DEVELOPMENT OF THE SILISPECT SMALL-ANIMAL IMAGER

By

Benjamin Seth McDonald

Dissertation

Submitted to the Faculty of the

Graduate School of Vanderbilt University

in partial fulfillment of the requirements

for the degree of

DOCTOR OF PHILOSOPHY

in

Physics

May, 2010

Nashville, Tennessee

Approved:

Professor Todd E. Peterson

Professor John C. Gore

Professor Thomas E. Yankeelov

Professor M. Shane Hutson

Professor Will E. Johns

DEDICATION

To Hannah Estelle McDonald

ACKNOWLEDGMENTS

I am grateful for Todd Peterson's mentoring and guidance through this project. In the academic spirit, he always entertained my questions, even if they were slightly off topic. I am also thankful for his patience and skills as a listener. His steady encouragement and cheerfulness helped propel me forward, especially after many experimental foibles. Dr. Peterson generously sent me to many conferences where I was able to present our work and meet others in the field. This was valuable not only for my scientific development, but it kept me abreast of research in the closely-related field which I am now entering. Mixed with the memories of working out problems with Dr. Peterson in the lab or in his office will be his exhortations at the research retreats, reminding me of my need to "fight for my right to party."

The other members of my committee, Drs. Gore, Yankeelov, Hutson, and Johns, helped me stay on target during this process. Dr. Gore has crafted a collegial environment in the VUIIS. I enjoyed the research retreats, which broadened my understanding of the work done at Vanderbilt beyond the world of SPECT instrumentation and helped build community within the VUIIS.

Dr. Shokouhi introduced me to the detector system and provided consistently good scientific and professional advice. Heather Durko of the University of Arizona was a cheerful collaborator in working with the DSSDs. It was good to have someone to commiserate with when the DSSDs were belligerent. Thanks also to Ken Wilkens who helped design and build many of the components of SiliSPECT. Ken always had an idea for how to make something better!

When I first arrived at Vanderbilt I noticed that in a brochure my home state of Washington was considered the "Far West." My time in Nashville has helped fulfill Cornelius Vanderbilt's goal of "...strengthening the ties which should exist between all sections of our common country." We forged life-long friendships here with people from across the Mid-South. Thanks to the Yankeelovs for Yankeeloving us with the power of a thousand suns.

Camaraderie among graduate students was one of the reason I chose Vanderbilt, and it proved to be a good instinct. Lunch-time conversations were particularly savored with Christopher Goodin, Stephen Johnson, Hugo Valle, and Jonathan Jarvis. The office group of Chris Wargo, Saikat Sengupta, Jack Skinner, Jennifer Whisenant, Chris Jarrett and Elizabeth Stringer all helped make a supportive and friendly work place.

I am indebted to Hannah for joining me in this adventure, providing encouragement, love, and companionship. If she ever gets the itch to pursue a PhD (beside the one she already has in patience), I will be there to the end. The last five years were filled with joy, especially the last two raising our son, Samuel. My parents, Amy and Paul McDonald, have also been constant encouragers. They helped shape my values to be a lifelong learner and to take creative risks.

I am grateful for the support of several sources of funding which made this work possible (and life more comfortable). Work at Vanderbilt University was supported by NIBIB grant R33-EB000776 and a Career Award at the Scientific Interface (TEP)

from the Burroughs Wellcome Fund. I also am thankful for the support given by the William A. and Nancy F. McMinn Fellowship in the department of physics and astronomy, and travel grants from the IEEE NPSS, Vanderbilt Graduate School, and the University of Arizona's Center for Gamma-ray Imaging.

TABLE OF CONTENTS

LIST OF TABLES

LIST OF FIGURES

CHAPTER I

INTRODUCTION

1.1 Key events in gamma-ray imaging history

Gamma-ray imaging systems have been the focus of much research in the fifty years since Hal Anger developed the gamma camera. Major efforts in developing imaging detectors, apertures, and algorithms have been performed in astronomy, high-energy physics, nuclear medicine, oil exploration, and security communities. Nuclear medical imaging has the longest history.

The foundation of nuclear medicine is based on a simple idea: isotopes of the same element are chemically inseparable, so radioactive nuclei can serve as markers of their stable, abundant counterparts. Radioactive materials were first intentionally put in living systems in 1923 when George de Hevesy examined the transport of radioactive lead in plants [1]. In 1935, de Hevesy and Chiewitz studied the biodistribution and metabolism of ^{32}P in rats [2], demonstrating that bone growth is in a constant state of turnover. Radiotracer presence was determined with Geiger-Müller (GM) tubes. He used this same technique to prove that his landlady was recycling food in her boarding house meals [3].

The first clinical gamma ray imaging system, the rectilinear scanner, debuted in 1951 [4]. Maps of the distribution of ^{131}I within the thyroid gland were produced by raster-scanning a cylindrical, single-channel collimator coupled to a thallium-doped sodium iodide scintillator and a photomultiplier tube (PMT). Scans were prohibitively

long, though. Hal Anger solved this problem in 1952 by creating the gamma camera, which consisted of a pinhole collimator and a scintillator crystal coupled to an array of photomultiplier tubes [5]. Centroid calculations of the photomultiplier tube signals yielded two-dimensional position estimation of each gamma-ray interaction in the crystal. The wide field-of-view (FOV) pinhole allowed the entire thyroid to be imaged from one detector position. The basic detection system underlying Anger's camera is still found in most clinical cameras today. Detailed accounts of the early years of nuclear imaging are found in Refs. [6–8].

In 1963 computed tomography was implemented, which expanded the utility of nuclear imaging to deeper objects within the body. Eventually the acronym SPECT, for Single-Photon Emission Computed Tomography, was coined to distinguish the technology from positron emission tomography (PET) [9]. SPECT systems consist of an image-forming element, a detector system, and an image reconstruction algorithm [10]. Imaging formation is done with absorption, whereby a small number of the photons emitted from the object pass through an aperture plate and interact in a position-sensitive detector. Photons that hit the aperture plate are attenuated, but those that make it through the holes contain directional information about their origin. Projections of the object are collected at different angles and used in a tomographic image reconstruction algorithm, which produces an estimation of the 3D distribution of activity within the object. Scatter and attenuation within the body complicate the estimation process, but SPECT image quality continues to improve.

Landmark achievements for SPECT in the last three decades included iterative reconstruction algorithms [11–13], which provided better system modeling and im-

proved image quality, attenuation correction methods, which improved quantitative accuracy, dual-modality systems that combined structural and functional information [14], and designs that boosted sensitivity, such as multi-headed scanners. All of these advances made large impacts in clinical decision-making, patient throughput, and in basic research.

The first nuclear imaging subjects, small animals, became a focus of attention again in the 1990s. Imaging small animals presented a host of new challenges and opportunities. The largest challenge was to improve spatial resolution by at least an order of magnitude while also using a smaller injected dose. Smaller image voxels meant less signal per voxel, so similar amounts of activity had to be injected into animals as in humans. Since the volume of a radiotracer injection used for a human could be as large as the total blood volume of a mouse, higher specific activity tracers were needed. Before in vivo imaging techniques like SPECT, greater numbers of animals were needed in experimental studies. Animals had to be sacrificed at different time intervals and imaged with ex vivo methods, like autoradiography. With SPECT a single animal can act as its own control and can be imaged multiple times, thereby reducing the number of animals required for a study.

Small-animal SPECT has found use in a growing range of in vivo imaging studies [15–18]. Several research needs have driven the development of new imager designs including better spatial resolution, sensitivity, cost, throughput, and accurate image quantification. In particular, detecting smaller lesions in various disease studies (such as plaques associated with Ahlzheimer's disease [19]) and tracking and counting radiolabeled stem cells [20] are applications that require new SPECT devices. As spatial

resolution is increased, considerably fewer counts are needed to make images of comparable visual quality [21]. Better spatial resolution also reduces the partial volume effect and its errors toward image quantification.

1.2 The scope of small-animal SPECT

Small-animal SPECT is useful in three main areas: translational studies of human disease, understanding biochemical processes, and animal disease itself. The majority of current research lies in the first two categories, which together are part of the burgeoning field of molecular imaging. Several recent reviews enumerate molecular imaging research utilizing small animal SPECT [15, 17, 22, 23]. For SPECT to answer meaningful biological questions, it must be coupled with well-understood probes and animal models (Fig. 1.1). Though this thesis is focused on instrumentation, it is helpful to motivate SPECT development in terms of its applications.

The goal of molecular imaging is to map the location and expression levels of genes and proteins that are considered to play key roles in the molecular pathways of disease [24]. Herschman [25] calls it, "noninvasive, quantitative, and repetitive imaging of targeted macromolecules and biological processes in living organisms." Molecular imaging consists of two components: a molecular probe whose properties are altered by a specific biological process, and means to detect and monitor those processes. Whereas many clinical imaging tasks measure the end results of disease (physiologically), molecular imaging aims to measure the processes that constitute the basis of disease, ideally before the disease promulgates [26].

Small animal SPECT is recognized as a key a tool for quantitative imaging of

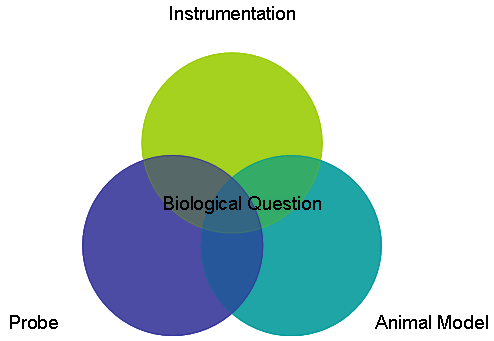

Figure 1.1: Venn diagram of components needed to answer biological questions with molecular imaging. Instrumentation and tool development are the focus of this work.

molecular processes and in drug development [15, 27]. Tissue viability, vascular integrity, organ specificity, and clearance properties of new radiolabeled drugs can be rapidly evaluated with SPECT measurements. SPECT also allows rapid screening of tracer biodistribution. If a drug must cross the blood brain barrier, for instance, SPECT (or simple planar imaging) can determine whether a radiolabeled candidate molecule succeeds. Most SPECT isotopes can be used in animals or humans.

Overall, animals present a friendlier imaging environment than humans, as explained in Table I.1.

1.3 SPECT among the other modalities

Small animal SPECT has a unique place among the armamentarium of molecular imaging technologies. First, only SPECT contrast agents span the set of all molecular probe sizes at high spatial resolution. Naturally occurring small molecules (1-100 Da) can be radiolabeled as can the largest molecular structures (10^5-10^6 Da), antibodies and peptides, which have slow biodistribution requiring days for localization

Table I.1: Clinical versus small-animal SPECT (modified from [28])

Clinical SPECT	Small-animal SPECT
∼1 cm resolution	sub-mm resolution
FOV ∼50 cm	FOV ∼5 cm (less if organ)
Parallel collimators used to cover FOV	Pinhole apertures used for magnification
Body dimensions $\gg 1/\mu$	Body dimensions $\ll 1/\mu$
Large amounts of scatter and attenuation	Smaller amounts of scatter and attenuation
Multiple scatter likely	Single scatter approximation useful
Need $E_{photon} > 100$ keV	Can use E_{photon} ∼30 keV
Radiation dose critical	Volume of tracer critical
Want shorter half-life (hours, e.g.s, ^{99m}Tc	Can use longer half-life isotopes
General-purpose cameras & instruments	Clinical cameras with special collimators or specialized instruments
Quantitative desirable, but detection tasks more common	Estimation taks more interesting for research

and clearance [15]. SPECT radiochemistry is also robust. Direct isotopic substitution allows molecules to be labeled without changing their biochemical features. In optical imaging, fluorescent tags increase the molecular probe's weight which can alter the tracer's biochemical interactions and biodistribution. SPECT also uses analog radiotracers, which make chemical changes to a molecule so that trapping occurs in certain cells or so as to isolate a specific molecular pathway [24]. With the latter approach isotopes of elements can be used in the probe not normally found in the molecule. Compared to optical methods, SPECT tracers can be imaged at higher resolution and in deeper tissue structures.

SPECT is set apart from its nuclear cousin, PET, by sensitivity, radiochemistry, cost, and spatial resolution limits. First, SPECT is sensitive to nanomolar concentrations of tracer, which makes it several orders of magnitude more sensitive than MRI methods. Yet PET is the most sensitive (picomolar) modality since it operates

without a physical collimator. On the other hand, iodine chemistry and technetium labeling is easier than ^{18}F labeling, which requires more complex organic chemistry (and the assistance of a radiopharmacy) [15]. Meikle notes that the efficiency of iodination reactions leads to higher specific activity agents that somewhat makeup for PETs sensitivity advantage over SPECT. Overall, SPECT tracers have higher specific activity [29], which is critical in neurotransmitter studies [16]. Many isotopes used in SPECT have longer half-lives (hours to days) than PET counterparts (minutes to hours) which require on-site production and labeling. The PET tracer infrastructure and larger number of required detectors make small-animal PET scanners more expensive (at least twice as much) than SPECT [30]. SPECT images resolution below 0.1 mm has already been achieved, but the best PET image resolution is still just under 1 mm. In PET, the positron range and noncolinearity of the annihilation photons place a limit near 0.6 mm on the spatial resolution, whereas there is no limit in SPECT [31]. PET's few long-lived isotopes, such as ^{124}I, have very energetic positrons which travel longer before annihilating, further degrading spatial resolution. In SPECT, multi-pinhole apertures with small pinhole diameters placed close to the object yield high resolution and high sensitivity images. These differences alone are reason enough for SPECTs continued existence.

A important distinction for SPECT is its ability to probe multiple molecular processes simultaneously via dual-isotope imaging. In the 2002 Society of Nuclear Medicine Highlights Lecture, Henry Wagner said, "Despite the enormous popularity of PET, SPECT will survive because of its ability to image multiple tracers simultaneously..." [32]. For instance, ^{125}I endothelial growth factor and ^{99m}Tc-MDP can

concurrently image bone metastases and regions of bone growth [32]. In 2006, Paul Acton asked, "Given that resolution far superior to PET are achievable, and with multiple-pinhole systems providing much better sensitivity, should SPECT replace PET as the standard radionuclide imaging tool?" [33] This is unlikely to happen, though, because SPECT and PET are often complementary [34]. Disadvantages of SPECT include the fact that it uses ionizing radiation and that there will almost always be some background signal from non-bound probes.

1.4 Objectives and contributions of this work

The goal of this project was to develop a multi-pinhole SPECT system offering high spatial resolution with good sensitivity for the imaging of ^{125}I-labeled radiotracers in small animals. The system consists of four silicon double-sided strip detectors each of 60.4 mm x 60.4 mm active area and 1 mm thickness with an intrinsic spatial resolution of approximately 59 μm. Each camera of this dual-headed system is comprised of a pair of detectors mounted one behind the other, allowing for pinhole projection data to be acquired at multiple magnifications simultaneously while also offering improved detection efficiency. The use of 127-pinhole, focused apertures on each camera head provides sufficient angular sampling for tomographic images to be reconstructed from data acquired without rotation of either the imaging system or subject. The apertures were designed for small FOV, high sensitivity imaging, such as for a mouse brain.

The main accomplishments included:

1) Characterizing the detectors which form the basis of the imaging system.

2) Developing threshold-adjusting methods to improve low-energy trigger uniformity.

3) Assembling the camera heads and testing their planar imaging performance.

4) Writing programs to control the data acquisition and process the list-mode data.

5) Implementing an acquisition protocol and method to estimate the geometric calibration parameters needed for tomographic image reconstruction.

1.5 Overview of the thesis

The thesis is composed of three main components: the detector, the camera head, and the imaging system. We started with detector measurements, then built camera heads and made pertinent tests, and finally calibrated the system for tomographic image reconstruction. The chapter order follows this basic scheme.

Chapter 2 places this work in context with other ultra-high spatial resolution detectors and nontraditional acquisition geometries. In chapter 3, the detector system architecture is detailed. Chapter 4 includes the bulk of the work, with detector characterization, and methods developed to improve detector performance. Chapter 5 contains the camera head design and assembly, and performance measurements, such as system sensitivity and spatial resolution. In Chapter 6 efforts to extract geometric calibration parameters for tomographic image reconstruction are described. Lastly, chapter 7 presents the conclusions of this work and makes recommendations for future investigations.

CHAPTER II

LITERATURE REVIEW

2.1 Pinhole imaging

Pinhole imaging has a very rich literature. It is getting renewed interest for pre-clinical and clinical applications for several reasons. Probably the largest reason is related to the advent of high spatial resolution detectors.

In absorptive collimation only gamma rays with incident angles confined by the shape of the aperture pass through to the detector. This gives approximate angular origin of the photons, but it is very inefficient for most apertures (on the order of 0.01 % pass through the aperture). Pinhole apertures suffer a tradeoff between sensitivity and spatial resolution. A pinhole provides magnification of the object by a factor M = a/b, where a is the detector-aperture distance, and b is the object-aperture distance. Planar image resolution, R_{sys}, is given in terms of full-width at half-maximum (FWHM) of the point response function (PRF). To first order, it is the sum in quadrature of effect of the intrinsic detector resolution, R_i, and geometric blurring due to the aperture:

$$R_{sys} = \sqrt{d_e^2(1 + 1/M)^2 + (R_i/M)^2}, \tag{2.1}$$

where d_e is the effective pinhole diameter, which is always somewhat larger than the actual diameter due to edge penetration by some photons and is dependent upon

the aperture material, the energy of the photons, and the shape of the pinholes. To image small objects within an animal, pinholes with sub-1 mm diameter must be used. High resolution detectors are needed for high planar image resolution across the depth of field. Fig. 2.1(b) shows the planar resolution for two different detector resolutions. As the magnification increases, the low-resolution detector is much slower to approach the resolution limit set by the pinhole geometry. While the planar resolution increases with smaller pinholes, the sensitivity (geometric pinhole efficiency), g, for a point source decreases:

$$g = \frac{d_e^2 \sin^3 \theta}{16b^2}, \tag{2.2}$$

where θ is the angle between the source at the aperture as shown in Fig. 2.1(a). Keeping the source close to the aperture is important for obtaining a reasonable sensitivity.

With a parallel-hole collimator, the detector area determines the field of view. In pinhole imaging, there is some flexibility depending on the spatial resolution of the detector. A large, low-resolution detector can be placed at high magnification to achieve the same planar resolution and field of view as a small, high-resolution detector at lower magnification. What's really important are the number of independent measurements made by the detector, or the number of pixels in a discrete detector [10].

In 1993 Rogulksi et al. showed a way of reducing the inherent tradeoff between sensitivity and resolution [36]. With a high resolution detector, the detector can be placed close to the aperture so many small pinholes can be packed close together

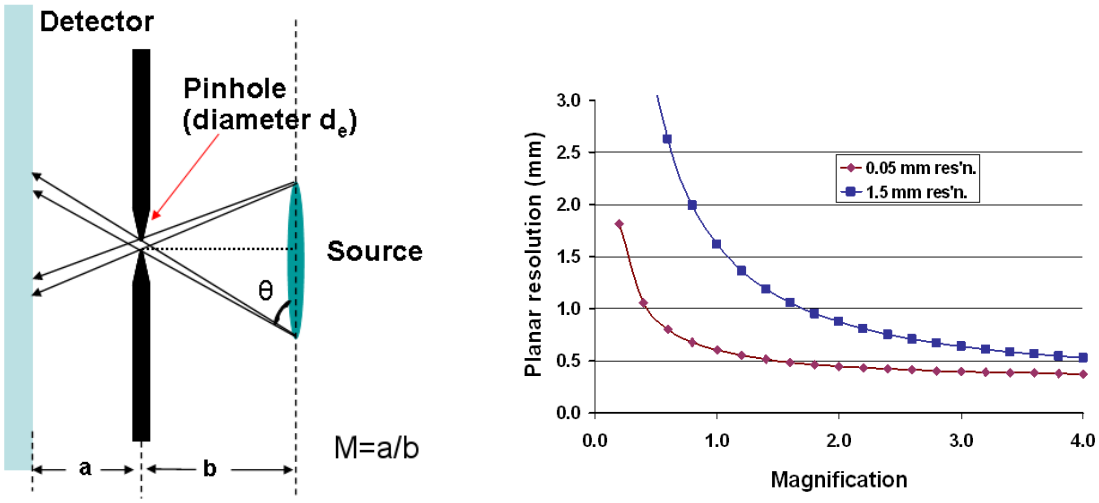

(a) (b)

Figure 2.1: Diagram showing pinhole magnification factors 2.1(a). If a/b is greater than one, then the object is magnified on the detector. As magnification increases the planar image resolution approaches the aperture diameter. 2.1(b) shows resolution versus magnification for an object 2.5 cm from a 300 μm-diameter pinhole. The two curves show that the planar image resolution quickly approaches the pinhole size when a high spatial resolution detector is used [35].

without projection overlap, or spatial multiplexing. A greater number of smaller-diameter pinholes actually gives better sensitivity and resolution than fewer, large-diameter pinholes. This is illustrated in the two designs in Fig. 2.2.

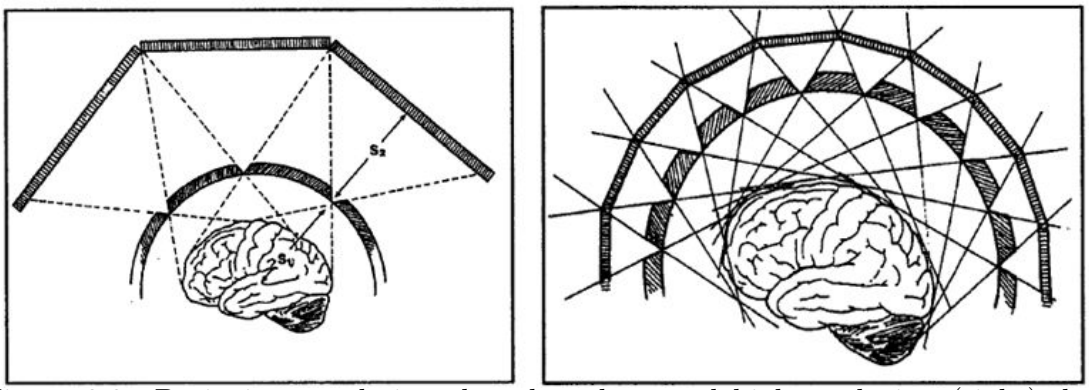

Figure 2.2: Brain imager designs based on low- and high-resolution (right) detectors [36]. With the high-resolution detectors, less magnification is need to get high planar image resolution, thus the detectors can be placed closer to the apertures. Then more pinholes can be used without multiplexing in the projection images.

2.2 Multiplexing in the projection images

Multiplexing in the projection images is another variable in imager design space. Some designs prevent multiplexing [37, 38], while others [39, 40] allow some multiplexing in the projection images. Vunckx et al., through a series of simulations, argued that artifacts from multiplexing negate any gains in sensitivity [41]. Large amounts of multiplexing in the projection images cause obvious artifacts[42]. These arise simply because in the multiplexed projections, it is not known whether a given photon came from one pinhole or another. A way to keep multiplexing (and its sensitivity boost) was discovered by Wilson et al., who showed that tomographic images could be reconstructed from highly multiplexed projection data with a high resolution detector, a multi-pinhole aperture, an iterative reconstruction algorithm, and projections collected at multiple magnifications [43]. The low-magnification image has little to no multiplexing, which when combined with higher-magnification, higher-multiplexed projections, helps detangle the multiplexed data. Fig. 2.3 shows simulated projections with and without multiplexing. This approach was called the synthetic collimator method. One reason this is possible is because multi-pinhole apertures sample different angular views simultaneously, permitting limited-angle tomography.

Work in the last five years has sought to experimentally demonstrate the synthetic collimator method. At the University of Arizona the M^3R system was built as a test bed for task-specific imaging and aperture design [40]. M^3R collected projection data through four aperture plates onto four detectors simultaneously, and the

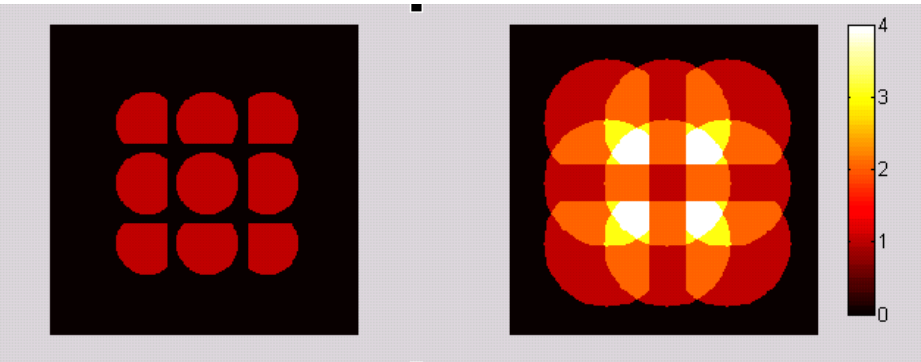

Figure 2.3: Simulated non-multiplexed projections (left) and highly multiplexed projections (right) from a small flat object through nine pinholes. The detector-aperture distance is greater in the right image. The color scale indicates the level of multiplexing. For instance, a level of 3 means that a photon could have traveled through any one of three pinholes to interact at that position on the detector.

data was combined into an iterative reconstruction algorithm. Results indicated that some multiplexing in the projection data improves certain task performance over non-multiplexed data [44]. While M^3R successfully investigated aperture configurations, it was not ideally suited to validate the synthetic collimator method, since the resolution of the detectors was somewhat low (2-3 mm) and magnification was limited. Similar to the synthetic collimator is the T-SPECT System [45]. Here the detector-aperture distance is fixed and the object is moved around in a T-shape. The object is viewed at different angles so the projection data contains more information about the 3D activity distribution. A prototype silicon double-sided strip detector (DSSD) system built at Vanderbilt University validated the synthetic collimator method [46]. With detector resolution below 100 μm, planar image resolution was high at low magnification and a large number of small pinholes were used to increase sensitivity and angular sampling. The prototype DSSD is 300 μm thick, giving it fairly low detection efficiency for ^{125}I photons. The layout of the readout electronics prevented stacking

detectors so multiple-magnification images could not be acquired simultaneously. To improve upon the prototype, a new system, SiliSPECT, was designed and developed with thicker detectors, more resolution elements, and a different readout geometry. In the prototype system a 23-pinhole aperture was used; SiliSPECT utilizes 127-pinhole apertures on two camera heads.

SiliSPECT implements the synthetic collimator method where all magnifications are collected simultaneously with stacked detectors [47–49]. SiliSPECT incorporates unique detectors, apertures, and synthetic collimator reconstruction. We designed SiliSPECT to image targeted regions of rodents (e.g., mouse brain) with a motionless acquisition. Silicon double-sided strip detectors (DSSDs) form the basis of SiliSPECT. Stacked detectors increase the total detection efficiency, and collect multiple magnifications simultaneously. The low-magnification detector has much less multiplexing in the projection image, which helps the iterative reconstruction algorithm sort through the more multiplexed, high-magnification projection data.

2.3 Survey of small-animal SPECT systems

In the last decade, new SPECT imager designs have taken several paths to improve image spatial resolution. One way was to replace the clinical gamma-camera with a higher intrinsic resolution semiconductor [35, 50, 51] or scintillator [52, 53] detectors. Recently, various types of CCDs have been coupled to scintillator crystals for high-resolution readout of the scintillation light [54–57]. Another way is to use pinhole apertures in high magnification configurations [58]. To enhance sensitivity, multiple-pinhole apertures and camera heads have been utilized [37]. Furthermore, field-of-

view (FOV) can be traded for sensitivity by tilting pinholes toward a common focus [59, 60].

Small-animal SPECT scanners can be categorized in many ways: those with special collimators adapted for clinical cameras (e.g. [37, 39]) and dedicated research systems (e.g., [51, 52, 61, 62]). The research systems can be classified further based on whether the detectors have asynchronous (event-driven) or synchronous (integrating) readout. There are also pixelated [63] and monolithic scintillators or semiconductor-based systems, those that rotate and those that are stationary. A list of recent systems and some of their properties is given in Table II.1 below. As mentioned above, the detector resolution is the most important component of the imaging system at low magnifications. So instead of focusing on the various apertures or acquisition strategies, we will the compare ultra-high resolution detectors used in SPECT.

Table II.1: A survey of multi-pinhole SPECT systems. This list includes most published systems and a few commercial systems. References, a brief system description (pinhole diameter), the radius of rotation (ROR), and sensitivity are given. This is an expanded table from J. Hesterman's thesis [64].

Reference	System Description	ROR (cm)	Res. (mm)	Sensit. (cps/MBq)
Kastis et al, 1998 [65]	FastSPECT I: 24 1.5 mm pinholes, twenty-four NaI(Tl) modcams (4 PMT)	2.0	2.0	359
Meikle et al, 2003 [66]	Four 0.5 mm pinholes, single NaI(Tl) PSPMT camera	4.0	1.5	146
Schramm et al, 2003 [39]	Seven 1.5 mm pinholes, single clinical camera, some multiplexing	2.0	2.0	325
Furenlid et al, 2004 [52]	FastSPECT II: Sixteen 1.0 or 0.1 mm pinholes and NaI(Tl) modcams (9 PMT), no multiplexing	4.0	2.2	243

Continued on Next Page...

Table II.1 – Continued

Reference	System Description	ROR (cm)	Res. (mm)	Sensit. (cps/MBq)
Moore et al, 2004 [67, 68]	Six 0.8 mm pinholes, triple-head clinical camera	3.2	∼1.0	300
Choong et al, 2005 [50]	Dual-headed camera, Si(Li) detectors, 64 x 40 mm FOV with parallel-hole collimator for ^{125}I	2.0	1.6	181
Weisenberger et al, 2005 [69]	Awake animal imaging with IR tracking, pixelated NaI(Tl) crystals, PSPMTs	1.0	3*	170*
Beekman et al, 2005 [37]	U-SPECT I: 75 0.6 mm pinholes in annulus, 3 clinical cameras, no multiplexing	4.4	0.5	2200
Goertzen et al, 2005 [70]	mouseSPECT: Annular NaI(Tl)+PMTs, eight 1 mm pinholes, rotating collimator	2.8	1.7	346
Kim et al, 2006 [51]	SemiSPECT: Eight 0.5 mm pinholes, eight 27 mm^2 CZT detectors	3.2	1.45	153
Funk et al, 2006 [60]	24 0.5 mm pinholes in a cylindrical collimator with 3.0 x 1.5 cm FOV, 24 CsI(Tl) + PSAPDs	3.0*	0.8*	630*
Schramm et al, 2006 [71]	NanoSPECT/CT: multiplexed rat & mouse apertures, four large NaI(Tl)/PMTs	30	0.4-1.0	1000-2000
Accorsi et al, 2007 [72]	MediSPECT: 256x256 55 μm pixel CdTe detector, coded aperture or 0.3 mm pinholes	3.1	0.11	233
GM-Ideas, 2007 e.g.,[73]	X-SPECT: two rotating NaI(Tl) detectors, various apertures (new version has CZT)	2.0-4.0	0.62-∼2.0	23-855
Hesterman et al, 2007 [40, 44, 64]	M^{3}R: four modcams with swappable apertures (adaptive system)	1.6	1.18-1.48	50-315
Soesbe et al, 2007 [56]	Various apertures used with a columnar CSI(Tl) crystal lens-coupled to an EMCCD sensor	NA	0.96, ∼0.11 intrinsic	38
van der Have et al, 2007 [59]	U-SPECT II: 75 pinholes in annulus (four sizes), commercial system, no multiplexing	NA	0.35 best	700 (0.35 mm)

Continued on Next Page...

Table II.1 – Continued

Reference	System Description	ROR (cm)	Res. (mm)	Sensit. (cps/MBq)
R Accorsi, 2008 [74]	Soft x-ray microscope made with NTHT MURA coded aperture and CCD	1.095	0.025, 0.02 intrinsic	302
Zingerman et al, 2008 [75],	0.6 mm pinholes, Gd2O2S(Tb) phosphor, standard CCD, 20 mm FOV	∼2.0	0.86*	135*
Qian et al, 2008 [76]	Pixelated NaI(Tl) crystal array, PSPMTs, 1 mm pinholes (1 to 5) or CuBe parallel hole aperture	2.5	1.2-1.4	252-417
Miller at al, 2008 [55, 77]	BazookaSPECT: micro coded aperture, GaOS screen, lenses, and CCD	NA	0.03 planar	NA
Shokouhi et al, 2008 [78–80]	SiliSPECT: Two-heads, four silicon DSSDs, 127 250 μm pinholes focused on 10 mm FOV	2.0	∼0.1	700-810*
Meng et al, 2009 [54, 81–83]	Columnar CsI(Tl) crystal, DM tube & EMCCD, multi-pinhole apertures (150, 200, 300 μm)	2.0	0.03-0.16	110-180

*Performance measurements simulated

2.4 Detectors for high-resolution SPECT

Silicon has many desirable properties for SPECT. It has the best material quality and charge transport properties among semiconductor materials. It also has reasonably high resistivity so detectors can operate at room temperature without cooling, unlike Germanium detectors. The disadvantage is it's relatively low detection efficiency due to its low atomic number and density.

Silicon double-sided strip detectors (DSSDs) form the basis and the name of the SiliSPECT system. These detectors have their roots in high-energy physics, where they are generally used to track charged-particles. They also have robust use in astrophysics applications (e.g., [84]). DSSDs have been infrequently used in med-

ical imaging. Papanestis et al. built a mammography system from 300 μm-thick DSSDs [85]. Recently silicon DSSDs have been used to monitor the real-time dose rate from radiation therapy beams [86]. Contemporaneous with our work is the similarly named SiliPET project [87]. Their goal is to use many layers of edge-on DSSDs to build a high-resolution PET scanner. In the same vein, but with lower spatial resolution CdTe detectors, Mitchell et al. tested several detector modules for a PET machine [88].

The main reason silicon DSSDs were not considered for SPECT earlier was their low-efficiency for most SPECT radiotracer emissions. DSSDs are well-suited to detection the emissions ^{125}I, however, a relevant isotope for small-animal imaging. The SiliSPECT DSSDs are thicker than the standard wafer at 1 mm. For ^{125}I emissions (27.2-35 keV) a millimeter of silicon has a total detection efficiency of around 36 %. The 60 day half-life makes ^{125}I readily available: suppliers keep various ^{125}I radiotracers in stock. Plus, at low energies the dominant interaction mechanism is photoelectric absorption. The low-energy photons from ^{125}I would be mostly attenuated in a human, but^{123}I or ^{131}I, which emit higher-energy photons, can be used instead.

Competing ultra-high resolution (<100 μm) detector technologies include hybrid detectors (scintillator plus semiconductor readout) and other directly read-out semiconductor detectors . The hybrid detectors consist of columnar CsI scintillators coupled to a gain stage (image intensifier [55] or de-magnifier tube [81]) which is then read out by a CCD/EMCCD. These systems have the advantage of being efficient for high energies, but the readout is integrated frame-by-frame. Thus, more effort

is required to extract the photon interaction positions compared to the direct read-out of each event with DSSDs. Silicon drift detectors are position-sensitive detectors with a single readout. Based on the timing of the readout signals, the interaction position can be inferred. These detectors are not thick enough for direct gamma-ray imaging, so they are usually coupled to scintillating layers, which lowers the spatial resolution [89].

A few other directly read-out semiconductor detectors have been considered or used for SPECT. Choong et al proposed a design for a ^{125}I imager based on pixelated Si(Li) detectors [50]. The detectors were a 6 mm thick, 40 x 40 array of 1 mm^2 pixels). The 6 mm thickness gave good detection efficiency ($\sim$90 %), but the intrinsic resolution was lower than in SDDs or DSSDs. Choongs array has 5120 pixels while the SiliSPECT DSSDs have over 1 million quasipixels. At the University of Arizona a group built SemiSPECT, based on a ring of CZT detectors. CZT offers good stopping power and energy resolution, but still has some materials processing issues that increases nonuniform detector response. A group in Liverpool is using stacked Ge strip detectors in PET mode and for Compton imaging [90]. The preamplifier outputs are digitized at a high sampling rate, which permits pulse-shape analysis and sub-strip interpolation down to 1 mm from the 5 mm strip pitch. To our knowledge, these detectors have not been used for small-animal SPECT. The intrinsic resolution is considerably less than the SiliSPECT DSSDS (59 μm), but the detection efficiency is higher. New Ge DSSDs with smaller strip pitch would allow imaging of higher energies, but require clever cooling systems. Thicker silicon DSSDs are being developed with waferbonding techniques [91]. Spatial resolution can decrease with thickness,

though, as charge carriers spread out as they travel to the electrodes. A promising technology that alleviates this problem are 3D silicon detectors, which have electrodes vertically placed through the detector thickness [92].

CHAPTER III

DETECTOR SYSTEM ARCHITECTURE

3.1 Overview of the detector system

The instrumentation for SiliSPECT is unique. Everything known about the way the detector system works is compiled in this chapter. Starting with the power supplies and ending with the list-mode data, each component of the system is described.

The detector system consists of a single power supply, four detectors, application-specific integrated circuits (ASICs) to read out the detector signals, digital isolators to extract the signal from the high voltage, FPGA-based packaging and control of the signals, and a National Instruments data-acquisition (NI-DAQ) card for transmitting data to a computer. The system architecture overview is shown in Fig. 3.1 and a corresponding photograph is in Fig. 3.2. These components will be detailed in following sections.

3.2 Silicon double-sided strip detectors

The DSSDs were custom made by SINTEF of Norway in 2005 [93]. The DSSD dimensions are 6.04 x 6.04 x 0.1 cm^3. The DSSD structure consists of 1024 N^+ strips (N-side) and 1024 P^+ strips (P-side), which are mutually perpendicular. The ion-implant strips are 20 μm wide, and the aluminum electrodes, which are on top of the above the implant strips, are 14 μm wide. More details are given in Table III.1. The silicon bulk is N-type semiconductor, so P-stops are implanted to electrically isolate

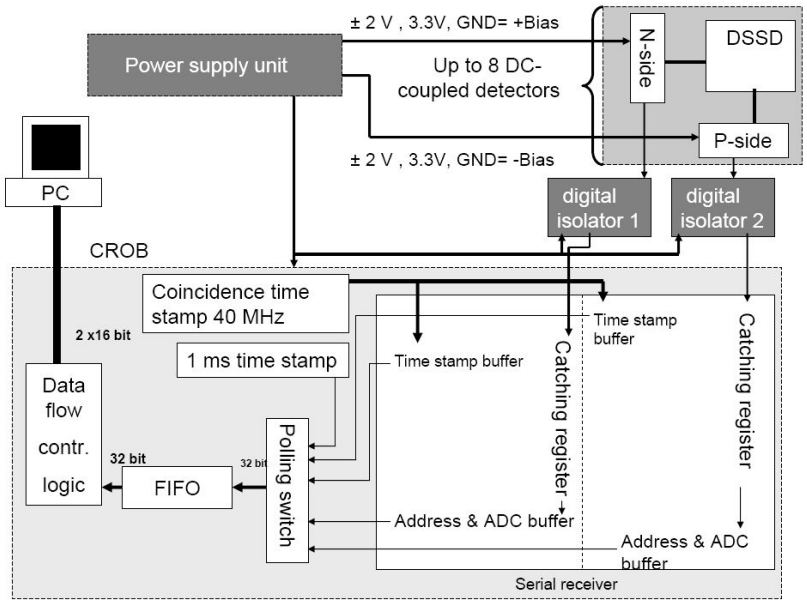

Figure 3.1: Diagram of the detector system. Data from the ASICS (trigger channel and ADC value) are decoupled from the bias voltage through digital isolators, are time-stamped in the CROB, and then transferred through a National Instruments DAQ board to a PC for storage and offline processing.

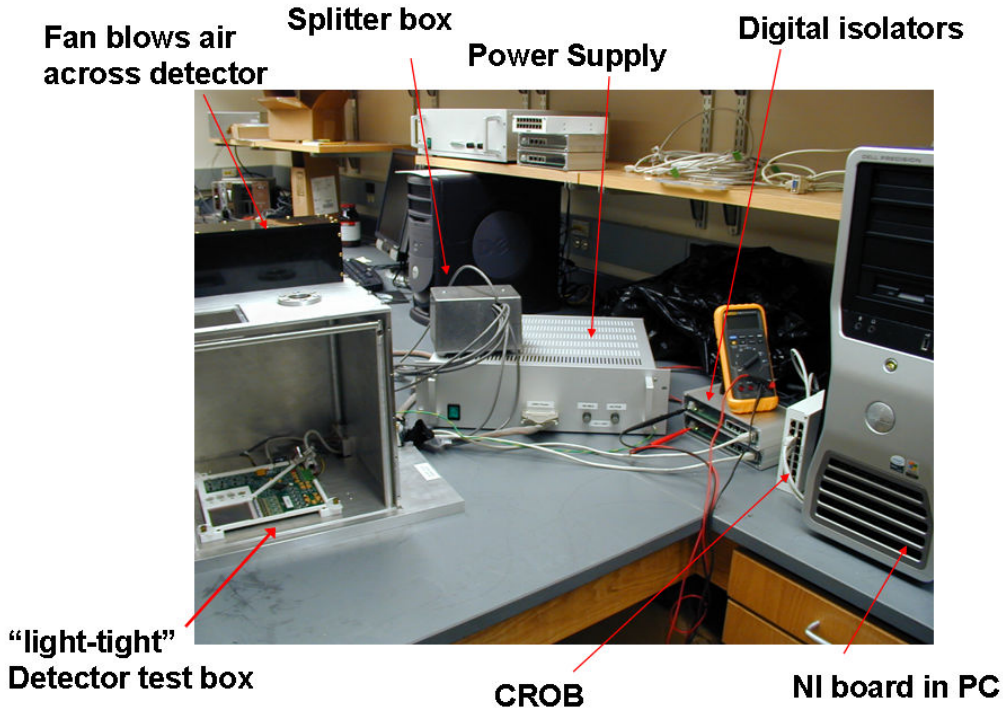

Figure 3.2: Photograph of the detector system with a single detector in the text box.

the N^+ strips. A schematic of a DSSD structure is shown in Fig. 3.3. The detectors are DC-coupled, so signals from the readout chips float on the HV bias.

Signals are generated on the readout strips through a cascade of physical processes. A photon interacts in the detector producing a high-energy electron, which then creates a cloud of electron-hole pairs. Because of the reverse bias and the PN junctions, the electrons drift to the N (Ohmic, positive bias) side and the holes move to the P (junction, negative bias). The moving charges induce signals on the strips which feed into the readout electronics. The integrated current on an electrode is the total charge, which is proportional to the photon energy deposition. A readout system amplifies the signal and digitizes, time stamps, and records the signal if it is above a set threshold. If triggers from the two detector sides are within a selected time window, their strip intersection forms the estimated 2D interaction position. Data from the 1024 strips on each detector side are processed to find the 2D interaction position for 1,048,576 quasi-pixels. This is the great advantage of DSSDs compared to pixel detectors: only 2N versus N^2 readout circuits for the same number of effective pixels.

Sintef provided two detector measurements. Leakage current was measured for a range of voltages at room temperature, as was the capacitance, on test structures made on the same wafers as the detectors (Figs. 3.5 and 3.4. Both the capacitance and the leakage current plateau when the high voltage is around 150 V. The depletion region between the implant strips of the detector is empty of conducting electrons or holes, but may have ionized donors or traps. The depletion region thus acts like a capacitor, and adjusting the voltage applied to the electrodes varies the depletion

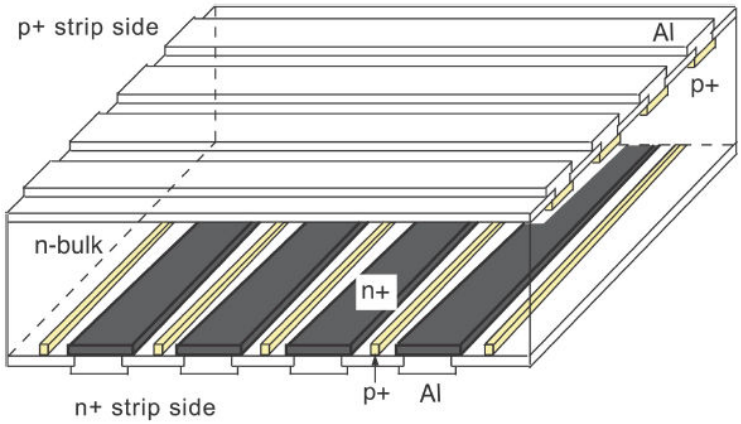

Figure 3.3: Double-sided strip detector schematic [84].Cross-sectional view of a DSSD. The doped p-type silicon strips (Junction side, p+, yellow) and the n-type silicon strips (Ohmic side, n+: black) are implanted orthogonally to provide two-dimensional coordinate measurements. Each n+ strip is electrically isolated by a floating p+-doped implantation (p-stops). Aluminum electrodes are coupled on each strip for reading out the signals.

Table III.1: DSSD Specifications.

Feature	DC-type	Unit
Chip size	63,576 x 63,576	μm^2
Active area	60,444.5 x 60,444.5	μm^2
Chip thickness	1000 $\pm$25	μm
Strip length	60,412	μm
Strip pitch	59	μm
Number of strips	1024/side	-
Implanted strip width	20	μm
Aluminum strip width	14	μm
P-stop width	8	μm
Bond pads (2/strip)	50 x 200	μm^2
Dist btw. strips & inner guard ring	50 (top/bottom) 67.5 (right/left)	μm
Multiguard structure	14 guard rings	-
Depletion Voltage	$\sim$150	V
Operation Voltage	$\sim$300	V

width. So when the depletion width (distance) is maximized, the capacitance is minimized according the geometry of a parallel plate capacitor (C ≈ Area/distance).

The depletion voltage is ∼150 V, but the detector is operated at 300 V (+150 V on N-side, -150 V on P-side) to decrease the charge collection time and ensure full depletion. Reducing the voltage to 150 V would not significantly reduce the leakage current, according to the data in Fig. 3.5. Reducing the temperature would have much larger effect on leakage current, as described in Ch. 4.4.

In total, 24 detector wafers were produced by Sintef. Six of the DSSDs were placed into ceramic frames and wirebonded to ASICS. Four detectors boards were also made for the Center for Gamma-Ray Imaging at the University of Arizona. The Arizonans have collaborated with us on the development tools for processing the detector output for and optimizing their performance. The other 14 crystals are unbonded and could be used in future detector systems.

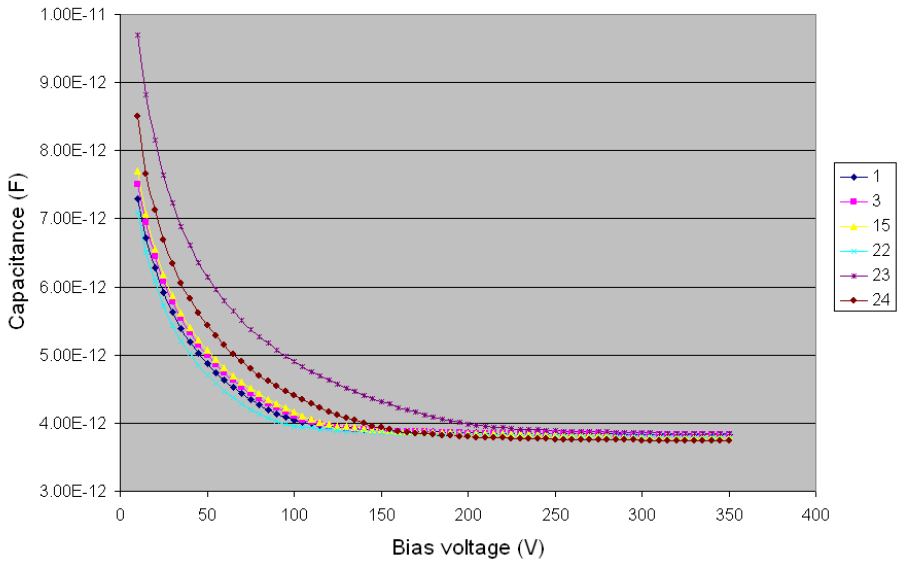

Figure 3.4: Capacitance vs. detector bias voltage measured on the active areas of six detectors as measured by Sintef. The depletion voltage is reached once the capacitance plateaus around 160 V.

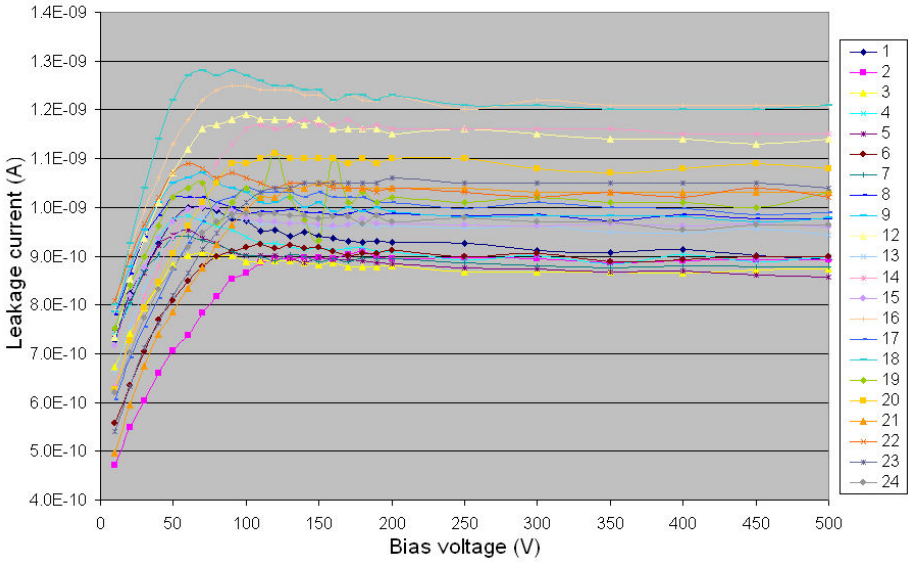

Figure 3.5: Leakage current vs. bias voltage for all detectors (active area). Leakage current plateaus around 150 V.

3.3 Detector readout

Signals from the DSSD electrodes are read out by VaTaGP6 chips, custom application-specific integrated circuits (ASIC) made by GM-Ideas of Norway. A single VaTaGP6 chip has 128 input channels. GM-Ideas wire-bonded the chips to the detector, built ceramic frames and back-end electronics for the system. Similar chips designed for SPECT were characterized by GM-Ideas ASIC designers in an 2005 paper [94].

Each detector side is read out with eight daisy-chained chips, as depicted in Fig. 3.6. Each chip has 128 of the integrated circuits shown in Fig. 3.7. Signal from each strip is integrated in a charge-sensitive preamplifier and simultaneously feeds into the two arms of the circuit. The top arm of the circuit (the Ta portion), determines whether the signal is above an externally set threshold (Vth) and gives a trigger signal if it is. The current pulse goes through a gain stage and then is shaped (with shaping time of 500 ns), sent through a high-pass filter, and then into

a level-set discriminator, which issues binary output (trigger or no trigger). Both shapers form semi-Gaussian signals to reduce noise. The trigger signal is sent to a field-programmable gate array (FPGA) which issues a hold on the output of the slow shaper in the bottom arm (the Va portion). This happens after the slow shaping amplifier in the bottom arm fully shapes its signal (3 μs shaping time). The analog peak value voltage is converted with a 12-bit analog-to-digital converter (ADC). The address of the triggered channel and the ADC value are read out by a serial or sparse read-out system and transferred to the CROB board, where they are buffered, time stamped, formed into data packets and sent to a PC.

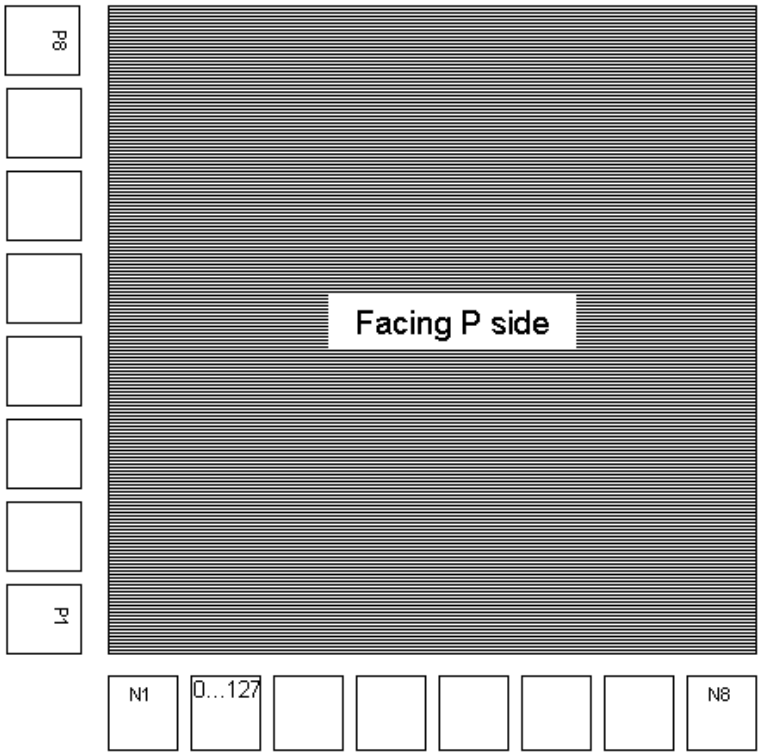

Figure 3.6: Diagram of the chip layout on a DSSD when facing the P-side. The origin of the channel numbers is in the lower left. Channels range from 0 to 127 on each chip and are rearranged in the FGPA to number linearly from 0 to 1023.

The operating points of field-effect transistors (FETs) in the ASICs are set by a network of bias currents and voltages. Each bias has a value that is referenced from

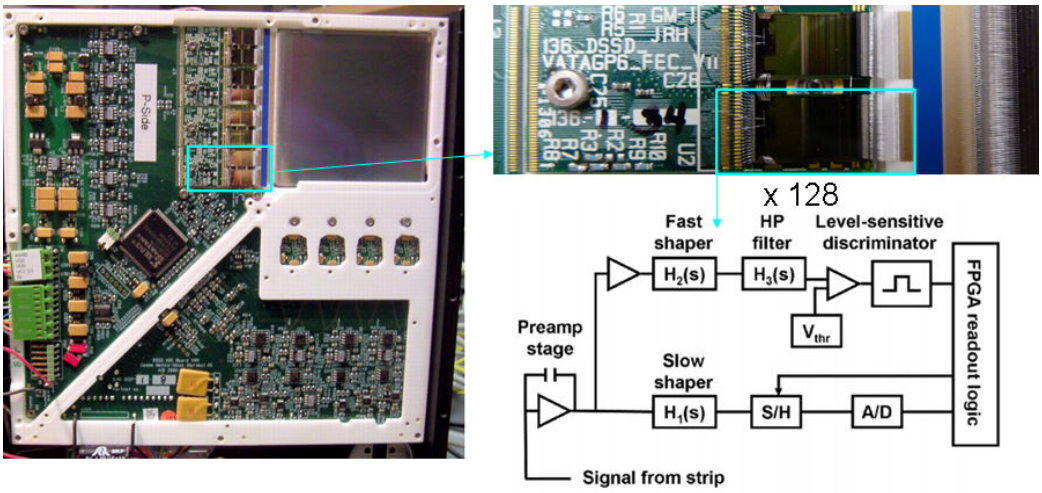

Figure 3.7: Photograph of a DSSD board (left) with a zoomed view of two chips (top right) and a diagram of a single channel in the ASIC (bottom right). The upper arm determines whether an event has occurred; the bottom arm measures the pulse height [95]

a main bias, Mbias. Many of the biases are set through user-modifiable digital-to-analog converters (DACs). The modifiable DACs are set externally through DACs which are wired to bond pads on the chips. Diagrams of the ASIC and a zoomed area of one bond pad row are shown in Fig. 3.8. If the connections are absent, the DACs assume a nominal value. On detector 19P a wirebond to the fifth chip's Sbif bond pad broke. This changed the Sbif value to some default value, which was much higher than the other chips. Through some threshold trim adjustments, the chip was coerced into triggering at the same rate as the other chips (Fig. 3.9).

The trigger threshold, Vth, is common to all channels. Channel thresholds can be adjusted relative to the common threshold by setting a 4-bit trim DAC. Thus, with some tweaking of the trim DACs on each channel the thresholds offsets, which arise from manufacturing process variations, can be aligned so each channel triggers at the same energy.

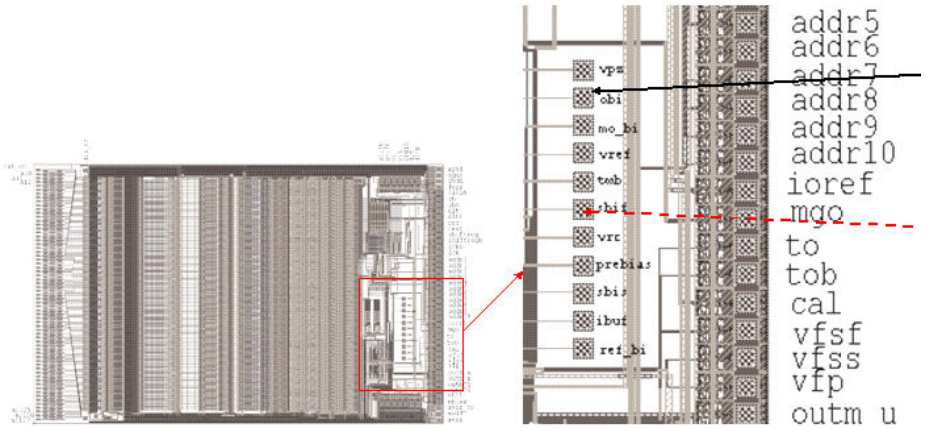

Figure 3.8: Schematic of VaTaGP6 ASIC (left) and expanded view of bond pad row for some of the DACs. Obi (solid line) and Sbif (dashed line) are wired on each chip. On chip 3 of P19 the Sbif wirebond broke, which prevented and user modification of the Sbif value and kept it at some nominal value.

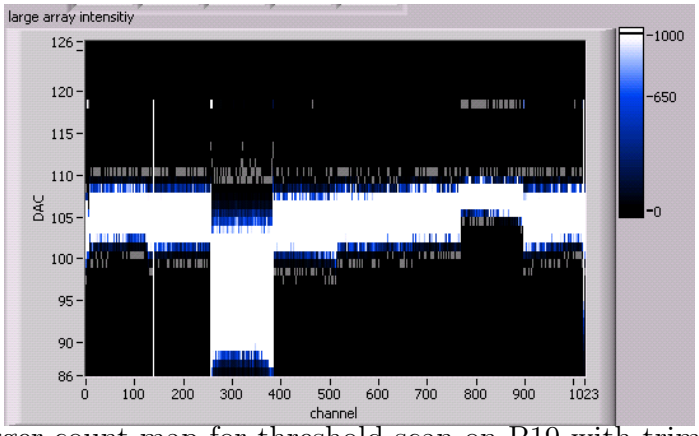

Figure 3.9: Trigger-count map for threshold scan on P19 with trims. The third chip has very high gain due to a broken Sbif wirebond which makes the chip assume a nominal value that is higher relative to the other chips. Chip seven has a lower gain for unknown reasons.

Other adjustable DACs include Vfp, Sbif, Vfss, and Vfsf. The Vfp DAC controls the feedback resistance of the preamplifier. The lower the Vfp, the higher the feedback resistance. If the Vfp is set too low the preamp becomes saturated, which could potentially damage the gate oxide of the input transistors. So it is important to make sure the Vfp is never set too low. In fact, in the Labview user-interfaces the lower range for Vfp was fixed so this could not happen. The noise at the preamplifier decreases with Vfp, but if the Vfp gets low enough the preamp turns off. We have seen this occur for some channels while looking at the real-time pedestal values in auto-triggered readout (described below). Turning up the Vfp brought these channels back to life with no lasting problems. The Vfp is sensitive to temperature changes as the feedback resistance is also affected by leakage current, which changes with temperature. Sbif is the DAC controlling the fast-shaper bias. Increasing Sbif improves the gain of the fast-amp, but also makes it less stable, according to the ASIC manual. Increasing Sbif helped achieve better triggering uniformity across all the channels, especially when multiple detectors were in close proximity. Changes to Vfss and Vfsf do not have major effects on the system performance and were not adjusted throughout the many experiments and acquisition. The discriminator DAC, Obi, is wired, but changing its value has no observed effect on the counting rate or shape of the threshold scan count histograms. Altering the DAC for the main reference DAC, Mbias, also has no known impact.

A number of features exist on the ASIC to ensure uniform triggering across the chips and increase readout stability. Table III.2 contains some of the most important features. The ASIC includes a leakage current compensation (CC) circuit that drains

leakage current from each preamplifier. The preamp inputs are connected to the strip electrodes directly, so leakage current flows directly into the preamp. Fig. 3.10 shows a diagram of the current compensation circuit. Leakage current is compensated via an adaptive MOSFET current source at the preamp input. The source is controlled by a slow differential amplifier that measures the differences between the input and output of the preamp. The current compensation was turned on for all detectors by default as an extra safety precaution. However, experience has shown that some detector sides operate more stably and uniformly when the CC network is disabled. The CC is toggled by programming a bit in the configuration register (which is a check box in the ASIC mask GUI).

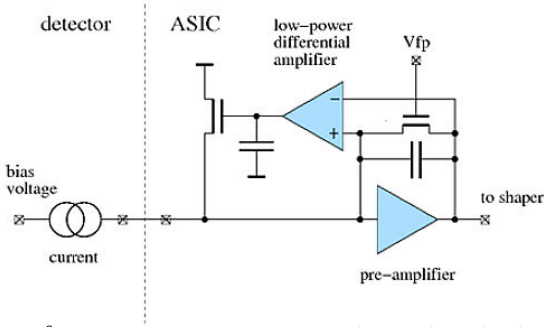

Figure 3.10: Diagram for current compensation circuit in XA ASIC, which has many things in common with the VaTaGP6 and was also designed by Gamma-Media Ideas [96].

The dynamic range (DNR) of the ASIC is given as ±14 fC. The energy required to create an electron-hole pair in silicon is 3.62 eV. The DNR translated to an energy value is (3.62 eV/e)*(14×10^{-15} C)*(1 e/1.602×10^{-19} C)*(1 keV/1000 eV) ≈ 316 keV. This is a much wider range than needed, since the silicon detectors are only reasonably efficient at stopping photons below 60 keV.

Using the equations in [97], the total strip capacitance for the DSSDs was estimated to be 1.56 pF/cm, or 9.41 pF total external input capacitance at the preamp.

Table III.2: VaTaGP6 ASIC Features.

Feature	Implementation	Comment
Adjustable internal bias values	Programmable DACs	Mbias is fixed
Each channel can be individually adjusted	Programmable DACs	Trims for adjusting, ASIC-level DACs for compensating
Channels can be enabled or disabled	Part of programmable 918-bit control register	Some noisy channels can also be 'drained'
Compensate large detector leakage current	Differential signals	Some detector sides have better response with this off
Combining several ASICs	Common address bus and analog line	Some common DACs among 8 chips on each DSSD side
Channel calibration test	Internal or external capacitor for charge injection	May have not been fully implemented

This capacitance is relatively high for silicon detectors. Capacitance and noise are directly related, so with this high capacitance we expect the energy resolution to be lower than most silicon detectors. The equivalent noise current (ENC), which is a measure of the noise in the chips, can be calculated with knowledge of the capacitance seen at the chip input. According to the ASIC manual, the ENC for the slow and fast shapers is:

$$ENC_{\text{slow}} = 40\ e^{-1} + 6\ e^{-1}/pF, ENC_{\text{fast}} = 70\ e^{-1} + 13\ e^{-1}/pF. \tag{3.1}$$

The ENC for the slow and fast shapers is 94.5 and 192.3 electrons (e^{-1}), respectively. These numbers are converted to eV by multiplying by the energy required to create an electron-hole pair in silicon, 3.62 eV/e^{-1}. This is the sigma for the energy resolution;

the FWHM is found by multiplying by 2.35. The minimum energy resolution due to the strip capacitance is thus 821 eV. This value does not include any contribution from the statistics of charge-carrier generation, but that contribution is relatively small because of silicon's Fano factor (which gives its sub-Poisson statistics). The energy blur due to counting statistics is [98]:

$$\Delta E_{FWHM} = 2.35\sqrt{FEE_i}, \tag{3.2}$$

where F is the Fano factor ($\sim$0.1 for silicon), E is the photon energy, and E_i is the ionization energy (3.62 eV). For an 18 keV photon, Eq. 3.2 evaluates to 0.19 keV. If the energy blur from the ENC and the counting statistics are added in quadrature, the result is 0.84 keV. Thus, the noise from the front end of the ASIC should yield an energy resolution that is less than 1 keV FWHM. In practice we observe higher values (worse energy resolution) because several other factors, such as leakage current and the readout process contribute to the energy resolution. Factors associated with the readout, such as the pickup from the digital clocking signals and time-walk on the fast amp also add to the noise (worsen the energy resolution).

3.4 Back-end electronics

Address and voltage values (from S/H) from the ASICs are controlled and processed by FPGAs. Fig. 3.11 shows the detector board and the location of one FPGA (others are within the CROB box). The signals float on the HV and digital isolators are used to decouple the signals from the HV. The S/H values are clocked out to

analog-to-digital converters (ADCs), whereupon the address value and ADC value are sent to a buffer in the CROB, time stamped, and sent to a PC in list-mode format.

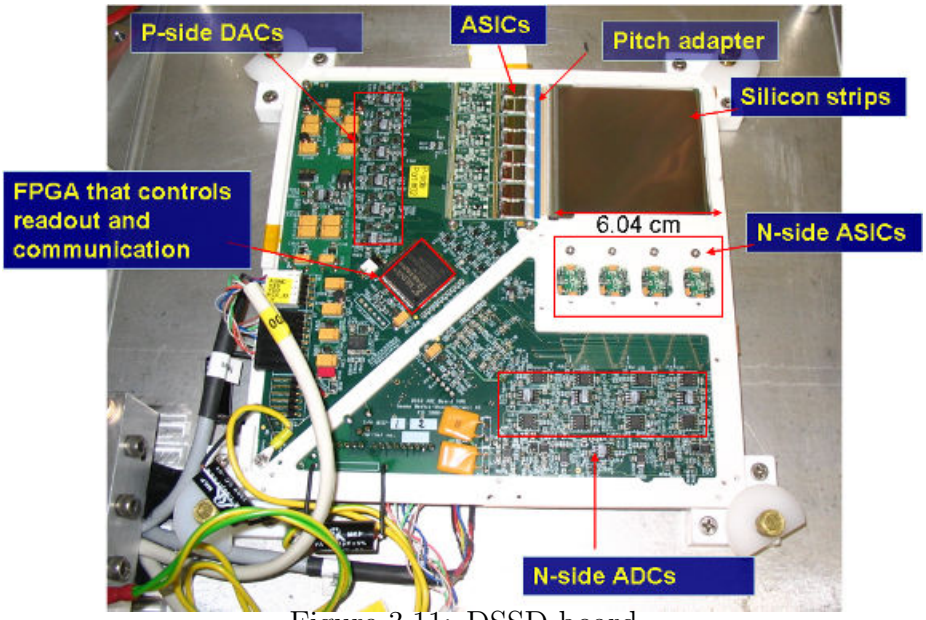

Figure 3.11: DSSD board.

The system has several readout modes. The core series of events common to all readout modes is showin in Fig. 3.12. Serial mode clocks out the slow-shaper analog voltage from each channel sequentially whether that channel has triggered or not. The values are sent through ADCs and then be analyzed offline to determine gamma-ray interactions in the channels. This option is useful to measure the baseline noise, or electronic pedestal, seen on each slow amp. Not only is serial readout slow, but it also increases the chance of missing real events. If an event occurs in a channel after it has been readout, the analog signal on the slow amp is gone by the time of the next readout cycle. The trigger-driven, sparse readout mode reduces the amount of collected data by only reading out channels that have generated triggers.

Sparse readout consists of a few basic steps. When the output of a fast shaper passes the discriminator threshold, a trigger (fixed-width logic pulse) is generated and

the disable late trigger (DLT) flag is set, so subsequent triggers from other channels are ignored. The system waits for the shaping time of the slow amp (nominally 3 μs) and then the sample and hold (S/H) circuitry activates to read out the analog value of the all slow amps whose channels have triggered. This is accomplished by clocking through a list of the list of triggered channels until all of the channels are read out. The S/H values are sent to 12-bit ADCs and then they and the channel addresses are sent to the CROB to be time stamped and put into a data packet. After the readout is completed, a reset pulse clears the DLT, the S/H values, and any trigger flags.

Signals with larger amplitudes cross the threshold earlier than smaller signals. This factor combined with the nominal shaping time of the fast amp means that several channels can generate trigger pulses before the DLT is set. These channels are clocked out one by one until all of the triggered channels have been read.

3.5 Data packet format

Fig. 3.13 shows the format of the data packets sent from the CROB to the PC. These packets must be decoded and sorted to find coincidence locations. For each trigger there are two 32-bit words. The event data is contained in the first word and includes the CROB port (detector side from which it came), strip address, ADC value, and several flags. The EDF flag simply distinguishes the word as an event packet, the LEF flag is set when the packet comes from a trigger channel (and not neighbors), and the MGO flag is set if multiple triggers are set before the DLT is enabled. With the trigger rates for SPECT and tests, the MGO bit is almost always set to 1. The second word, which generally follows the event packet, is the trigger

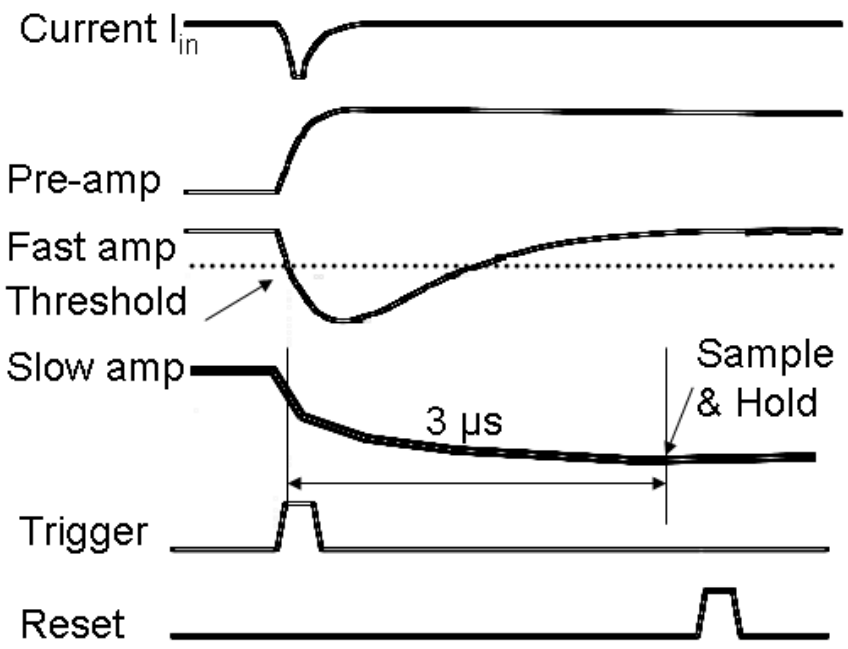

Figure 3.12: Timing diagram of event readout. If the signal from the detector, after having been amplified and shaped, passes the discriminator threshold, a trigger is issued. 3 μs later, the sample/hold circuit polls the slow-shaper output and sends it to the ADC. After all triggers are clocked out, a reset pulse removes all triggers and clears the amplifiers.

timing packet. This packet also contains the CROB port number, which connects it with the event packet, and a 16-bit coincidence time stamp (which runs on an 40 MHz clock). The port number in the second word is always one greater than the port number in the first word apparently because of a programming error in the CROB FPGA. Interspersed through the event and coincidence packets are time stamp packets from an independent 1 kHz (1 ms) clock. With bit-masking, each type of packet can be identified. Occasionally there will be a packet that does not match any of the defined packet formats. These events are deemed to be junk and are discarded in the processing. Also, the event and coincidence packets may be in varying order in the data stream, or a time stamp packet may be sandwiched between

them, so packets must be processed without any assumptions of order. The acquired data are processed to remove junk packets and ensure that each trigger has complete information (address, ADC, CROB port number, and both time stamps).

CROB - NI PCI-6534 packet format definitions:

Port A/0 Most Significant Port
Port B/1 Least Significant Port

Event (30):

	Port A/0							Port B/1							
	MSB						LSB	MSB							LSB
	7	6	5	4	3	2	1	0	7	6	5	4	3	2	1	0
1	<-module (4) ->				<-			Address (11)							->
0	EDF	LEF	mgo	<-				ADC (12)							->

* EDF <=> Event Data Flag
** LEF <=> Leader Event Flag

Coincidence (16):

	Port A/0								Port B/1							
	MSB						LSB		MSB							LSB
	7	6	5	4	3	2	1	0	7	6	5	4	3	2	1	0
1	<-module (4) ->				x	x	x	x	x	x	<-Coincid. (16-12)->					
0	0	0	x	<-	Coincidence (11- 0)											->

Time stamp (16):

	Port A/0								Port B/1							
	MSB						LSB	MSB								LSB
	7	6	5	4	3	2	1	0	7	6	5	4	3	2	1	0
1	r	r	r	r	x	x	x	<-	Time stamp (15- 8)							->
0	0	1	0	x	x	x	x	<-	Time stamp (7- 0)							->

Read-back ():

	Port A/0								Port B/1							
	MSB						LSB	MSB								LSB
	7	6	5	4	3	2	1	0	7	6	5	4	3	2	1	0
1	<-module (4) ->				0	0	0	0	1	0	1	1	0	1	0	
0	1	<-	No. of cfg. bits sent (9)								->	<-RP ->		RB	SCD	LED

* RP <=> Register Pointer
* RB <=> read_bit
* SCD <=> SC data

Figure 3.13: Format of list-mode data packets from CROB board.

3.6 Power supply

A power supply provides high voltage (HV) for the detector biasing and low voltage ($\sim$5 V) for the ASICs and board electronics. A single power supply can power up to four detectors. The front panel of the power supply includes an on/off switch, a reset button (which resets a relay upon loss of power), and two knobs for the positive and negative HV. General instructions for operating the system are found in Appendix A. We know from experience (storm disruption of power) that shutting the power supply off while the HV is on does not damage the detector boards, so rather than buying a battery backup power supply, we installed a simple relay switch. If the current to the power supply is disrupted the relay flips a switch which turns off the power until the relay is manually reset. This ensures that the HV can be turned off before restarting the system.

The current setup of the system is depicted in Fig. 3.14. Two power supplies each power two detectors (two DSSDs in each camera head). This requires two sets of digital isolators and a single CROB. This configuration exhibited the best stability compared to using either power supply alone. However, we later determined this was because of a bad power splitter cable. Thus, in the future, a single power supply and digital isolator could be used for the four-detector system.

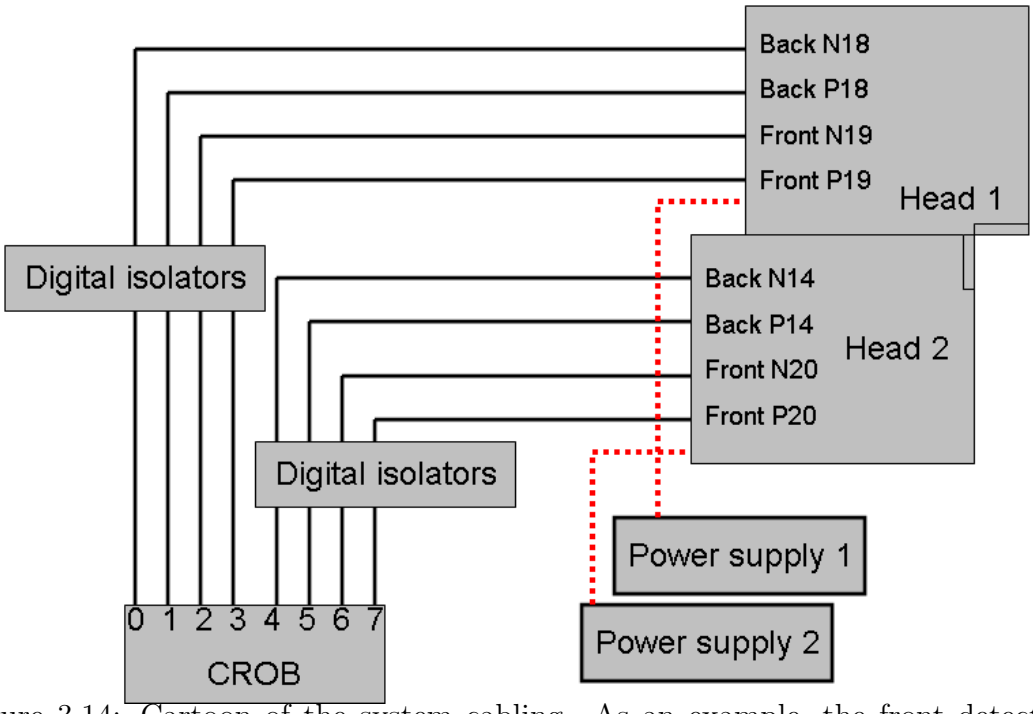

Figure 3.14: Cartoon of the system cabling. As an example, the front detector in head 1 (detector 19) has its P data sent to port 3 and its N data to port 2 on the CROB. In the list-mode data, detector 19 events will have these module numbers.

CHAPTER IV

DETECTOR PERFORMANCE MEASUREMENTS AND METHODS

4.1 Introduction

As the basis of the imaging system, the DSSDs needed to be well characterized and optimized for detection efficiency and stable operation. At the hardware level, we adjusted the bias voltage across the detector and investigated different cooling schemes and their effects. Many more 'knobs' were adjusted at the electronic level (e.g., channel trigger threshold Vth and other DAC biases). And with post-processing software, we determined things like optimal coincidence window, count-rate capability and energy resolution. Several of these measurements were reported in 2009 in a TNS paper [99]. Measurements were made with a number of radioisotopes with low-energy x-rays and gamma-rays. Finding appropriate sources was an important first step.

4.2 Radioisotopes of interest

The detection efficiency for 1 mm thick silicon detectors is low (<5 %) for most nuclear medicine isotope emissions due to its low density (2.33 g/cm^3) and atomic number (Z=14). For ^{125}I emissions (mostly 27 keV), the intrinsic efficiency is higher at around 36 %. Fig. 4.1 shows the fraction of attenuated photons in various thicknesses of silicon. For 1 mm of silicon, the fraction of attenuated photons from photoelectric, Compton, and total interaction processes are plotted. The attenuation fraction rapidly decreases after 40 keV, as does the fraction of photoelectric effect interac-

tions. Imaging at lower energies, while more efficient, also poses problems since the probability of triggering on electronic noise is higher. SiliSPECT was designed to image ^{125}I. A few other isotopes have low-energy emissions, such as ^{111}In and ^{99m}Tc, but imaging with these isotopes is complicated by their higher-energy emissions. Table IV.1 contains a list of relevant isotopes with DSSD-detectable photon emissions. ^{125}I is the main biologically relevent isotope with no high-energy components. ^{123}I can be substituted for ^{125}I. It has the same low-energy x-rays, a shorter half-life, and a human-body penetrating 159 keV gamma. Another isotope of interest is ^{124}I, a PET tracer that also has a large abundance of iodine x-rays. One advantage of ^{125}I is its long (59.5 days) half-life. The long half-life means that many off-the-shelf labeled radiopharmaceuticals are available. It also permits studies with molecules that have very slow biodistribution, such as antibodies. The long-half life also adds some complications.

Because of its longevity and volatility, ^{125}I presents some unique challenges. For instance, animals must be stored in a lead-lined freezer for months before they can be properly discarded. Human exposure to this isotope is problematic because it accumulates in the thyroid gland. To measure the performances of the detectors, we needed sources that were easy to handle and closely mimicked sources we could image in an animal. Free or labeled ^{125}I is generally in liquid form and in a diluted volume. We needed high-activity, point-like sources that were well-contained.

One attractive source was the ^{125}I Brachytherapy seed. We had access to left-over seeds from hospital procedures, and they were safe to handle, since the iodine is surrounded by a laser-welded titanium capsule. A variety of seeds have been devel-

Table IV.1: List of isotopes with low-energy emissions suitable for detecting with 1 mm thick silicon DSSDs [100]. These isotopes are used in medical procedures or are common calibration sources. Some of the isotopes would be much harder to image via SPECT because of high-energy emissions, like ^{124}I.

Isotope, Half-life	Energy (keV)	Intensity (%)	Isotope, Half-life	Energy (keV)	Intensity (%)
^{125}I	∼27.3[a]	126.3	^{111}In	∼23.0	69.6
59.4 d	∼31.0	20.5	2.8 d	∼26.0	13.9
	35.5	6.7		171.3	90.0
				245.4	94.0
^{123}I	∼27.3	71.6	^{124}I	∼27.3	47.7
13.3 h	∼31.0	14.8	4.17 d	∼31.0	9.9
	159.0	83.0		602.8	63.0
	∼500	∼2.0		722.8	10.4
				1300-1700	∼6.0
^{99m}Tc	∼18.2	6.3	^{103}Pd	∼29.0	64.7
6.01 h	140.5	89.0	17.0 d	∼23.0	12.3
^{241}Am	∼14	10.7	^{125m}Te	∼27.3	95.1
432.2 y	∼16-18	12.1	57.4 d	∼31.0	20.0
	∼21	2.9		35.5	6.7
	26.3	2.4		109.2	0.3
	59.5	35.9			
			^{109}Cd	∼22.0	85.2
			462.2 d	∼25.0	16.8
				88.0	3.6

[a] ∼ indicates intensities were summed for energies within 1 keV.

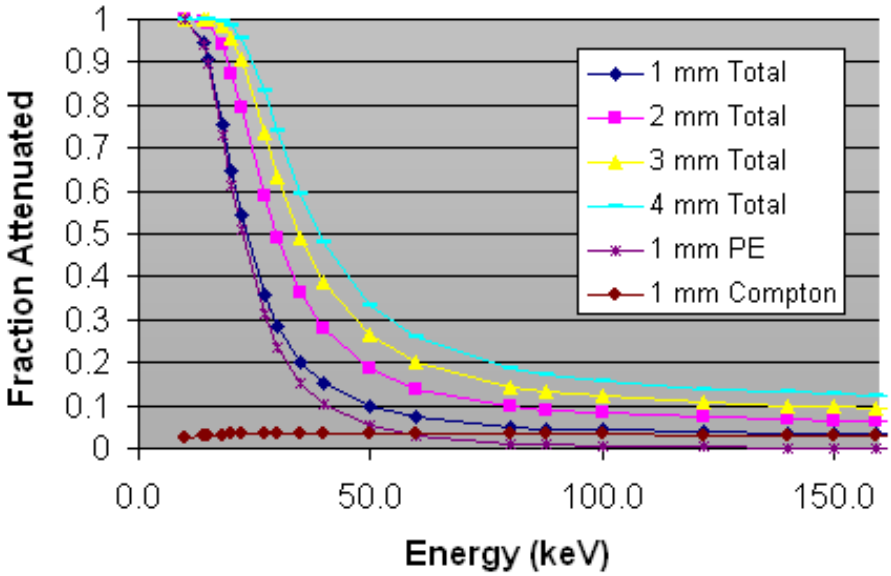

Figure 4.1: Fraction of attenuated incident photons from XCOM data[101]. Attenuation was calculated using Beer's law. Four lines show the absorption vs. energy for four detector thicknesses (1-4 mm), and two lines show the photoelectric and Compton attenuation fraction for 1 mm of silicon. At the low-energies most of the interactions are through the photoelectric effect.

oped over the years for various medical procedures. Most of the seeds use ^{125}I, but low-energy emitting ^{103}Pd and ^{131}Cs are also used now.

We first obtained Oncoseeds (Oncura, Amersham Health, model 6711), depicted in figure 4.2. The Oncoseed design consists of iodine adsorbed onto a silver rod, which is surrounded by a 0.8 mm diameter, 5.0 mm long capsule. Oncoseeds were observed to yield worse uniformity in flood images than purer sources, such as ^{109}Cd (22-25 keV). Many seed designs contain silver, which introduces significant amounts of fluorescence x-rays (22 & 25 keV) into the emission spectrum. So enclosure materials were also a consideration in finding suitable sources. Nath and Chen quantified the amount of silver fluorescence from nine seed designs with a high-purity germanium detector (HPGE) [102]. Figure 4.3 shows the spectra from a 6711 seed. Seed 6711's silver

x-ray components were among the highest, so the average photon energy emitted by a 6711 Oncoseed is less than that of pure 125I. We explored alternate Brachyseeds, as a range of designs exist with different x-ray spectra.

Four of the nine seeds contained resin ion exchange beads, where iodine is absorbed by the beads instead of adsorbed onto silver rods. The spheres are more attractive since a single sphere more closely resembles a point source. The two seeds with the lowest x-ray yield were also the two with the beads. Unfortunately, the DraxImage LS-1 and the Oncura 6702 seeds are no longer manufactured.

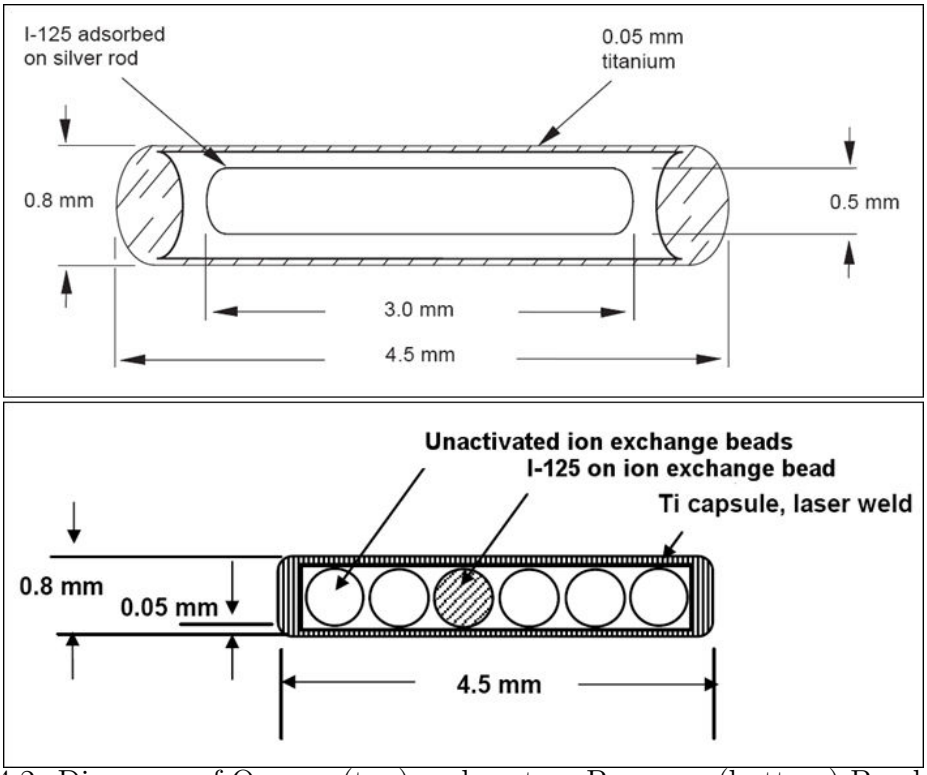

Figure 4.2: Diagrams of Oncura (top) and custom Prospera (bottom) Brachytherapy seeds. In normal Prospera seeds, the middle two beads are gold markers for x-ray imaging. In the custom seed, no gold markers were used, and only one bead was activated with 3.0 $\pm$0.2 mCi of ^{125}I.

The best available option was a seed without silver innards. X-rays from the titanium capsule have energy less than 5 keV, and are not as problematic. We found

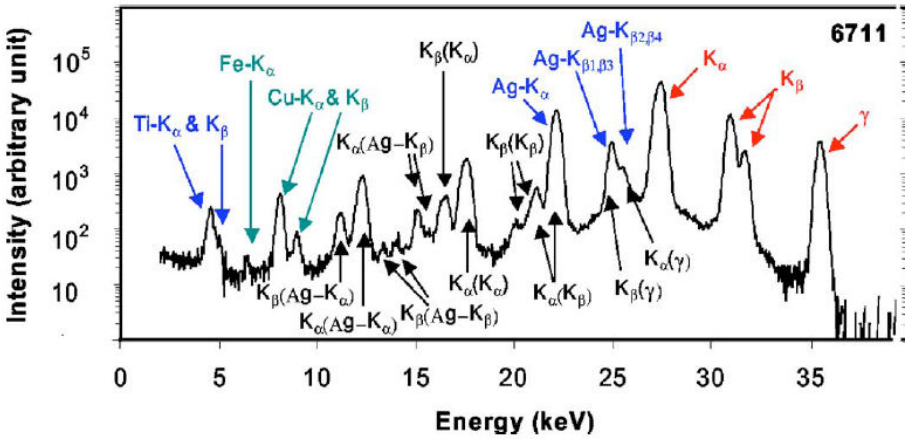

Figure 4.3: Spectrum from Oncura 6711 [102]. The three peaks on the right are from ^{125}I emissions (red). Ag, Cu, and Ti x-ray peaks are labeled accordingly. The majority of peaks are x-ray escape peaks (black). For example, $K_\alpha(K_\beta)$ denotes the escape peak from Ge-K_α x-rays that were created by ^{125}I-K_β x-rays in the Ge detector.

a good candidate in North American Scientific's Prospera design. This design has a similar titanium case, but instead of a metal rod on the inside, resin ion exchange beads are used to soak up the iodine. Normally four ion exchanage beads surround two gold beads, which are used as x-ray imaging markers. NAS made a custom seed where only one of the six resin beads had activity on it. The beads are roughly 600 μm in diameter. Without the silver core, the low-energy spectra for this seed should be less populated with x-rays than in the Oncura seed. We verified this by measuring the seed's energy spectra using a Canberra HPGE detector with the help of Dr. Michael Stabin. We set as low a threshold as possible with the detector and the entrance window (around 11 keV), then counted for ten minutes with the custom seed and an Oncura 6711 seed. Software with the HPGE detector found the peaks and integrated the counts under each peak. We normalized the counts for each result to compare the energy spectra. Uncertainty from counting errors was propagated and

included as error bars ($\pm\sigma$). Results are shown in figure 4.4. The custom seed has fewer counts below 20 keV, and more above 25 keV because there is less attenuation of the ^{125}I emissions without the silver core of the 6711 seed.

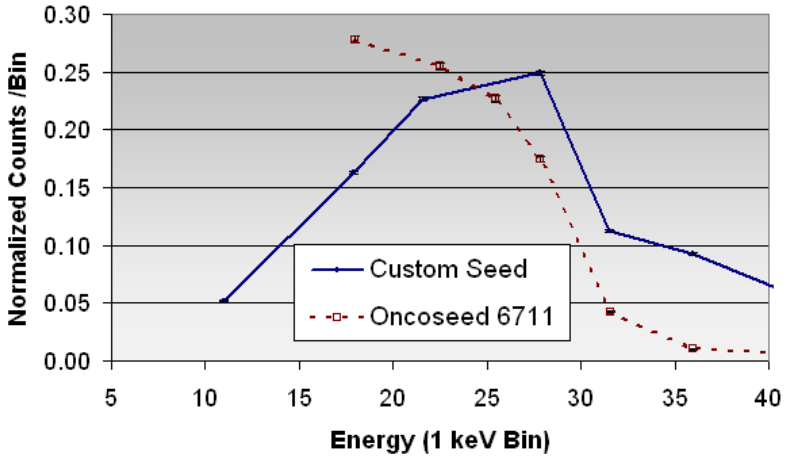

Figure 4.4: HPGE spectra from 6711 and custom Prospera ^{125}I seeds. Because the custom seed has fewer low-energy counts, the thresholds on the detectors can be set higher, ensuring fewer triggers from electronic noise and better trigger uniformity.

The first measurements with the custom seed indicated that the source was confined to a single seed and very point-like. As time progressed, however, we noticed that the seed projections became less point-like and more distributed (Fig. 4.5). In a high-magnification configuration, it was obvious in the projection image that the activity had spread among the neighboring ion exchange beads within the seed (Fig. 4.6). So the "point source" ended up being a multi-nodule blob source. The iodine on the hot seed apparently diffused or volatilized and settled on other beads. It would have been better to only load the seed with a single bead, as free iodine would be more likely to reattach to a single ion exchange bead than the seed walls.

Some other sealed sources were also used in measurements. ^{109}Cd, which mostly emits photons between 22 and 25 keV, and ^{241}Am, which emits 14, 18, and 60 keV

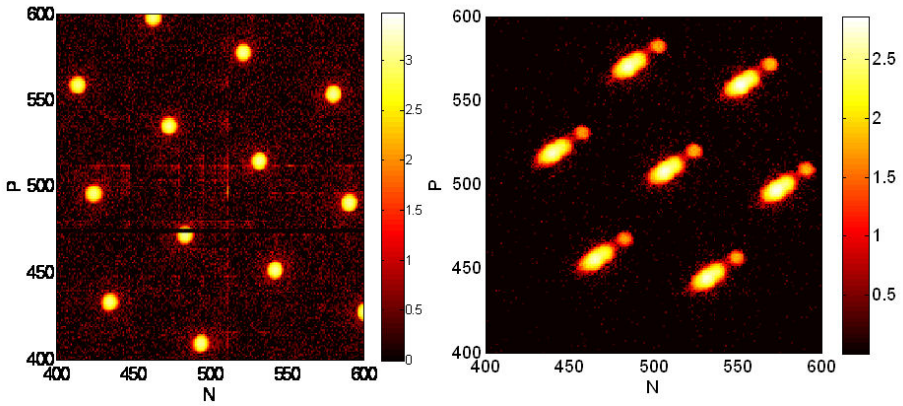

Figure 4.5: Projection images from custom seed when it was first delivered (left) and after several months (right). The seed magnifications are different in the two images, but it is easy to see that the source was confined to a single bead at first, and then started to spread activity among the neighboring beads over time.

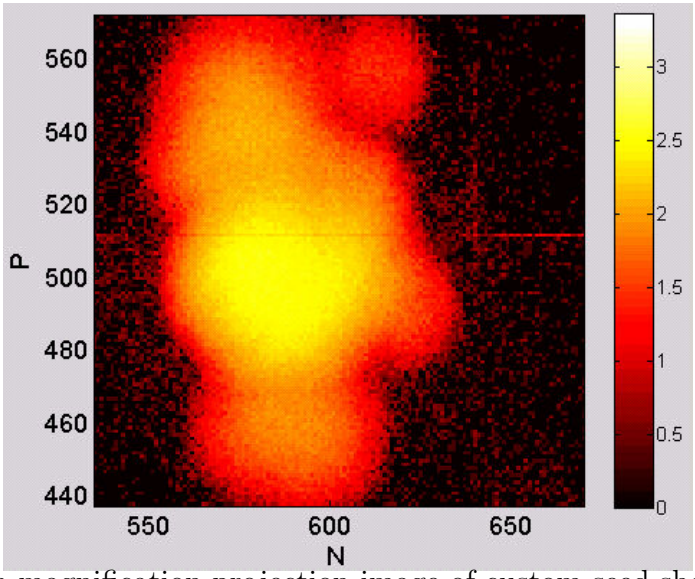

Figure 4.6: High-magnification projection image of custom seed showing the activity distribution among several ion exchange beads.

photons, were used to make flood uniformity measurements and energy calibrations, respectively. ^{109}Cd is a better flood source because the emission energies are closer to ^{125}I. Plus, the greater the emission energy (and detection threshold), the less likely to trigger on electronic noise; uniformity is better for higher energies since a higher threshold can be used. ^{241}Am is useful as an energy calibration source because on most channels two peaks (14-18 and 60 keV) will be distinct.

4.3 Trigger and flood uniformity

Next to stability, trigger uniformity for all channels is the most important detector parameter to optimize. For flood source geometry, all the channels should trigger at roughly the same rates. This condition helps maximize detection efficiency and minimizes false coincidences. The net counting rates for each detector side should also be similar. If one side has a much higher triggering rate, then there is a greater chance that events from the two detector sides will be mismatched. This also means that the effective energy thresholds are different, so either some real events are ignored, or more triggers are generated on one side by electronic noise. Either case is undesirable.

Detecting ^{125}I photons with maximum efficiency requires setting the DSSD discriminator thresholds as low as possible. As the threshold is lowered, the probability of triggering on electronic noise increases. The point at which noise triggers become significant (1 count in 20 ms, or 50 Hz by our current procedure) is called the threshold floor. If the threshold is set below the floor, noise triggers will dominate the system output, which causes real events to be lost to system dead time. Each channel's threshold must minimize the noise trigger rate and maximize the trigger

rate for ^{125}I photons. In the following sections methods are described for equalizing the channel thresholds, and results are given for trigger uniformity improvement and flood uniformity.

4.3.1 Methods for reducing threshold dispersion

Each channel has a trigger threshold offset that varies due to manufacturing process imperfections and tolerances in the amplifiers, capacitors, and other components of the ASICs. We sought to align the offsets of all the channels on both detector sides in order to obtain uniform triggering from ^{125}I emissions. When the relative thresholds are not aligned, there is significant trigger nonuniformity, as seen in the P-side singles histogram in Fig. 4.7. With a highly segmented detector, some amount of charge-sharing is expected, where signals from the charge clouds are induced on more than one strip. The threshold for each channel should be set low enough to collect charge-shared events (13.5 keV for a 50-50 sharing from a 27 keV photon), but not so low as to significantly trigger on electronic noise. To ensure uniform triggering across the combined 2048 channels, trim DACs were set that adjusted each channel's threshold relative to the global, externally-set threshold (Vth). To make the adjustments, we had to first determine the offsets for the channels.

The output of the fast amplifiers cannot be directly probed, so we scan Vth and record the number of triggers at each threshold to find the threshold floor. This was accomplished by iterative adjustments of 4-bit channel trim DACs and 5-bit, ASIC-level DACs. By adjusting the trim DAC on each channel according to the threshold floor array, the dispersion in offsets can be reduced.

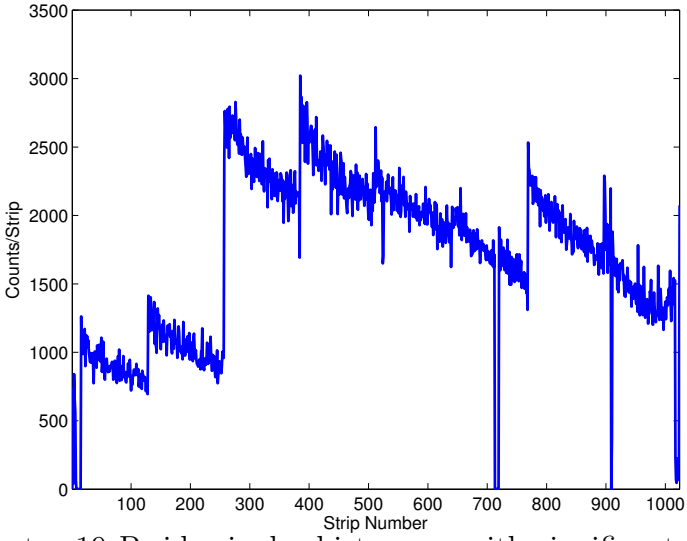

Figure 4.7: Detector 19 P-side singles histogram with significant trigger nonuniformity. The first two chips have a higher relative threshold than the rest. There is also significant variation within the chips, with more counts at the lower channels on each chip. This is the baseline result when no efforts were made to fine-tune the relative threshold offsets. Data was acquired with an ^{241}Am source.

4.3.2 Iterative threshold adjustment algorithm

An iterative algorithm was developed that measures the threshold floor of each channel, adjusts the trims, remeasures, and repeats. The threshold floor dispersion reduces with each iteration. The algorithm consists of the following steps and is illustrated in Fig. 4.8.

- A single channel is enabled and the triggering rate is monitored as the global threshold (Vth) is lowered to determine the level at which it begins to trigger on its own electronic noise. At each Vth value, triggers are counted for a fixed time (generally 20 ms).

- Channels with threshold floor values greater than two standard deviations above the mean of that channel's chip are added to a list of noisy channels and disabled

in the acquisitions. No further effort is made to adjust these channels because the most a trim DAC can move a channel's offset relative to its neighbors is about seven Vth DAC units. If a threshold floor is two standard deviations beyond the mean of the chip, no amount of trimming will move that channel's relative offset to be aligned with the other offsets.

- Trim DAC values are calculated to shift the trigger thresholds towards the mean threshold floor value from the previous scan. If there is a current imbalance (too many positive or negative trims, which can shift Vth out of range), compensating currents are assigned with the ASIC DACs.

- This process is repeated until the threshold floor variance of the whole detector converges (usually less than 1.0). One iteration takes around 30 min when the dwell time for each Vth value is 20 ms.

Each step of the algorithm is detailed below. The concept of a single channel threshold scan is illustrated in Fig. 4.9. As the threshold sinks into the baseline noise, the number of triggers increases until the threshold is on the other side of the DC offset. The offset sits in the middle of the Vth range. The amplifiers accept signals of both polarities (from holes and electrons) and the triggers are set by a threshold crossing. In single-polarity systems, the threshold scan would produce "S-curves," where the trigger rate only increases as Vth is lowered. In this system the trigger peak is symmetric since the signals from noise only extend a certain Vth range in both directions from the offset.

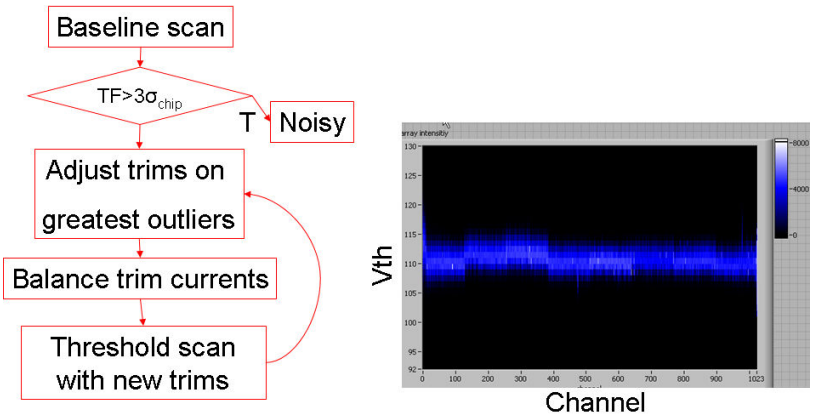

Figure 4.8: Flow chart of the iterative trim adjustment algorithm (left) and threshold scan result for all channels (intensity being the number of triggers, right). The 2nd and 3rd chips are the most offset from the other chips, and some low channels on the first chip are highly offset. Ideally all of the lower DAC values would line up for the N-side and the top values for the P-side.

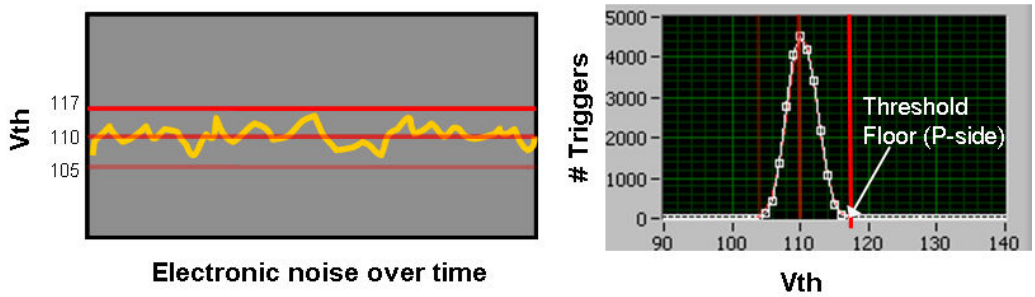

Figure 4.9: Cartoon of threshold scanning (left), where Vth is incrementally decreased after triggers are counted at each Vth value. The electronic noise fluctuates around a DC offset. Triggers are generated for threshold crossings on either side of the offset, thus the threshold scan produces a symmetric Gaussian shape instead of the typical "S curve" (right). Red lines of varying opacity correspond to different Vth values. The solid red line indicates the threshold floor for this P-side channel at Vth=117.

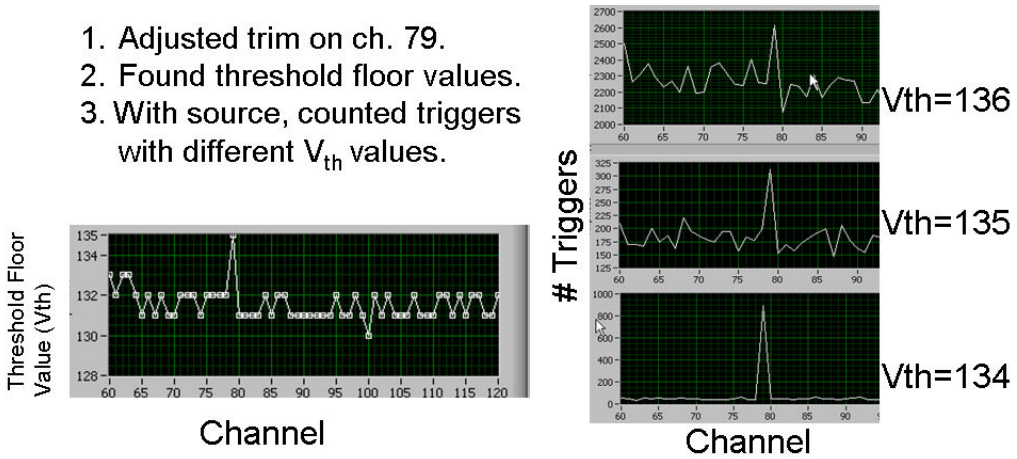

Figure 4.10: Example effect of trim DAC and Vth setting on trigger uniformity. The maximum trim (-7 mV) was placed on channel 79. This adjusted the threshold floor value higher with respect to the other channels to Vth=135 (left). The number of triggers versus channel are shown for different Vth settings (right) with a flood source. When Vth is set at 136, channel 79 has more triggers. When Vth is 134, noise triggers from channel 79 dominate the output.

The algorithm first disables all but the scanned channel with an ASIC mask. The Vth DAC is set to the start of a scan range (starts at low numbers for N-side and high numbers for P-side), and triggers are counted for a set amount of time, typically 200 ms. The threshold floor is found after triggers are collected consecutively for more than two Vth settings. We aimed to align all of the threshold floors, so the full range of Vth (Gaussian peak in Fig. 4.9) does not need to be scanned. However, it is useful to determine if there are any large gain differences among the channels, since large gain differences can also affect the triggering rates. The results of a full DSSD side threshold scan is shown in Fig. 4.8. The 2nd and 3rd chips are offset from the other chips. Other than a few channels on the first chip, the dispersion in threshold floor values is relatively small.

Once the threshold floors are acquired, the trim DACs for each channel must be adjusted in a way to decrease the threshold floor dispersion and increase the trigger uniformity. The trim DACs produced threshold adjustments on the individual channels, but their effect was complex. The individual channel response to trimming was nonuniform, the inter-chip threshold offsets were affected by the trims, and the global threshold displacement from the trims was dependent on the

4.3.2.1 Current compensation

When the trim DAC is adjusted on a single channel, the effect is to move that channel's relative offset with respect to the other channels. It actually causes three connected shifts on a detector side. First is the aforementioned shift. The 4-bit trim DACs range from -7 to 7 mV. With the largest 4-bit trim setting ($\pm$7 mV), the relative offset moves 3-5 Vth units. Second, the trimmed channel's chip also moves with respect to the other chips, though this effect is much smaller. It takes an ensemble of trims ($\sim$30 mV) distributed among channels on that chip to move the chip's offset by 1 Vth unit. And third, the relative position of the global threshold on the Vth range moves with when trims are applied. This effect is quite large. A single 1 mV trim moves the threshold by 10 Vth units. Thus, some balancing must be done among the trims so the signal is not pushed out of range. If the threshold does get shifted beyond the Vth range, there will be no triggers for any Vth value.

Simply equalizing the number of positive and negative trims did not work. We quickly realized that an asymmetry existed where negative trims had a larger impact on moving the three relative offsets mentioned above (channel, chip, and global).

Fig. 4.11 shows the shift in threshold floor for one channel as a different number of alternating trim DACs are applied to channels. For instance, an x-value of 20 means that ch. 0 has +7 mv, ch. 1 has -7 mV, ch. 3 +7 mV, and so on up to channel 20. Negative trims move the effective threshold higher, so the positive slope confirms that negative trims have a bigger impact on the shifts. So when the trims are adjusted, there generally needs to be extra positive current (+trims) added to compensate for the asymmetry, which keeps the global threshold in the useful range (0 to 255).

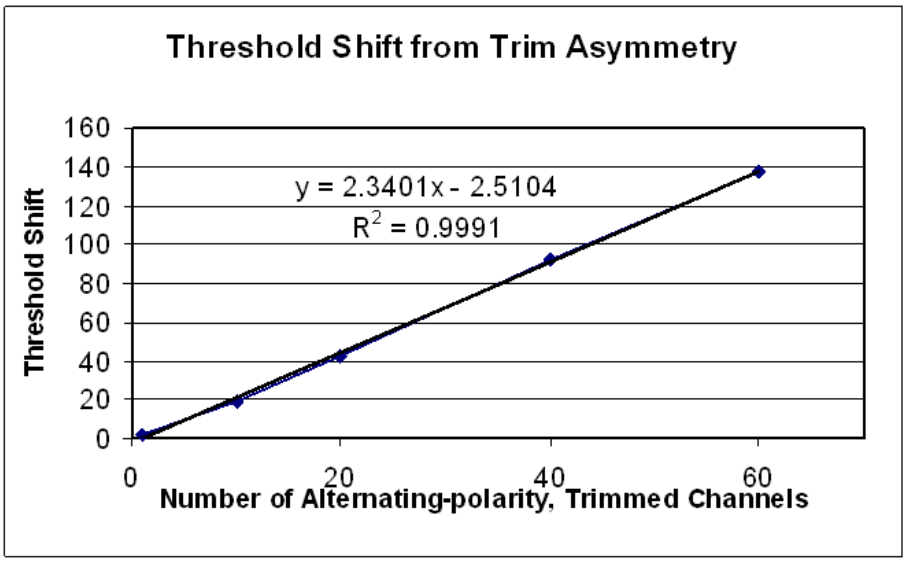

Figure 4.11: Threshold floor shift for a single channel vs. number of alternating-polarity, trimmed channels. An x-value of 20 means that ch. 0 has +7 trim, ch. 1 -7, ch. 3 +7, and so on up to ch. 20. The larger the quantity of negative and positive trims, the greater the effect of the asymmetry.

A convenient place to put the extra trims is on the ASIC-level DACs. These are 5-bit DACs on each chip. We originally thought they were for correcting for intra-chip offsets after the inter-chip offsets had been corrected with the trims. However, all they do is move the global threshold, so they are perfect for adding the extra needed currents. A single ASIC trim has a slightly larger effect on the global threshold than the trim DACs. It too is asymmetric. The conversions between negative and positive

Table IV.2: Effect of trim and ASIC DACs on global Vth.

	+1 trim	-1 trim	+1 ASIC	-1 ASIC
≈Shift (Vth)	9.7	10.0	13.0	14.0

trim and ASIC DACs can all be related through their effect on global Vth, as listed in Table IV.2. Once the sum of negative and positive DACs are tabulated, the number and polarity of ASIC DACs is calculated and turned on to balance the trim currents.

The channel thresholds are trimmed by generating currents which flow through series resistors in a voltage divider scheme. The voltage across the resistors is the required correction to the reference threshold voltage. The threshold reference voltage of each ASIC daisy chain (all the chips on one detector side) is provided with a DAC and a voltage divider with a 10 kΩ resistor from the DAC output to the threshold line and a smaller 1 kΩ resistor from the threshold line to ground.

The current from one compensation circuit cannot flow through the resistors of the other circuits due to the almost infinite resistance of the discriminators. Instead, the total compensating currents of all the trim circuits flows through the pad for the reference threshold voltage of the ASIC, causing an increase in the threshold reference voltage of all the channels of the chip with respect to the other chips in the daisy chain. The same current flowing through the 1 kΩ resistor of the voltage divider causes a further increase in the threshold voltage of all the channels inside the daisy chain. Fig. 4.12 shows the diagram for trim DACs for the XA chip, which is similar to the VaTaGP6. Pacciani et al. explained that the threshold equalization problem would be simpler if each ASIC had its own threshold reference voltage DAC. Instead,

the sum of trims on one chip affects its standing with the rest of the chips instead of just having intra-chip effects.

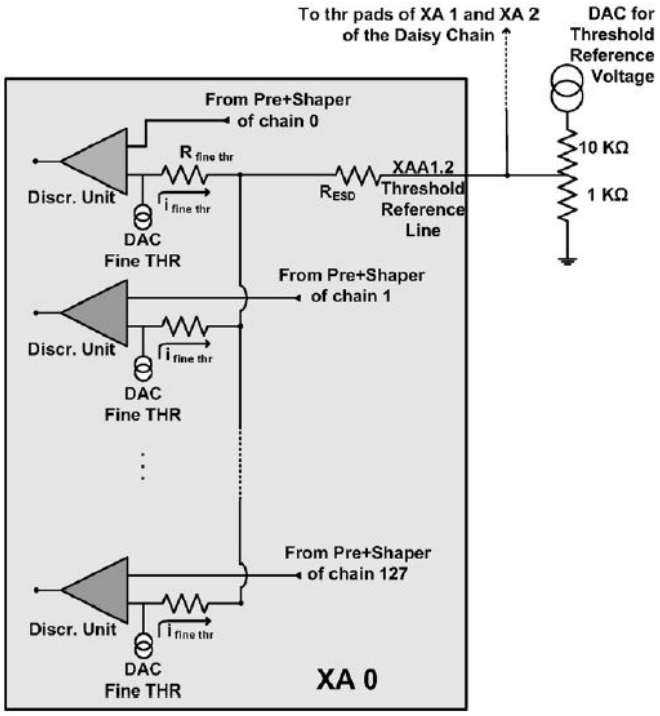

Figure 4.12: Schematic showing how the trim DAC currents are generated and how they change the effective threshold of the discriminators (From [103]). $\mathrm{DAC}_{fine\ thr}$ are the current generators for the 4-bit trims.

Pacciani et al. found a position-dependence for the trims and their effect upon the global threshold shift [103]. This was attributed to the extra line resistance seen by the outer channels. To investigate this effect, a -7 mV trim was placed on one channel. Then the threshold floors were found for each channel on a chip (128 in total). The trimmed channel was incremented, and all 128 channels were again scanned. This let us see if the position of the trimmed channel had any effect on the global threshold. Fig. 4.13 shows the results from these scans. The columns are stacks of threshold floor values when the X^{th} channel was trimmed. The diagonal contains the trimmed channel, which is always higher than its neighbors. The gradient here

was quite obvious; there is a position-dependent threshold shift for the trims. To see if this effect was consistent across strips, we placed a trim on every 16th channel and scanned every 16th channel. Fig. 4.14 contains these results. The right side of the figure shows the mean threshold floor shift for each trim channel, with the chips separated by vertical lines. The difference in Vth units for the chip-level threshold shift is roughly 2 Vth units between a trim at the beginning of the chip versus the end. Since this is a smaller effect, and the results were not consistent across all chips (especially for positive trims, not shown), we do not account for the position dependence when calculating trim current compensation. Results indicated this was an acceptable decision.

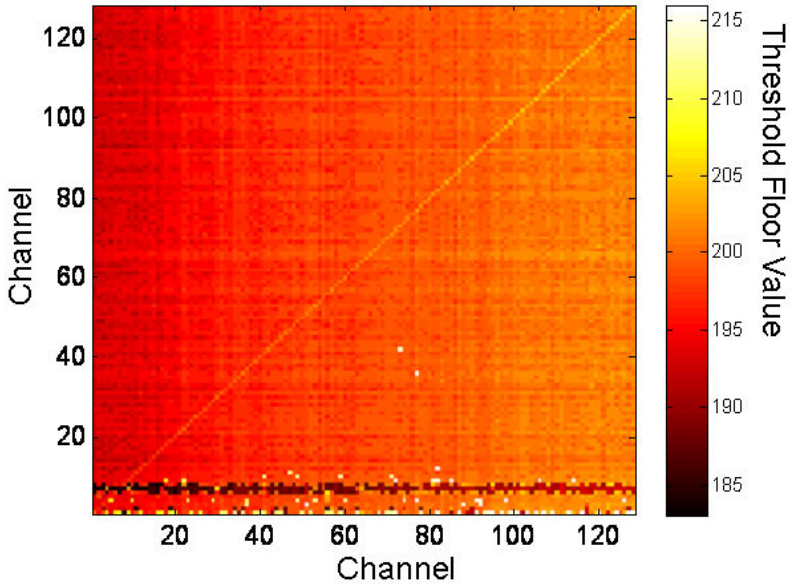

Figure 4.13: Intensity map of threshold floors for trimmed channel vs all channels on a single chip. The columns are stacks of threshold floor values when the Xth channel was trimmed. The diagonal contains the trimmed channel. This demonstrates a position dependence for the trims and the global threshold shift.

To test the compensation algorithm against a range of possible trim combinations, random trims were generated and the threshold floor was measured for a single channel. A scatter plot of the sum of the trims versus the threshold floor value is

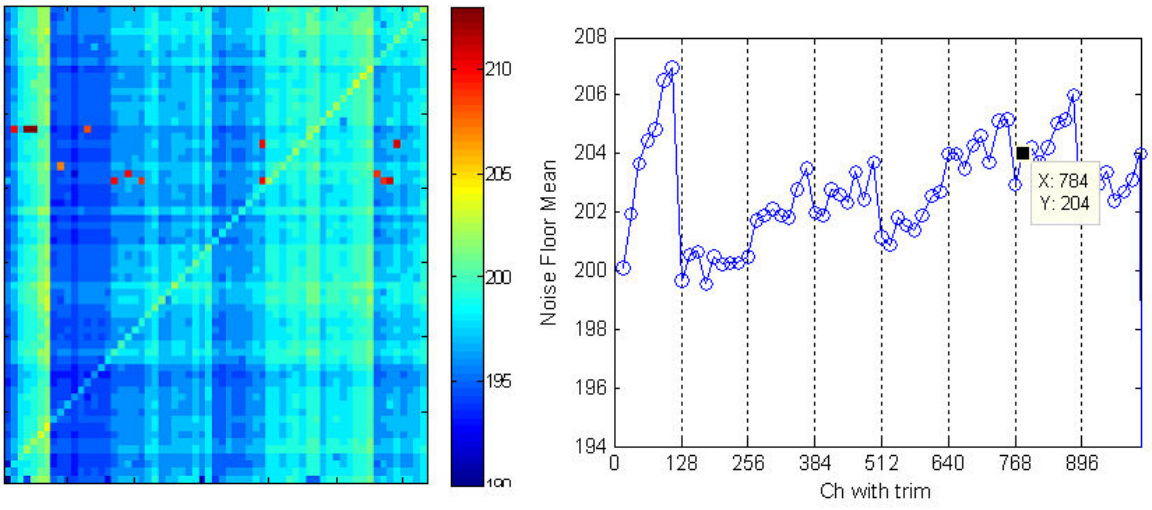

Figure 4.14: Intensity map of threshold floors for trimmed versus rest of (every 16) channels across all chips (left). The mean threshold floor change with trim-channel position was not as consistent as the first chip (shown sparsely here and completely in Fig. 4.13

shown in Fig. 4.15. The points in the scatter plot have a wide distribution, but the important thing is that they are all within the 0 to 255 range of the Vth DAC. Thus, the compensation algorithm worked well enough to keep the new threshold within the operating range.

4.3.3 Iterative trim adjustment results

Fig. 4.16 shows the threshold floor results for a DSSD side for seven iterations of the scanning algorithm. The dispersion in threshold floor values decreases overall through the iterations, but can also increase for a single step. The increase in variance is usually due to a single chip, or a pair of chips being offset. This happens when one chip has a higher trim density than its neighbors, and sometimes has to be manually corrected as the algorithm can get stuck toggling between two off-center chips.

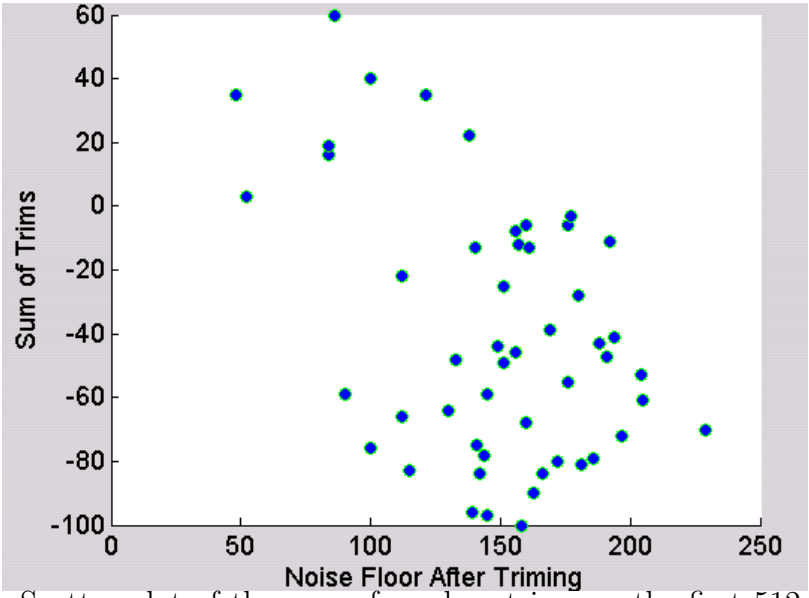

Figure 4.15: Scatter plot of the sum of random trims on the first 512 channels of a detector P-side versus a single channel's threshold floor. A wide range of trims are compensated such that the threshold floor remains within the 0 t0 255 Vth range.

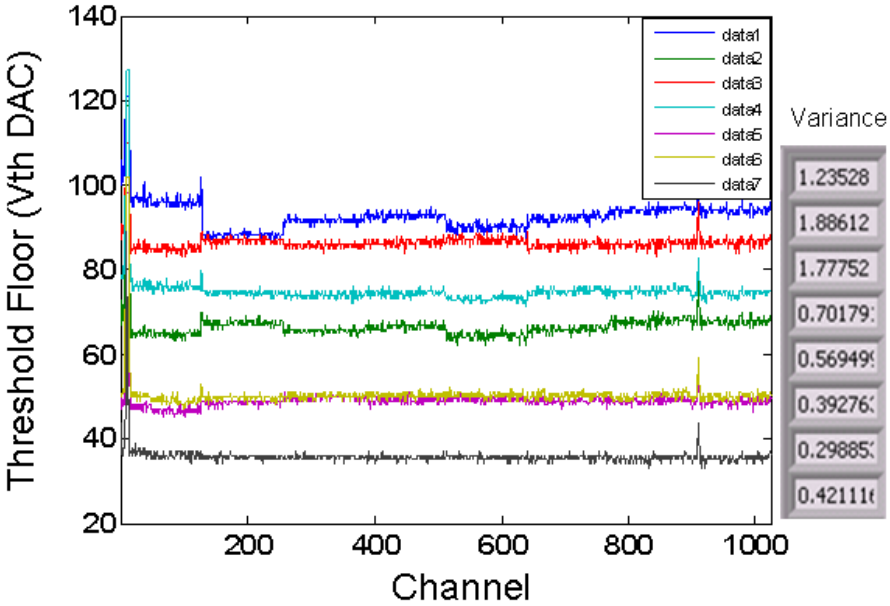

Figure 4.16: Threshold floor value versus Channel for seven iterations of the threshold scanning algorithm. The variance of the threshold floors for all channels is shown in the right column. The latest iteration provided no decrease in the variance, thus the previous iteration's trims were chosen as the best set.

A plot showing the threshold floor values before and after the best trims were applied is shown in Fig. 4.17. Here the range in threshold floor values was reduced from 5 to 3 Vth DAC units, mainly due to the inter-chip offsets becoming better aligned. The trigger counts from a ^{125}I source before and after the trims used in Fig. 4.17 were applied is shown in Fig. 4.18. Before the trims, there were dips in the trigger efficiency at the beginning 20-40 channels of each chip. After the trims were used, the dips were absent in the first four chips and their relative size was reduced on the latter three chips. There were spike-artifacts present in some of the higher channels and edge channels due to the high count-rate. The efficiency dips are not reflected in the threshold floor values, but overall small dispersion in threshold floor values means better trigger uniformity. This is visible in the size of the scatter plots of threshold floor and channel counts in Fig. 4.19.

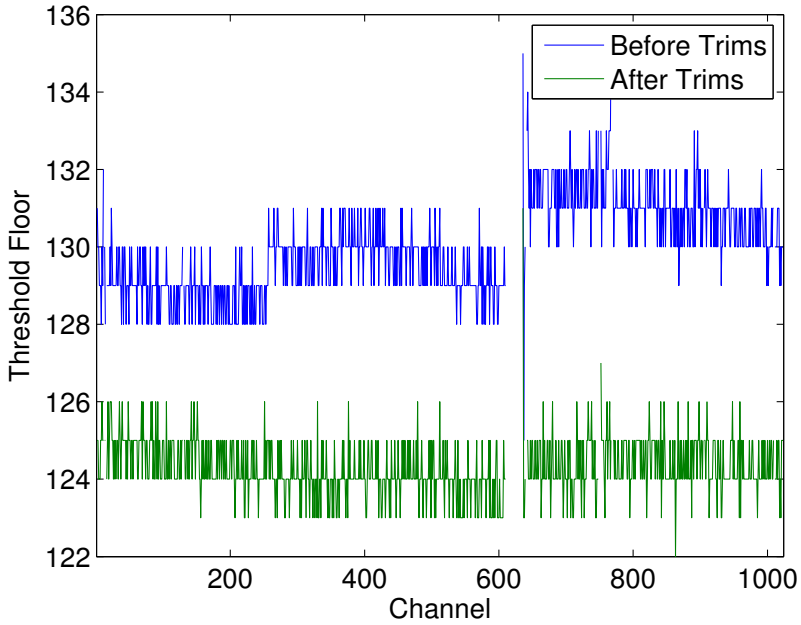

Figure 4.17: Threshold floor value for all N-side channels on a DSSD before and after iterative algorithm. The variance of the threshold floors was 2.27 before and 1.17 after.

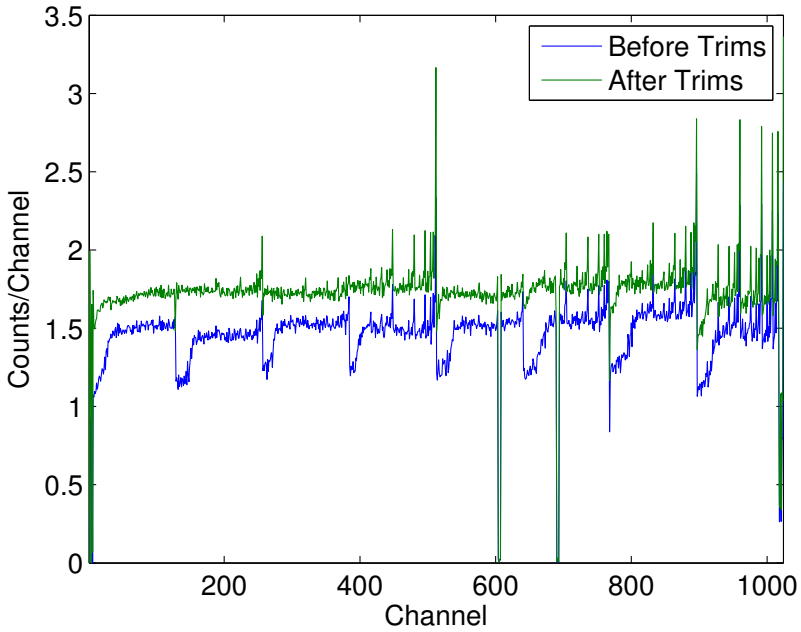

Figure 4.18: Trigger counts for all N-side channels from a ^{125}I source before and after iterative adjustment of the channel trim DACs. The trims greatly improved the uniformity on the first part of all the chips (the dips). The trims allowed a lower global threshold to be set, which increased overall detection efficiency. A slight drawback of this is an increased counting rate, which includes artifacts in some of the higher channels (spikes). Without trims Vth was 100 and with trims it was 200.

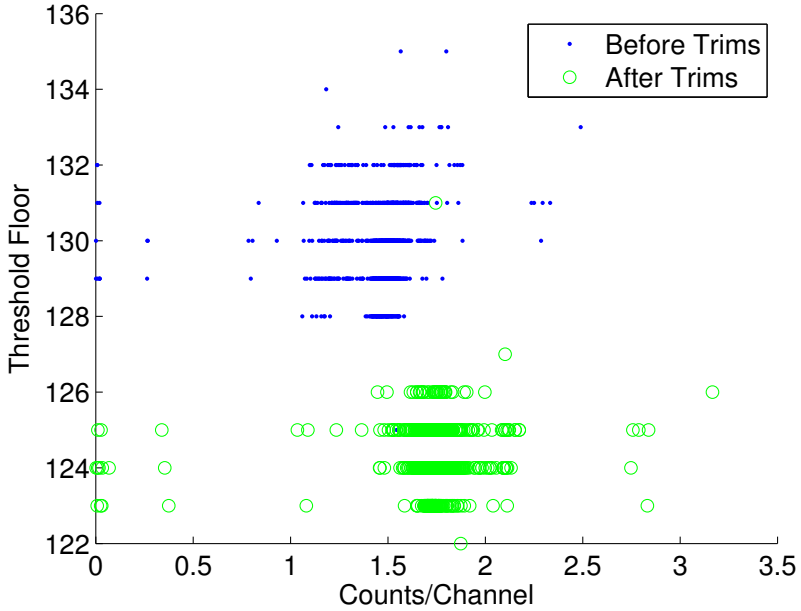

Figure 4.19: Scatter plot of threshold floor values and number of counts/channel. The trimmed channels have a tighter distribution overall, but a few high-count channels due to the higher count-rate artifacts (more in Sec. 4.3.5).

4.3.4 Flood acquisition considerations

After the iterative routine was run for multiple (∼10) iterations, a flood measurement was made. The purpose of flood image acquisitions is to uncover systematic nonuniformities in the detector response and to see changes in the response over time. There are several challenges associated with acquiring low-variance flood images with the DSSDs. To distinguish small systematic nonuniformities from uncertainty due to counting statistics, the number of counts in each pixel must be very high. There would need to be 10,000 counts/pixel to have 1 % variance. To get this many counts per virtual pixel, over 1×10^7 counts/strip would be needed, or 1.024×10^{10} counts total for each side. For a counting rate of 2 kHz, this would take 60 days to acquire. The difficulty of acquiring high-count flood images prevents us from seeing small differences in flood uniformity, but large differences are still detectable with the human eye (which may, as it turn out, be the best measure of uniformity [104]). For example, it is easy to see the nonuniformity in the two flood images shown in Fig. 4.20, even though there are on average less than 30 counts/pixel in the images. So the flood image uniformity can be visually gauged, or to decouple the systematic and statistical uncertainties, the singles events from each side can be considered.

To evaluate systematic counting differences among the channels it is more accurate to examine the data from a single detector side, which have much higher count numbers than the flood image pixels. By histogramming the pixel counts we can at least see if the counts are within the expected Poisson distribution (e.g., Fig. 4.36). The drawback of using the singles data is that the events may or may not be used

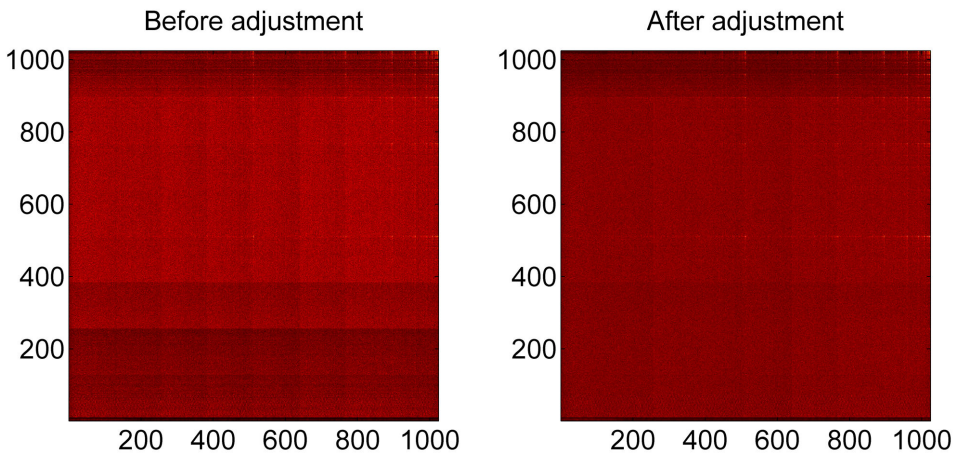

(a) (b)

Figure 4.20: Detector uniformity under ^{125}I flood illumination before (a) and after (b) iterative trim DAC adjustment. These flood acquisitions were taken with detector 18 in the test box (Fig. 4.35).

to form a coincidence event; some of the singles are from noise or the corresponding trigger on the other side was not generated. To minimize this effect, which would artificially inflate the width of the histogram, we make sure that noisy strips are disabled and the background count rate is low before acquiring flood data.

Another requirement for accurate flood measurements is proper geometry. According to clinical gamma-camera calibration standards, a point source should be placed away from the detector at a distance equal to least five times the detector field of view to get a uniform photon flux on the detector [105]. For sources placed closer to the detector, corrections for the count profile falloff should be made. The irradiance from a point source on a detector falls off as $\cos^3\theta$, where θ is the angle from normal at the center of the detector. For a 6.04^2 cm^2 detector and a source

placed 29.6 cm away, the largest angle is:

$$\theta_{max} = \arctan\left(3.02\sqrt{2}/29.6\right) = 0.143 \text{ rad.} \tag{4.1}$$

The maximum difference in irradiance is $100\cdot(1\text{-}\cos^3(0.143)) \approx 3.0$ %. A map of the irradiance fall off from a point source placed 29.6 cm (the distance from the window on the test box to the detector) away from the detector is shown in Fig. 4.21. To see this variation in flood images suffcient pixel counts ($\sim$10k events per pixel to get 1 % variance) would be required to differentiate irradiance fall off from counting uncertainty. If the source was placed at the recommended distance of five times the FOV, the maximum difference in the irradiance is reduced only by a factor of two to $\sim$1.5 %. The projection of the irradiance map gives an estimate of what the singles histogram would look like for one side and is shown in Fig. 4.22. Here the difference in counts from the edge of the detector to the center is $\approx$1.5%. Since it is much easier to acquire high-count singles data, this variation should be easier to observe.

4.3.5 Count-rate related artifact

Above a count rate of 2 kHz per detector side, some clocking-related artifacts are introduced into the data stream. With the apertures in place, these count rates are less likely to be encountered. A stacked detector flood acquisition shows this effect. In Fig. 4.23 the front DSSD image (left), which had a count rate above 3.5 kHz, has visible hot strips and the back detector, which had a count rate below 2 kHz, does not have any noticeable hot strips (thus better uniformity).

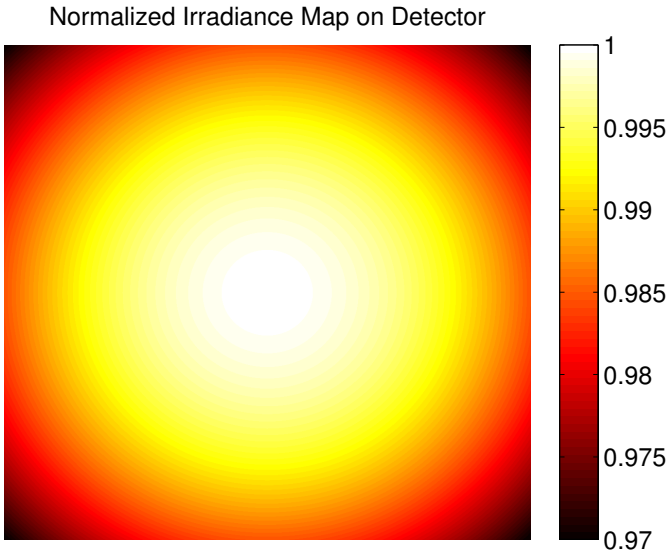

Figure 4.21: Normalized irradiance map on a 6.4 cm^2 detector from a point source placed 29.6 cm away. The maximum difference in irradiance value is $\sim$3 %.

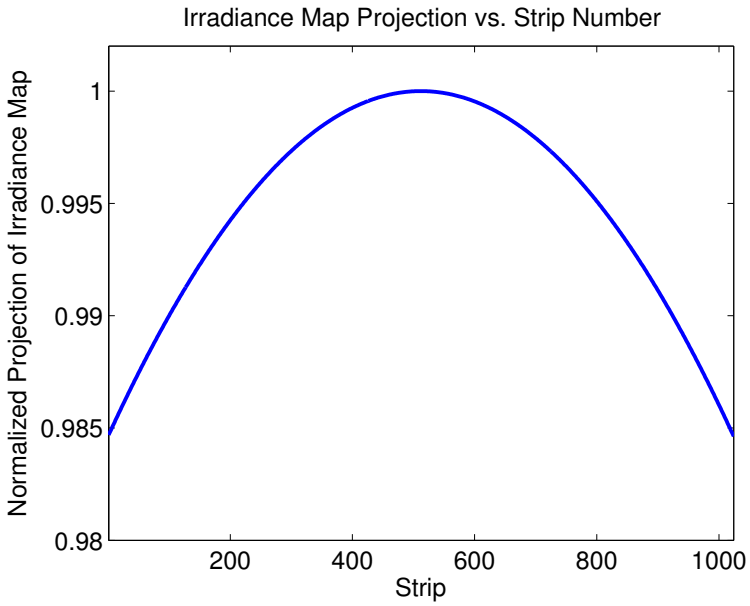

Figure 4.22: Normalized projection of the irradiance map (fig. 4.21), which shows the expected distribution of counts on one detector side from a point source. The maximum difference in counts is 1.5 %. This is the variation one would expect to see in a histogram of the singles events on one detector side with the point source flood geometry from irradiance nonuniformity alone.

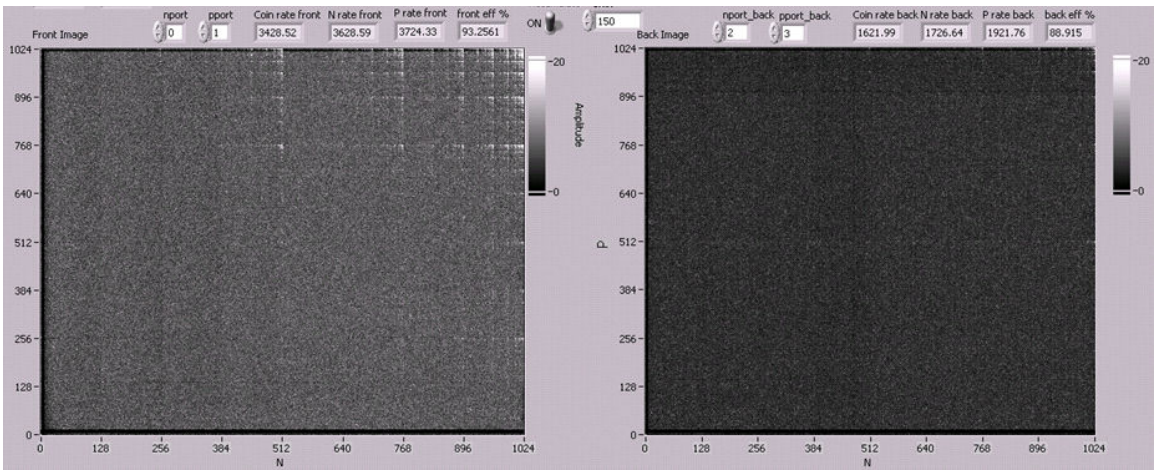

Figure 4.23: Simultaneously-acquired flood image from ^{125}I source. This screen shot is from a Labview real-time coincidence sorting interface. The front detector image, on the left, has side counting rates above 3 kHz and has noticeable 'hot strip' artifacts. The back detector coincidence image (right) experience lower counting rates (< 2 kHz and does not have noticeable artifacts.

We examined the list-mode data of the higher count-rate acquisitions to look for any differences from the lower count-rate data. The hot strips seen in flood images have correlated high-ADC values. Fig. 4.24 shows the ADC histograms for all channels on the P-side of a detector. Hot strips have high-energy ADC tails. In Fig. 4.25 the ADC histograms for two channels are shown, one with a high-energy tail (hot strip) and one without.

The exact cause of this phenomenon is still a mystery, but it could be from the digital clocking signals at high count rates injecting charge over the wirebonds [94]. This retriggering phenomenon is something ASIC designers try to prevent from occurring. It could also be that those channels have many noise triggers because their threshold is set too low. Despite these unknowns, we can reduce the artifacts by removing such events with an ADC cut, shown in the gray area of Fig. 4.25. We set an ADC window

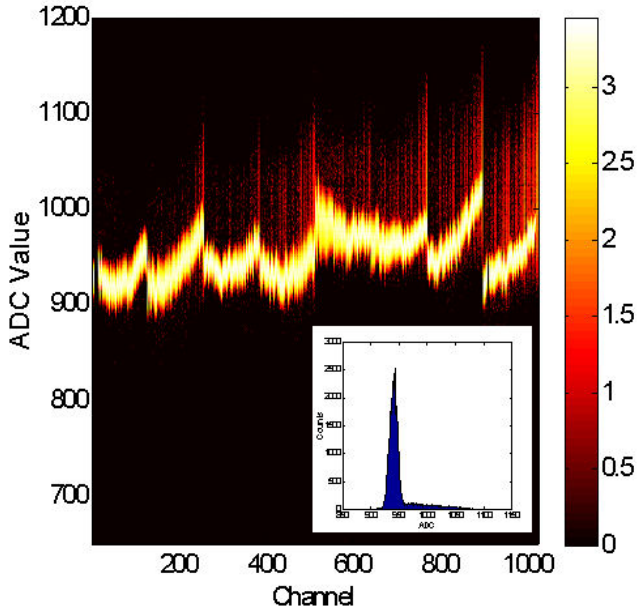

Figure 4.24: 2D histogram of ADC value on the P side of detector 18. The intensity is in a $\log_{10}$ scale. Inset shows ADC spectrum for channel 960. The high-energy tail is thought to come from clocking-related triggers seen only at higher counting rates. Setting an ADC cut around the peak removes the majority of the hot strip artifacts.

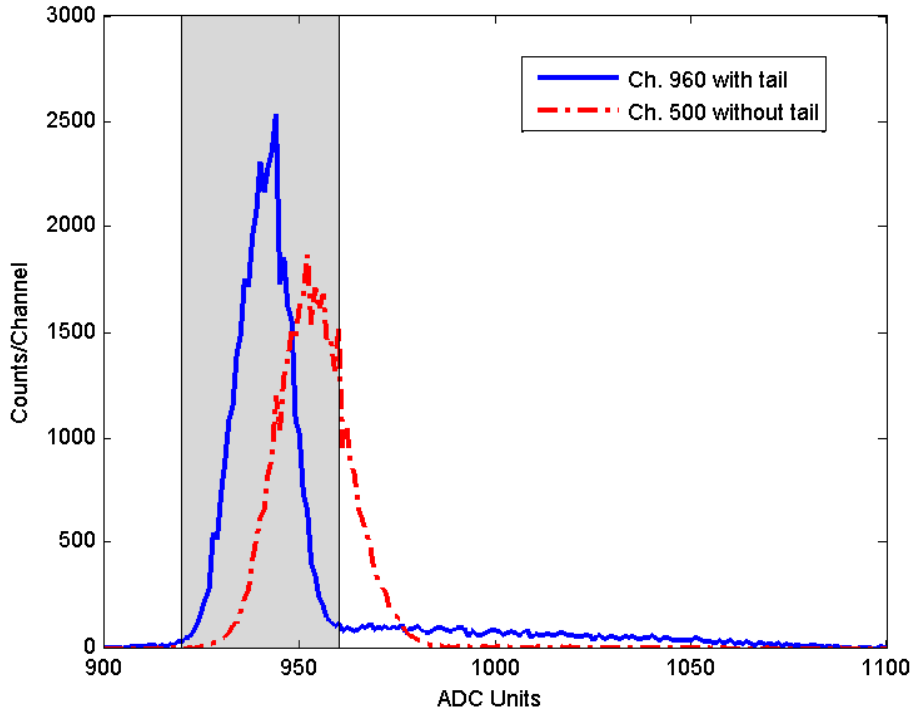

Figure 4.25: ADC histograms for P-side channels with and without high-energy tail artifact. The shaded area shows the ADC cut for channel 960.

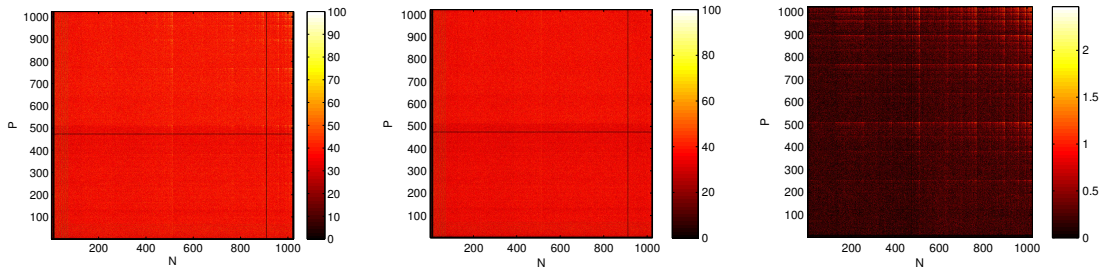

(a) (b) (c)

Figure 4.26: Flood image from an ^{125}I source without an ADC cut (a), where some count-rate related 'hot strip' artifacts are visible, flood image with an ADC cut removing most hot strips (b), and a difference image showing mostly hot strips remaining (c).

for each channel by finding the indices of the ADC peak and then finding the actual FWHM of the peak. ADC values that are three standard deviations outside of the peak value are discarded. An example result from this method is shown in Fig. 4.26.

4.3.6 Measures of flood uniformity

The National Electronics Manufacturer's Association (NEMA) [106] standard for gamma camera performance defines the uniformity, U, as

$$U = \frac{N_{max} - N_{min}}{N_{max} + N_{min}} \cdot 100\ \%, \tag{4.2}$$

where N_{max} and N_{min} are the maximum and minimum pixel intensity values over a certain area. With the DSSDs, the first and last channels on each side are generally disabled. The edge channels are also potentially more susceptible to pickup from various sources of EM noise. The first eighty channels also have artifacts from the bond pads, which are thought to collect more charge because of field effects (Fig. 4.27).

Royle et al. observed similar effects with Sintef-made DSSDs [85]. When the uniformity index is calculated for the useful-field-of-view (channels 80-1023 on both sides), it is termed the integral uniformity (IU). To assess uniformity on a local scale, the maximum difference between pixel intensities in a contiguous region of five pixels in both x and y directions is calculated and called the differential uniformity (DU). The flood image is smoothed by convolving it with a nine-point filter:

$$\begin{bmatrix} 1 & 2 & 1 \\ 2 & 4 & 2 \\ 1 & 2 & 1 \end{bmatrix}$$

before calculating either IU or DU. The DSSDs have some disabled channels, which are removed before smoothing and not included in the uniformity calculations. The five-pixel width for the DU calculation was originally chosen based upon the size of PMTs in gamma-cameras [104]. Gamma-cameras with high DUs generally exhibited "tube" patterns. With the DSSDs we tend to see inter-chip trigger uniformity variations. The DU could be calculated on a chip-by-chip basis to better quantify the largest chip-to-chip dispersion. Results for the NEMA calculations on detector 18 are given in Table IV.3. The difference in IU is significant as the hottest strips were removed with the ADC cut. However, the other values are poor descriptors of the actual systematic non-uniformity since the uncertainty due to counting statistics is so large. For example, if there are on average 26 count/pixel, then the result would have at least $100^*\sqrt{26}/26 = 19.6$ % variation. The results for DU are better than this because

Table IV.3: NEMA uniformity performance measurements on detector 18 flood images before and after trim masks. The IU change is significant, but the DU values are mostly, if not completely determined by counting statistics.

Condition	IU	Mean DU P	Mean DU N
Trims	64.9 %	17.0 %	16.6 %
Trims & ADC cut	36.8 %	16.2 %	16.1 %

the filter slightly improves the uniformity.

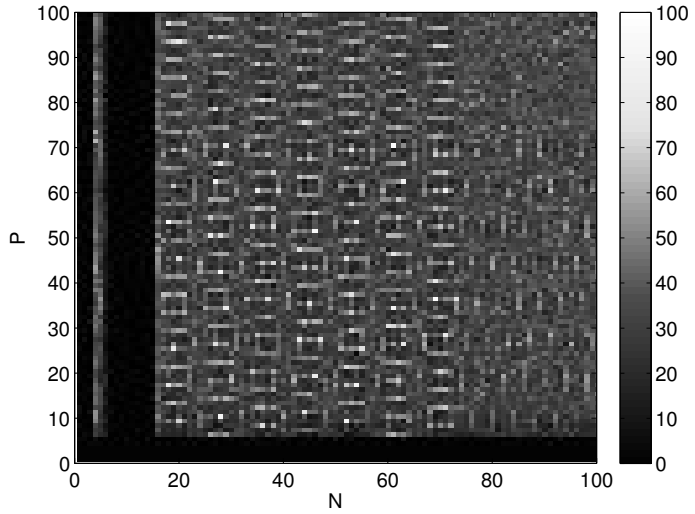

Figure 4.27: Zoomed flood image showing nonuniformities around bond pads. The charge collection in these region is different than the rest of the detector likely because of the size of the bond pads. Eight rows of bond pads extend until roughly the 80th channel on two sides of the DSSD.

Table IV.4 contains the flood data statistical analysis on the singles histograms for three detectors and two different sources. For ^{241}Am, the trims not only increased the detection efficiency, but also unfortunately increased the trigger nonuniformity. For example, P19 has its efficiency increased by over one-hundred percent, and the first two chips are put in line with the others (Fig. 4.28), but the overall dispersion is still slightly worse. ^{241}Am has significantly lower energy photons than ^{125}I, which is responsible for the greater nonuniformity (since the thresholds must be set closer to the threshold noise floors). The results for ^{125}I were more promising, and match

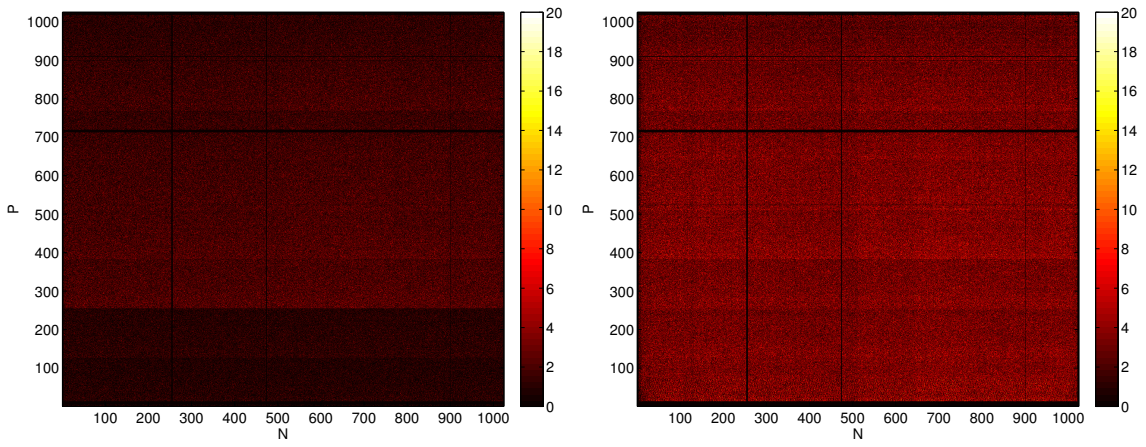

Figure 4.28: Detector 19 flood images from ^{241}Am before (left) and after (right) trims. With the thresholds trimmed it was possible to set a lower global threshold, which doubled the number of coincidences from 1507994 to 3272659. The trimmed threshold was low enough so low-energy x-rays from ^{241}Am were counted.

up with previous interpretations of flood data (e.g., Fig. 4.20). An example of the singles histograms for ^{125}I on P19 is shown in Fig. 4.29. We conclude that the current trimming method is marginally useful for ^{241}Am, but successful for improving the uniformity for ^{125}I, our main isotope of interest. Higher energy photons will produce better trigger uniformity in general. Bare ^{125}I will potentially even look better than from the Oncoseed, which produces many low-energy x-rays. The standard deviation values for the ^{125}I singles' histograms are so large because there are high count-rate artifacts present, and they were not excluded from the calculation.

4.4 Detector stability

Perfect triggering uniformity is not required so long as the triggering rates are stable. Precision is more important than accuracy, since non-uniformities can be accounted for if they are consistently present, but we do want to maximize detection

Table IV.4: Statistics on singles data from detectors 20, 18, and 19 from flood illumination before and after trims. ^{241}Am was used for all three detectors. The trims increased the efficiency in all cases, but actually increased the dispersion. ^{125}I was used as a flood source for detector 18 and 19, and this time the efficiencies dropped slightly after trimming, but so did the dispersion (standard deviation). All parameters were calculated only for channels with counts > 10.

Side/Trims	Mean	Median	Mode	Std. dev.	Kurtosis	Skewness
^{241}Am						
20N/no trims	1.12e4	1.17e4	1.14e4	1649.61	24.64	-3.98
20N/ trims	1.28e4	1.31e4	1.31e4	1744.16	36.01	-5.22
20P/no trims	1.12e4	1.17e4	1.14e4	1649.61	24.64	-3.98
20P/ trims	1.28e4	1.31e4	1.31e4	1744.16	36.01	-5.22
18N/no trims	9.05e2	9.04e2	9.62e2	120.59	25.39	-2.27
18N/ trims	1.51e3	1.51e3	1.62e3	189.52	32.05	-4.05
18P/no trims	1.10e3	1.15e3	1.19e3	213.57	10.94	-2.01
18P/ trims	1.98e3	2.00e3	1.96e3	344.78	19.57	-3.22
19N/no trims	2.52e3	2.50e3	2.36e3	270.04	38.24	-0.15
19N/ trims	5.28e3	5.33e3	5.15e3	703.40	23.44	-3.21
19P/no trims	1.72e3	1.82e3	9.03e2	560.99	2.31	-0.36
19P/ trims	4.15e3	4.21e3	4.07e3	681.65	11.03	-1.52
^{125}I						
18N/no trims	8.37e3	8.52e3	8.22e3	1111.70	40.03	-5.34
18N/ trims	7.83e3	7.95e3	7.71e3	1018.72	44.02	-5.85
18P/no trims	9.04e3	9.15e3	9.07e3	1694.93	24.89	-2.21
18P/ trims	8.51e3	8.69e3	8.81e3	1515.56	25.50	-3.68
19N/no trims	1.63e4	1.62e4	1.60e4	2093.83	53.09	0.75
19N/ trims	1.53e4	1.52e4	1.51e4	1672.46	49.83	-2.79
19P/no trims	1.52e4	1.50e4	1.42e4	4319.34	128.84	8.69
19P/ trims	1.35e4	1.36e4	1.35e4	1969.53	39.59	-2.34

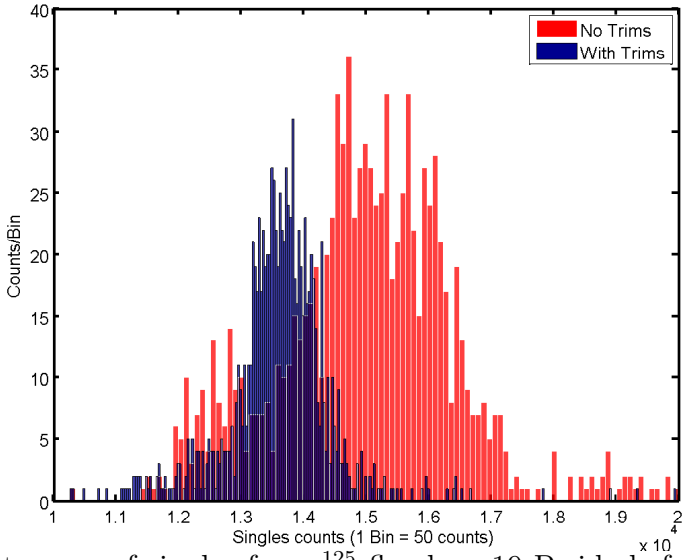

Figure 4.29: Histogram of singles from ^{125} flood on 19 P-side before and after trims (data in Table IV.4). With iodine the trims lowered the efficiency slightly, but greatly reduced the dispersion in counts among the channels.

efficiency. One known source of system instability is temperature variation. Other sources can be external, such as from light, mechanical vibrations, and ripple on the power line. There are also potential internal sources of interference (and thus instability) on the detectors boards themselves, such as the readout clocks inducing false triggers. This section includes efforts to maximize detector stability and results from stability measurements.

4.4.1 Temperature control

Stable operation is essential for detector measurements, and a big source of instability is temperature variation. The ASIC chips produce heat, which warms the surrounding material and detector crystal. Heat travels through the wire bonds onto the bond pads of the detector strips, increasing the leakage current. The various

amplifier gains and offsets also change with temperature, so it is important to ensure constant temperature, especially during data acquisition. We explored several methods for temperature control, and also found that the room temperature can play a big role in detector stability.

In his book on semiconductor detectors[98], Spieler derives a relation between the leakage current and temperature, T,

$$I_R \propto T^2 \exp\left(-\frac{E_g}{2kT}\right) \tag{4.3}$$

where k is Boltzmann's constant and E_g is the bandgap energy of the detector material (1.12 eV for silicon). The ratio of leakage current at temperatures T_1 and T_2 is

$$\frac{I_R(T_2)}{I_R(T_1)} = \left(\frac{T_2}{T_1}\right)^2 \exp\left[-\frac{E_g}{2k}\left(\frac{T_1 - T_2}{T_1 T_2}\right)\right]. \tag{4.4}$$

Without any form of cooling, the temperature within the detector box reached 49° C. With high-end, PC-fan forced-air cooling the temperature stabilized around 36° C when the room temperature was 29.5° C. As temperature increases, it is easier for charge carriers to gain enough thermal energy to jump the band gap, increasing leakage (or dark) current. Noisy channels will trigger more and potentially swamp the system output (around 300 kHz). This creates large output files (if acquiring list-mode data) and causes real events to be lost amid the system dead time. Reducing the temperature by 13° C lowers the leakage current to two thirds of its original

value, as can be seen in Fig. 4.30. Greater levels of cooling offer exponential decreases in leakage current. Thus, our first attempt looked at cooling the detectors below room temperature. K-type thermocouples (Omega) were taped inside the camera head boxes. The thermocouple wires were attached to a National Instruments thermocouple module that connects to a computer via USB.

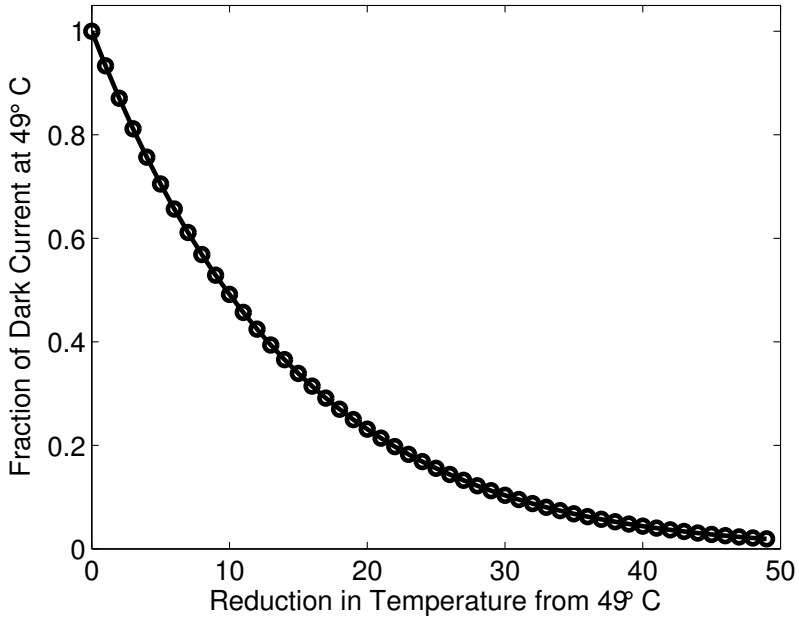

Figure 4.30: Leakage current vs. temperature reduction as estimated by equation 4.4.

We investigated using gas from liquid nitrogen (LN2) boil-off to cool the detectors and ASICs. While this approach easily lowered the temperature in the box, our setup made it difficult to reliably control the temperature. As the volume of LN2 decreased in the dewar, the flow of cool nitrogen gas also decreased, so the temperature would creep up unless the valve was further opened. Furthermore, we had to be careful to avoid condensation on the detector board. The cooled box was brought up to room temperature slowly by reducing the flow of gas. This prevented moisture in the air from condensing in the box as long as inert nitrogen flowed. To avoid engineering a flow-controlled cooling system, and to avert recurring costs from a consumable

commodity, we used fans to blow room-temperature air across the detectors. Plus, the reduction in the common-mode noise (pedestal width during auto-trigger readout) was small, indicating that noise in the system is not dominated by leakage current.

Inlet and outlet holes were machined into one plate of each detector box. The inlet hole is large enough to cover both detector boards. Hoses clamp onto machined aluminum boxes which protrude from the detector boxes, and are connected to high-volume PC fans. A hose is also attached to the outlet box so as to prevent any outside light from entering the detector boxes. We achieved temperature stability (without respect to the room) by using forced air cooling.

Room temperature shifts of up to 4° C were observed in the Peterson lab. This lab is directly connected to the building air handler, so the temperature tends to fluctuate with the outside temperature. A plot showing a decrease in temperature as the night progresses is shown in Fig. 4.32. Temperature changes as low as 1° C can change the detector triggering rates, as displayed in Tab. IV.5. The fluctuations in the room temperature caused the shift in triggering rates on the detector N-sides. Why the N-sides on both detectors displayed a larger triggering rate change with temperature changes than the P-side is not known. The N-sides of DSSDs are in general noisier because of the more complicated strip structure (P+ stops between N+ strips).

Moving the detector system to the small-animal imaging lab in the VUIIS building improved overall temperature stability. The lab temperature fluctuated, but the range was not as wide (roughly 3° C compared to 5° C). An example plot of the small-animal lab temperature is shown in Fig. 4.32. The DSSDs have operated in the small-animal

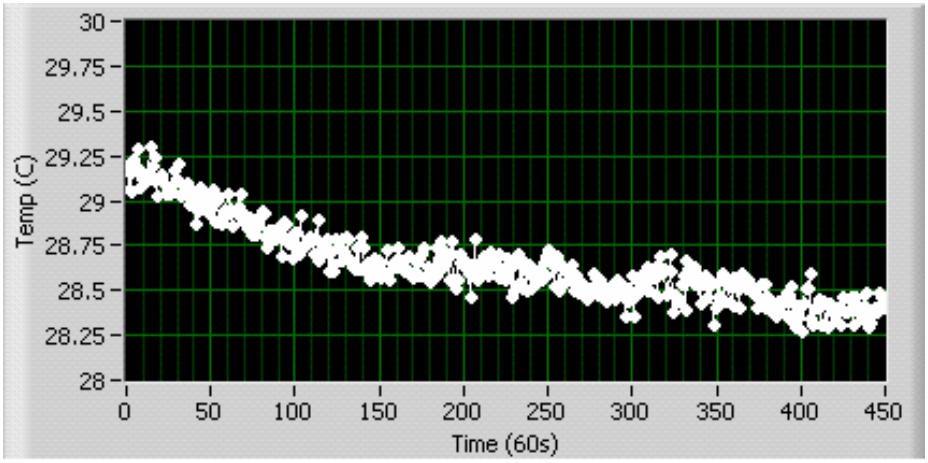

Figure 4.31: Temperature vs. time in the Peterson lab (S1403 Medical Center North)). Data was measured every minute. The acquisition process started in the early evening and the temperature decreased in the lab through the night.

Table IV.5: Detector triggering rates vs. lab temperature. Flood data were acquired for 30 min with a 60 min break in between for a total of five acquisitions. The table values are all in kHz.

DSSD Side	30 min	120 min	210 min	300 min	390 min
P19	1.12	1.13	1.13	1.13	1.13
N19	1.18	1.15	1.13	1.09	1.06
P18	0.71	0.71	0.71	0.71	0.71
N18	0.70	0.69	0.68	0.66	0.65

lab for months at a time without major stability problems. At most, some thresholds need to be slightly adjusted and ASIC masks re-downloaded to achieve previously-seen triggering rates for a given source. Given the range of temperature-sensitive components in the detector system, and the fact that these detectors are operating at room temperature with some amount of leakage current, this level of stability was deemed acceptable.

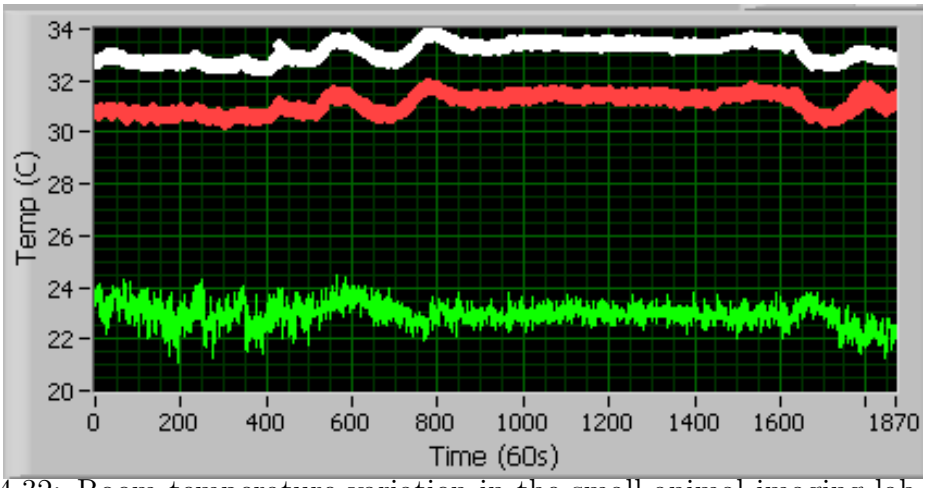

Figure 4.32: Room temperature variation in the small-animal imaging lab. The red trace is for camera head 1, white for camera head 2, and the green for the ambient room temperature. Data was acquired every minute.

4.4.2 Sequential-day flood acquisitions

Flood acquisitions were acquired with detectors 18 and 19 running simultaneously on sequential days in a stacked configuration. Detector 18 was in the back position, and 19 was in the front. A ^{109}Cd source was placed approximately 35 cm from the center of the front detector. Thresholds were adjusted so the channels triggered below the 22 keV x-ray. During each 417 min acquisition the temperature remained stable within 0.5° C. In the first acquisition there were 17 N-side channels and 34 P-side channels disabled. The second acquisition required a larger chunk of N-side channels

to be disabled (25 total). To compare these measurements, the number of triggers on each side of detector 18 were histogrammed for each channel. The mean counts per channel (nonzero count-channels) on the P-side data were 2.63×10^3 and 2.61×10^3, and on the N-side the means were 2.52×10^3 and 2.53×10^3. The percent difference and associated uncertainty were then calculated.

The uncertainty of the calculation is found from the error propagation formula [107], which gives the uncertainty (standard deviation) of a measurement that is a function F of two measurement sets, N_1 and N_2 (or any number of independent variables), to first order.

$$\sigma_F = \sqrt{\left(\frac{\partial F}{\partial N_1}\right)^2 {N_1}^2 + \left(\frac{\partial F}{\partial N_2}\right)^2 {N_2}^2} \tag{4.5}$$

The percent difference calculation is simply:

$$\mathrm{PD} = 200 \cdot \frac{N_1 - N_2}{(N_1 + N_2)} \pm \sigma_{PD}. \tag{4.6}$$

The uncertainty in a given channel's counts is, according to Poisson statistics, $\sqrt{N}$, where N is the number of counts. Solving for σ_{PD} with Eq. 4.5 yields:

$$\sigma_{PD} = \frac{400}{(N_1 + N_2)^2}\sqrt{N_1 N_2^2 + N_2 N_1^2}. \tag{4.7}$$

Figures 4.33 & 4.34 show the stability data with the associated uncertainty. The central line is the mean, and the surrounding lines are the 1- and 3-σ levels. The N-side performs as well or better than that predicted by statistics, with 68% of

channel-count-differences falling within 1σ, and 99.6% falling within 3σ. The P-side peforms slightly worse, but this is largely due to lower-counting efficiency in the last chip, which has lower gain. The effective threshold for that chip needs to be moved relative to the other chips. Both sides show very good stability over one day, with most channels having less than 5% difference between-day stability.

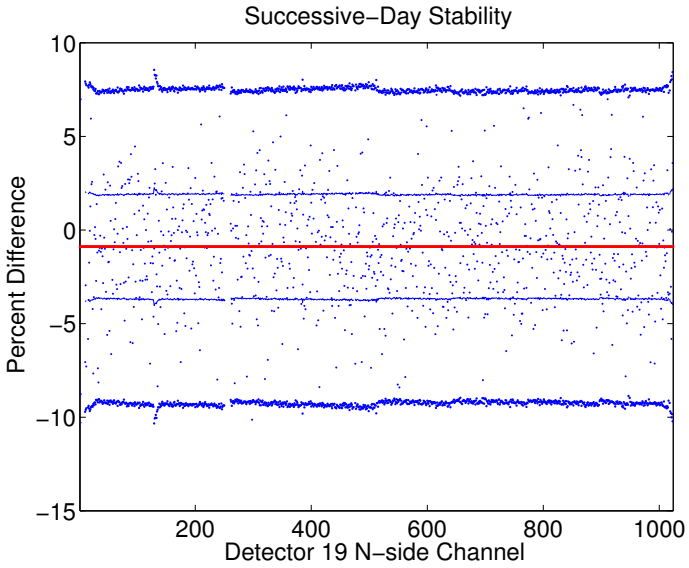

Figure 4.33: Detector 18 N-side percent difference between two successive-day flood acquisitions for all channels. The 1σ (68%) and 3σ (95%) levels are drawn around the mean percent difference. 68.0% of the channels were within 1σ and 99.6% were within 3σ.

As mentioned before, eight more channels on the N-side had to be disabled before the second acquisition began. These channels were triggering on noise and would have otherwise used up the system bandwidth if left enabled. It is not clear why these channels started triggering since the temperature stayed relatively constant near the detector frames. The N-side has been observed to drift more with temperature (Fig. 4.31 and Table IV.5). As the temperature decreases, the triggering rates on the N-sides also decrease. The phenomena of a few channels suddenly triggering at high

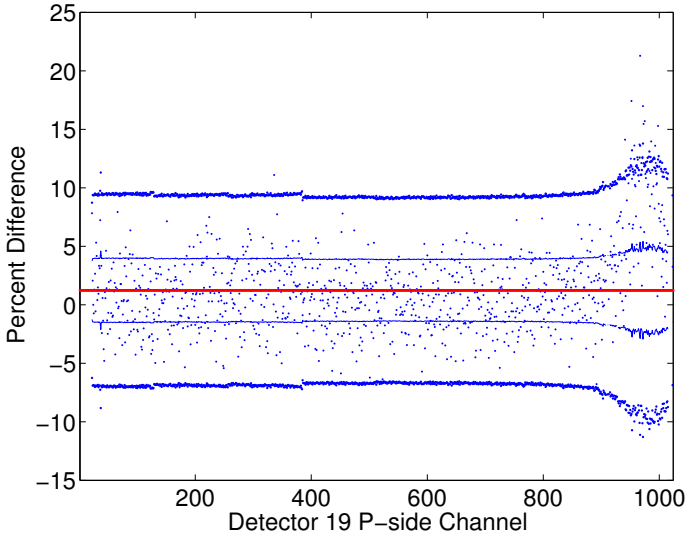

Figure 4.34: Detector 18 P-side percent difference between two successive-day flood acquisitions for all channels. The 1σ (68%) and 3σ (95%) levels are drawn around the mean percent difference value. 63.4% of the channels were within 1σ and 97.6% were within 3σ.

rates has been seen many times. Generally one enables as many channels as possible, which works for one acquisition, but then some of the channels start triggering on noise, so they must be disabled again. Channels found noisy (even if only once) should be disabled permanently since they exhibit low triggering stability.

4.5 Detector efficiency

The silicon DSSDs are only practical for photon imaging up to around ∼50 keV because of their low stopping power (low-Z (14) and low-density (2.33 g/cm^3)). Stacking these detectors boosts the total system detection efficiency without significantly altering the point spread function (PSF) on either detector. This section consists of three parts: a Monte Carlo simulation, measurement of a single DSSD intrinsic efficiency, and analysis of coincidence sorting efficiency. Total detection efficiency for

a DSSD includes the loss associated with coincidence sorting, as some good events are always discarded if one detector side has a higher triggering rate than the other. Some events can also be discarded by using the ADC information associated with each event. This can help remove events from noise and scatter if an appropriate energy window is selected.

Detector efficiency is important to know for a number of reasons. If the measured efficiency is far from the theoretical prediction, then we can look for and reduce sources of inefficiency, such as too-high thresholds. The intrinsic detection efficiency is defined as the number of detected photons divided by the number of photons incident upon the detector:

$$\epsilon_{intrinsic} = \frac{N_{detected}}{N_{incident}}. \tag{4.8}$$

The number of incident photons is given by the solid angle subtended by the detector, $\Omega/4\pi$, times the number of emitted photons, N:

$$N_{incident} = \frac{\Omega}{4\pi} \cdot N. \tag{4.9}$$

N is a product of the activity, A (Bq), acquisition time, t (s), and a factor, P, giving the number of photons emitted per decay. P is $\sim$1.05 for ^{109}Cd because ^{109}Cd emissions include a 3.6% 88 keV gamma-ray and 99.4% 22-26 keV Ag K x-rays, plus a few other low-probability emissions that sum to 1.05 photons/decay.

The solid angle subtended by a square detector makes a four-sided pyramid shape. An analytical expression for a point source perpendicular to the center of the detector

face is [108]:

$$\Omega = 4 \arcsin\left(\frac{\alpha\beta}{\sqrt{(4d^2+\alpha^2)(4d^2+\beta^2)}}\right), \tag{4.10}$$

where d is the distance from the detector to the point source, and α and β are the side lengths of the base of the pyramid (detector side lengths). Since the DSSDs are square, the equation simplifies to:

$$\Omega = 4 \arcsin\left(\frac{\alpha^2}{4d^2+\alpha^2}\right). \tag{4.11}$$

MCNP5 [109], a general purpose radiation transport code, was used to check eq. 4.11. The distance, d, between the detector and point source was changed and the detector side length, α, was kept at 6.0 cm. The detector and source were surrounded by a vacuum in the simulation to better match the analytical calculation. The point source isotropically emitted 1 billion ^{109}Cd photons for each simulation. Pulse height (F8) tallies were used to estimate the solid angle and the intrinsic detection efficiency. The F8 tally gives counts per emitted photon in user-defined energy bins. The first bin (called the ϵ bin) of the tally contains all of the photons that were incident upon the detector but did not interact. The summation of all of the bin values (including ϵ) yields the solid angle (what fraction of isotropically emitted photons are incident upon the detector). The summation of the real energy bins divided by ϵ gives the intrinsic detection efficiency. Since the detector has a low-energy threshold near 15 keV, energy bins below 15 keV in the simulation results were not included in the summation. There were not many counts in the low energy bins, anyway. Table IV.6

Table IV.6: Solid angle results from the analytical expression (eq. 4.11) and Monte Carlo simulations. The bottom row contains results for the geometry of the experimental measurement.

α (cm)	d (cm)	Analytical $\Omega/4\pi$	MCNP5 $\Omega/4\pi$	% Difference
6	1	3.564×10^{-1}	3.555×10^{-1}	0.065
6	10	2.631×10^{-2}	2.626×10^{-2}	0.045
6	20	7.005×10^{-3}	7.044×10^{-3}	0.139
6	30	3.152×10^{-3}	3.135×10^{-3}	0.133
6	40	1.780×10^{-3}	1.771×10^{-3}	0.128
6.04	29.6	3.279×10^{-3}	3.286×10^{-3}	0.053

contains the results from the calculations and simulations for the solid angle. No MCNP5 result has a difference from the analytical result greater than 0.2 %. Thus, the analytical expression was deemed trustworthy and used later in error analysis calculations.

The MCNP5 geometry was modified to better model the real experiment, which is shown in Fig. 4.35. The source was placed on the test box entrance window, which is centered directly over the detector 29.6 ± 0.5 cm and is the visible black circle in the right image. The detector size was increased slightly to 36.48 cm^2. Air was included to incorporate the small attenuation low-energy photons experience as they travel from the source to the detector. The fraction of emitted events incident upon the detector is reduced by ∼1 % when air is included ($N_{incident}$ reduces from N·3.286×10^{-3} in a vacuum to N·3.248×10^{-3} in air). With the 15 keV energy threshold, MCNP5 yields an intrinsic detection efficiency of $1.568\times10^{-3}/3.286\times10^{-3} = 47.7$ %.

The source used in the efficiency measurement was a 3.0 mm-diameter thin disk of ^{109}Cd (Model GF-109-M, Isotope Products, CA). The cadmium is deposited in a

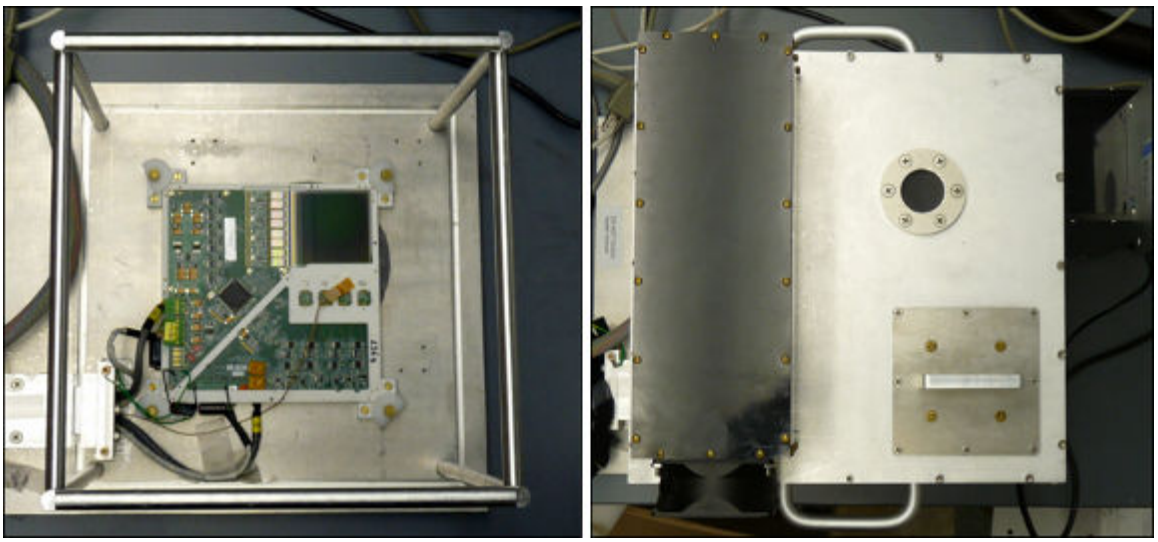

Figure 4.35: Photograph of detector test box without (left) and with (right) light-tight lid. The black circle in the right photograph is the window used for point source flood measurements.

thin layer less than 0.5 mm thick. The source activity was 3240 kBq $\pm$ 3.1 % on Jan. 1st, 2004. Closed-form expressions for the solid angle of distributed sources seldom exist, but a point source approximation can be made. The difference in solid angle subtended by a detector from a disk source versus a point source is less than 1 % if r $\leq$ 0.1D, where r is the disk radius and D is the source-detector distance [110, page 354]. So a point source approximation can be made as long as source-detector distance is at least five times the diameter of the largest source dimension. In this measurement the source-detector distance is roughly one hundred times the source diameter.

Detector 20 was used in the test box for the efficiency measurements. Flood data was acquired for 416.7 minutes. The The N-side had much better trigger uniformity (as seen in Figs. 4.36 & 4.37). The P-side had significant triggering nonuniformity across channels and chips. The better trigger uniformity on the N-side also gave it

better detection efficiency. 6.73×10^6 events were detected on the N-side, and 5.99×10^6 events were detected on the P-side. The total number of counts in the coincidence image was 5.48×10^6, so some good N-side events are being discarded because they do not have matching P-side events. The nonuniformity indicates that some channels' thresholds are too high. The other possibility is that the channels with higher triggering rates are triggering more because their thresholds are set below the electronic noise floor. Before acquiring data the source was removed and the counting rate was $\sim$5 Hz total for both sides, so it is unlikely that the nonuniformity is due to excessive noise triggers. It is likely the former option: some channels are not fully triggering on real events, causing an overall decreasing in detection efficiency. Background events are mostly thought to come from cosmic rays and naturally occurring radioactive isotopes found in the lab paint, concrete, etc. So for the efficiency estimate, the side with the best uniformity is the side whose total number of events we use in the calculation.

The equation for intrinsic detector efficiency with the solid angle included is

$$\begin{aligned} \epsilon_{int} &= \frac{N_{det.}}{N \cdot \frac{\Omega}{4\pi}} \\ &= \frac{N_{det.} \cdot \pi}{N \cdot \arcsin\left(\frac{\alpha^2}{4d^2+\alpha^2}\right)} \end{aligned} \tag{4.12}$$

And the uncertainty associated with ϵ_{int} is

$$\Delta\epsilon_{int} = \sqrt{\left(\frac{\partial\epsilon_{int}}{\partial N_{det.}}\right)^2 \Delta {N_{det.}}^2 + \left(\frac{\partial\epsilon_{int}}{\partial N}\right)^2 \Delta N^2 + \left(\frac{\partial\epsilon_{int}}{\partial d}\right)^2 \Delta d^2 + \left(\frac{\partial\epsilon_{int}}{\partial \alpha}\right)^2 \Delta\alpha^2} \tag{4.13}$$

The errors for each variable are given in Table IV.7. The acquisition time, t,

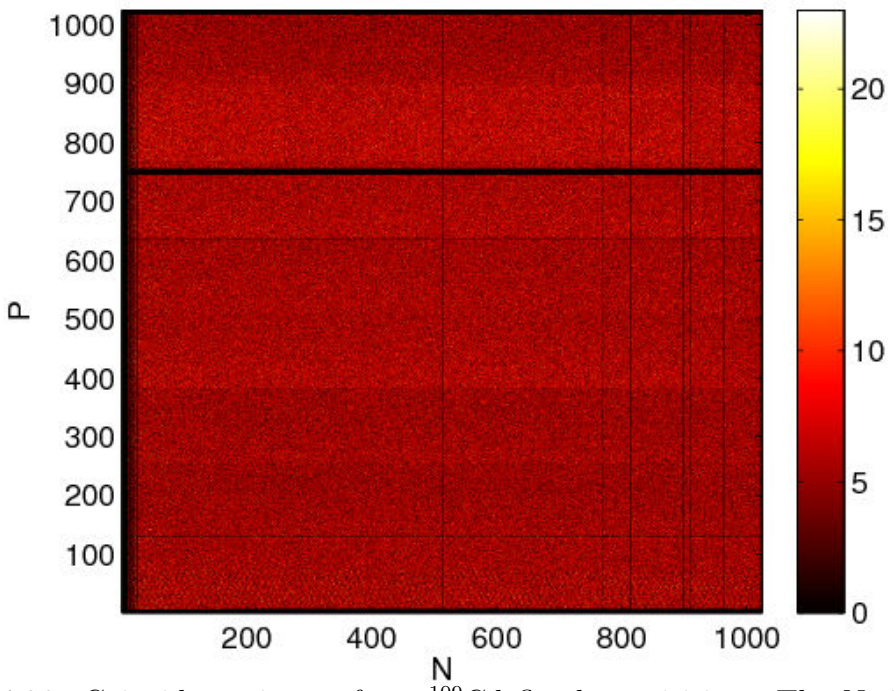

Figure 4.36: Coincidence image from ^{109}Cd flood acquisition. The N-side displays much better trigger uniformity than the P side, as it almost is completely within the bounds of the Poisson distribution based on the mean counts.

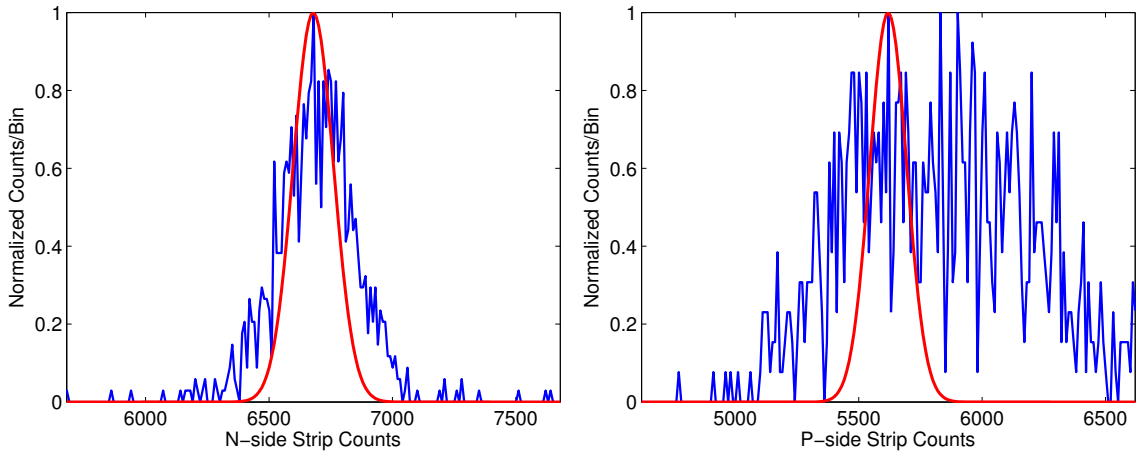

Figure 4.37: Histogram of strip counts for N- and P-side of detector 20. 4.37(a) contains the N-side histogram and 4.37(b) shows the P-side data. The distribution in N-side counts falls much closer to the expected Poisson distribution (red curves) than the P-side.

and photons/decay constant, P, are assumed to have very little error. The source activity has a tolerance of 3.1 %, which carries through to the the uncertainty in N. The number of emitted photons, N is assumed to have a $\sqrt{N}$ uncertainty since photon decay is a Poisson random process. The uncertainty with the source activity dominates the Poisson counting uncerainty for large values of N. The total uncertainty for N is calculated by adding the relative errors in quadrature, then converting to an absolute error in N.

$$\begin{aligned} \Delta N_{\%} &= \sqrt{\left(\frac{100 \cdot \sqrt{N}}{N}\right)^2 + (3.1\%)^2} \text{ (add relative errors)} \\ \Delta N &= \frac{N_{\%}}{100} \cdot N \text{ (convert back to absolute error)} \end{aligned} \tag{4.14}$$

Table IV.7: Sources of error in detector efficiency measurement.

Variable	Abs. Error (Δ)	Error Source
$N_{det.}$	$\sqrt{N_{det.}}$	Counting statistics
N	see Eq. 4.14	Mostly activity uncertainty
d	2 mm	Multiple ruler measurements
α	2 mm	Possible frame occlusion of DSSD

There were 27 disabled strips on the N-side, so the expected number of singles is $(997/1024)\cdot 0.477\cdot N_{incident}$. $N_{incident}$ should be reduced by roughly 1 % because of air

Table IV.8: Detector efficiency measurement values.

Acq. Time (m)	# Decays	N (photons)	$\Omega/4\pi$	$N_{incident}$	$N_{det.}$
416.675	4.814×10^9	5.084×10^9	3.286×10^{-3}	1.671×10^7	6.73×10^6

attenuation. The calculated $N_{incident}$ is then 1.654×10^7 photons. So the number of expected singles is $(997/1024)\cdot0.477\cdot1.654\times10^7 = 7.683\times10^6$. The actual number of singles was 6.73×10^6, making the measured efficiency $6.73\times10^6/1.654\times10^7 = 40.8$ %. Since a background scan was not taken after the source acquisition, we could not subtract any background contribution, though it has been observed to be low (around 6 cts/s for one detector side). If we assume that average background rate, it reduces the efficiency by less than 1 %.

Solving the partial derivatives of equation 4.13 in Matlab and using the results of Tables IV.7 and IV.8 gives the measured efficiency and its uncertainty:

$$\begin{aligned} \epsilon_{int} &= \frac{N_{det.}\cdot\pi}{N\cdot\arcsin\left(\frac{\alpha^2}{4d^2+\alpha^2}\right)} \pm \Delta\epsilon_{int} \\ &= 40.75 \pm 4.62\ \% \end{aligned} \tag{4.15}$$

The measured intrinsic efficiency (eq. 4.15) is reasonably close to the expected value based on the MNCP simulations (47.7 %). Three main factors could cause a decrease in the efficiency: charge-sharing among strips, system dead time, and attenuation in the thin inactive oxide layers and metal strips on the surface of the detectors. Charge-sharing is more evident in adjacent-strip ADC histograms for higher-energy photons. This follows in that the higher-energy the gamma-ray, the larger the number of electron-hole pairs produced. Since the charge cloud is initially larger, there is greater chance that the charge induced on the strips will be shared among several strips as the cloud drifts, diffuses, and self-repulses. If many events were charge-shared, we would expect to see an abundance of triggers from neighboring strips in

the list-mode data. If we histogram the N-side sequential-event address difference, we see the distribution of events shown in Fig. 4.38. There are more counts in the lower address-difference bins than the higher bins because of the combinatorics of the calculation. It is more likely for two randomly selected addresses to have a difference that is small. For there to be a large difference both addresses have to come from opposite ends of the range. A spike would be present in bin 1 if there were many double-triggers from charge-shared events. The spike that appears to be in bin 1 is actually in bin 0 (same sequential channel) and is predominantly from noise triggers on channel 25 (the bump in Fig. 4.39). Since the distribution in addresses is random, we conclude that the majority of the counts in the efficiency measurement are from single photons with charge not shared among strips.

Losses due to dead time increase at higher counting rates. The fraction of events lost to dead time (using the equations and model described in Sec. 4.7.1) for a 269 Hz signal is only 0.36 %. This moves the experimental efficiency slightly closer to the simulated efficiency, as would including losses from inactive layers in the DSSDs not modeled in MCNP5.

We repeated the intrinsic detection efficiency measurement with the same configuration, but this time included a background scan. The results are summarized in Table IV.9. The acquisition was for half the time since the error from the counting statistics is dwarfed by the other uncertainties.

There were 23 disabled strips in the second efficiency measurement. The calculated $N_{incident}$ is 7.26×10^6 photons. The number of expected singles is 3.38×10^6. The count histogram and background counts are shown in fig. 4.39. The measured efficiency is

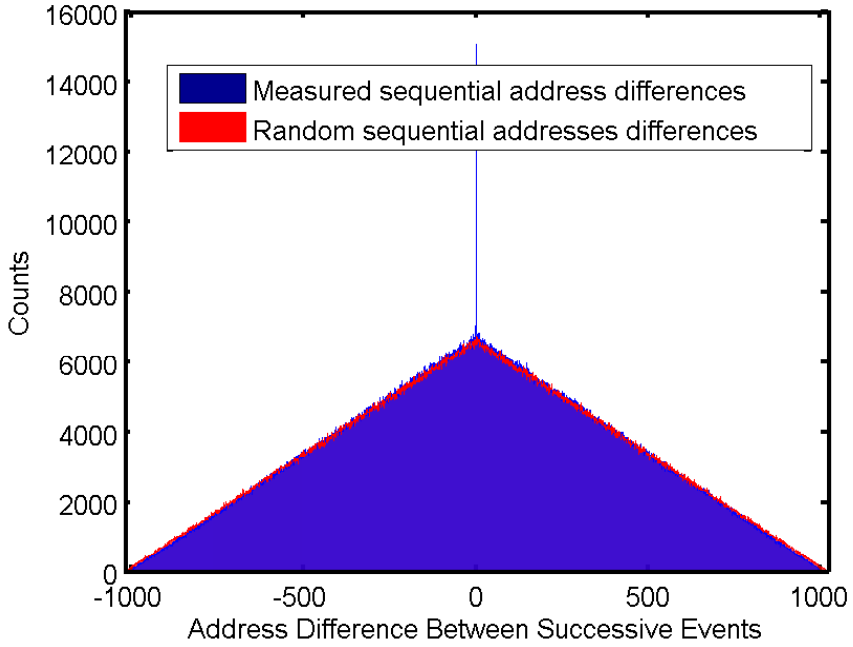

Figure 4.38: Histogram of sequential-event address differences on N-side of detector 20. The histogram of the measured events and randomly-generated events are plotted. The only difference between the two distributions is a spike at 0-channel difference in the measured data, which is from a noisy channel inundating the data stream. Fewer counts are in the high-value bins because of the combinatorics of the problem: it is less likely to have two events with sequential-address difference of 1023 (two possibilities) than it is for a difference of 1022 (four possibilities) and so on.

Table IV.9: Second intrinsic efficiency measurement with detector 20 N-side. The data was acquired on 06/01/2009, the source activity was 0.167 MBq ± 3.1 %, and the geometry was the same as in the first measurement.

Acq. Time (m)	N (photons)	$\Omega/4\pi$	$N_{incident}$	$N_{det.}$	$N_{background}$
208.333	5.084×10^{9}	3.286×10^{-3}	7.26×10^{6}	3.12×10^{6}	5.31×10^{4}

the number of singles minus the number of background counts divided by the number of calculated incident photons:

$$\epsilon_{int} = \frac{3.12 \times 10^6 - 5.31 \times 10^4}{7.26 \times 10^6} = 42.84 \pm 4.62\ \% \tag{4.16}$$

This second measurement with the error is just under the intrinsic efficiency from the simulation.

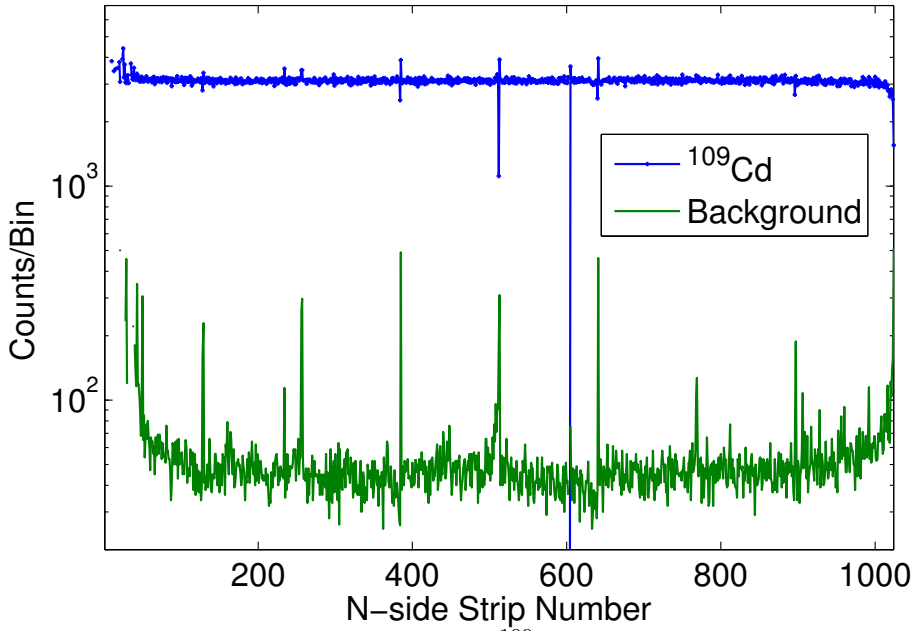

Figure 4.39: N-side singles histogram from ^{109}Cd flood acquisition and background scan. The acquisition time was 208.3 min.

We measured the intrinsic detection efficiency of the N-side of one detector, which still had the best trigger uniformity of the two detector sides. The thresholds were set well below the 22 keV ^{109}Cd x-ray, but not low enough to receive many noise triggers. Gamma-ray interaction positions are determined by combining the data from the two independently-triggered sides, some total efficiency is lost in the sorting process. Since the P-side trigger uniformity was less than the N-side, some N-side events did not

find coincidence pairs. So the coincidence detection efficiency is limited by whichever side has the lowest true (not background or noise) singles rate. Thus, the coincidence efficiency for a DSSD is usually less than the efficiency for an unsegmented silicon crystal. Coincidence efficiency in part depends upon the window with which the list-mode data are combined into coincidence pairs. Determination of an optimal sorting window is given in the next section.

4.6 Coincidence sorting efficiency

Two measurements were made to determine the best coincidence window. In the first experiment, thin pieces of tungsten were placed over the detector so only a narrow slit permitted gamma-rays. Data was acquired from a ^{125}I Oncura Brachyseed. In the second experiment a mask with two 1 cm diameter holes was made in a sheet of molybdenum.

In both experiments, coincidence images were made for a series of different coinicidence window times. Then counts were summed in several regions of interest (ROIs). In the slit image, counts were summed in the slit-projection area, and in a region where there should have been no counts. For the two-holes, ROIs were selected around the hole projections and the regions intersecting the hole-axes, where misplaced coincident events would appear. Example projections created with low- and high-coincidence time windows are shown in fig. 4.40.

Event position information comes from independently-operating detector sides, so if one side is triggering more efficiently than the other, there will be fewer coincidence matches made than if both sides trigger equally. The optimal coincidence window was

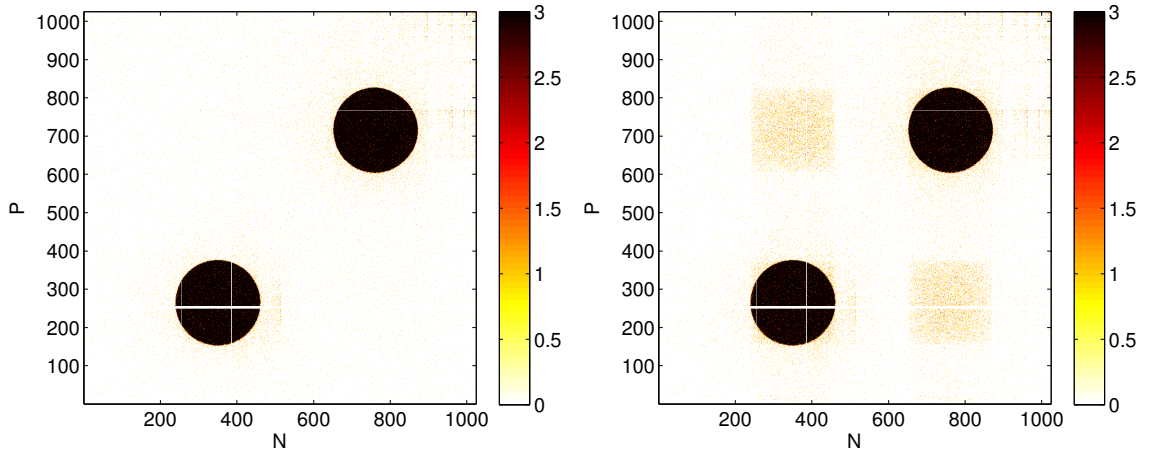

Figure 4.40: Projection images from two-hole mask in a thin molybdenum sheet and a ^{125}I Oncura Brachytherapy seed. Coincidence sorting algorithm used a 2.5 μs window (a) and large, 2.5 ms (b) window. Mis-assigned coincidence events are seen in in the square-shaped regions in (b), which form as the extent of the circles. A very large coincidence (large enough to have rollovers in the time stamps) window is needed to have significant numbers of mispairings, indicating the robustness of the sorting algorithm.

defined as the window that produces the maximum number of overall coincidences and the highest ratio of true to false coincidences. The two-hole data shows an optimal window in the range 50-300 coincidence clock units (1.25-7.50 μs). In fig. 4.41, the ratio of true to false events plateaus near 1.25 μs, which is also near where the number of total coincidences reaches a maximum. The clock runs at 40 MHz, so a single clock unit is 25 ns. Singles events were subsequently sorted with a window of 150 clock units, or 3.75 μs. For two events to be in coincidence, their coincidence clock difference must be less than 150 (no fixed window requirement) and the millisecond time stamp must be the same.

Noise triggers are likely to be discarded in the sorting process. A noise trigger generated on a strip on one side of the detector does not induce a signal on the opposite detector side. For noise triggers to make it into the coincidence image, they

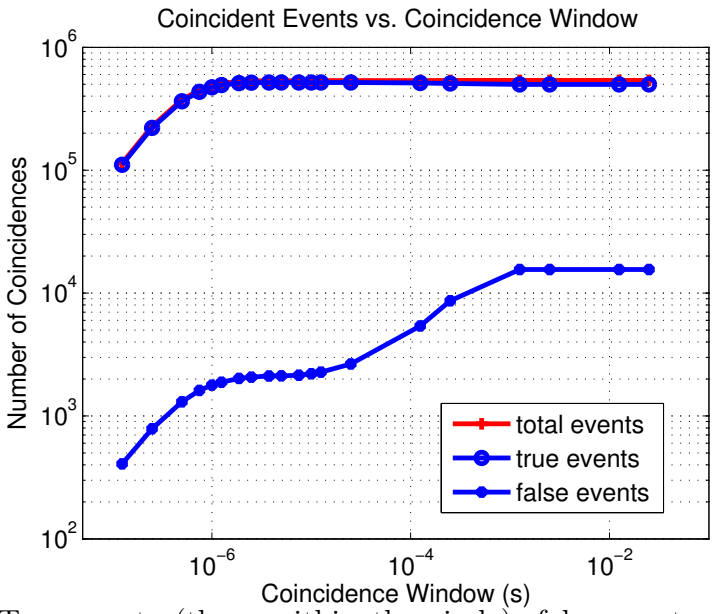

Figure 4.41: True events (those within the circle), false events (those in the mismatched areas), and total coindidence events vs. coincidence window time.

have to be paired with a real trigger from the opposite side that happened to occur within the sorting window. If the thresholds are set low enough on both sides, real photon absorption events (above ∼10 keV) should produce triggers on both DSSD sides, so the time stamp from both events is likely to be closer together than a noise event with a random time stamp. The singles and coincidence ADC histogram for a single channel shown in Fig. 4.42 illustrates this effect. The small peak at the left is due to noise triggers and most of these events are discarded in the sorting process.

4.7 Timing Properties

We already determined an optimal coincidence sorting window in Sec. 4.6. Here we explore several of the other timing properties of the detector system. The timing resolution is found by binning the time difference between coincident P- and N-side

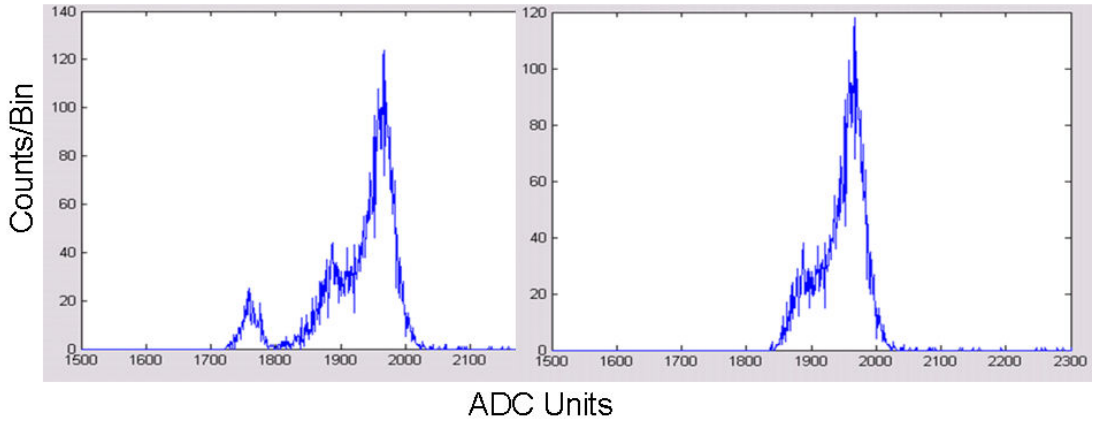

Figure 4.42: P-side channel's ADC spectra before (left) and after (right) coincidence sorting. Counts from electronic noise are present before sorting, but those events are largely discarded because events with corresponding time-stamps do not exist on the N-side.

events. The FWHM of the resulting distribution is a measure of the system timing resolution. We found that the resolution varies with count rate and photon energy.

For a lower count rate, like that experienced during the efficiency measurements with the ^{109}Cd source, the FWHM of the coincidence difference histogram (the timing resolution) was ∼950 ns. Fig. 4.43 shows the timing resolution peak for all strip-pairs and Fig. 4.44 shows the peaks for each chip-pair, with the P-chip value on the y-axis and N-chip value on the x-axis. The contribution to the overall timing resolution is about the same for each area of the detector.

In all cases, the P-side data has slightly larger time stamps, so the timing peaks are shifted to the right for the P minus N time difference calculation. The P-side collects the holes, which drift at roughly one third the rate of electrons in the DSSDs, so their slower drift time could explain the later time stamps. Somewhat countering this effect

is the fact that slightly more photons interact closer to the P-side. The detector is illuminated from the P-side, so more photons interact closer to that side and those holes have shorter drift lengths. The offset from zero is roughly 750 ns. The charge collection time in the DSSDs is an order of magnitude less than this, which indicates that some other process is causing the offset. Similarly, we made measurements of the timing resolution when the detector was biased at 300 and 400 V. There was no obvious difference. Thus, the large timing resolution is likely due to the readout electronics and not the detector charge collection. The offset is likely a discrepancy between the time-walk on the fast-amplifiers of both sides. Time-walk will get more scrutiny in the following sections. The offset is not a problem as long as an adequately wide coincidence window is set.

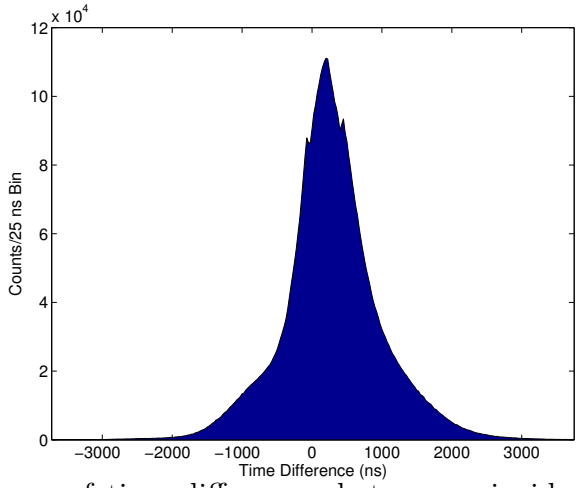

Figure 4.43: Histogram of time differences between coincidence event components from low count rate data. The FWHM of the peak is 750 ns. This data is from the efficiency measurement (Fig. 4.36).

The level-set discriminators contribute to the timing resolution. Fig. 4.45 shows a diagram of the time-walk effect on timing resolution for the low- and high-energy peaks of ^{241}Am. In the diagram, three pulses are shown that come from the fast amp. The first pulse's amplitude is less than the discriminator threshold (Vth) so no trigger

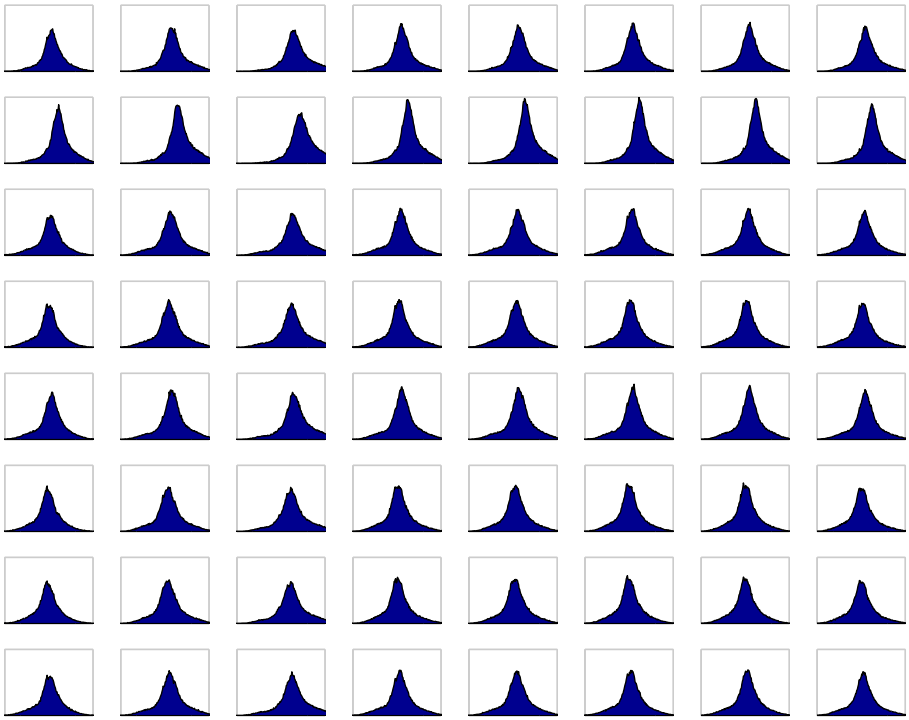

Figure 4.44: Chip-by-chip histograms of time difference data. The origin is in the lower left (P0,N0). The x-axes extend from -3 to 3 μs (just like in Fig. 4.36) and the y-axes are normalized to the maximum counts in the ASIC-pair time difference histograms.

is generated. The second and third pulses trigger the discriminator output when the leading edge of the pulses cross the threshold (Vth). The timing of the output pulse is dependent on the amplitude and the rise time of the input signals. There is "time walk" of the signal trigger with respect to the beginning of the input pulse, so pulses with higher amplitudes produce triggers sooner than those with lower amplitudes.

The events in Fig. 4.45 are histogrammed from a single chip pair (128 x 128 channels) and divided between high and low-energy events. The FWHM of the high-energy timing spectrum is ∼500 ns, but in the low-energy spectrum it is significantly higher, implying that the time-walk differences between the two detector sides are greater for low-energy pulses. The time walk effect propagates to the accuracy of the sample-and-hold readout of the slow-shaper amp. Since the triggers are issued at different times depending on the energy, the readout of the slow amp may be before or after it has fully shaped the pulse, which blurs the overall energy resolution. The energy threshold effects the amount of time walk, and the hold delay can be tailored for the energy of interest. If the threshold is high, then only larger pulses, which cross threshold sooner, cause triggers. If Vth was lowered, the newly-accepted low-energy triggers cross the discriminator threshold later. Meanwhile the slow shaper has had more time to reach its peak, so the hold delay should be less in this case. Hence there is a need for an optimal hold delay based on the energy of interest.

Use of constant-fraction discriminators instead of level-set discriminators would remove the time walk degradation in timing and energy resolution, but they are power hungry and would have placed additional constraints on the design of the ASICs.

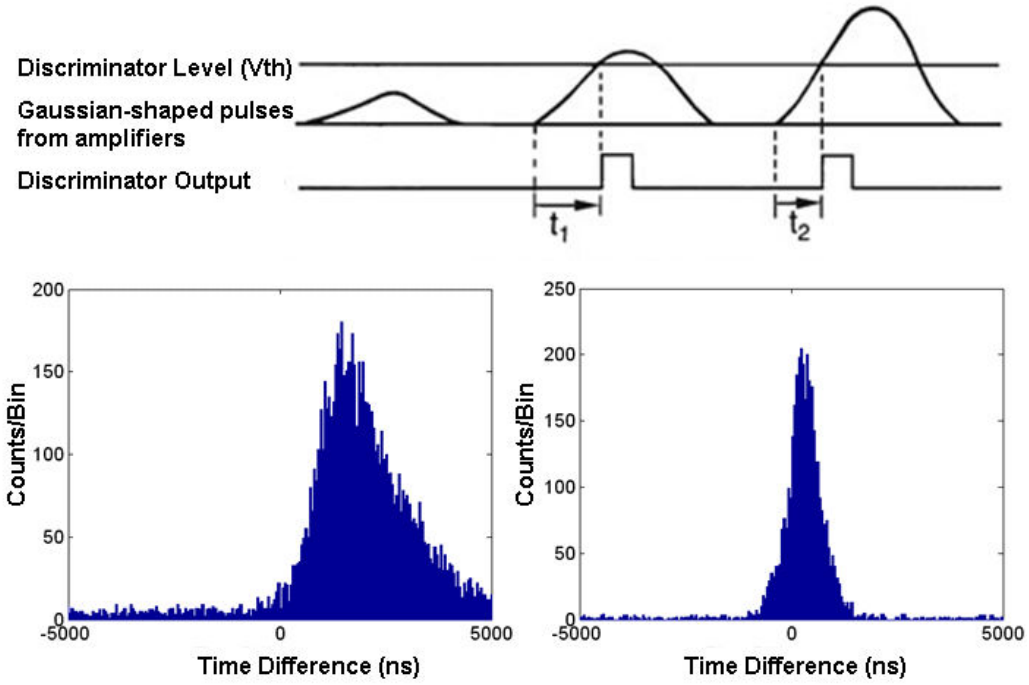

Figure 4.45: Timing resolution for the low-energy (left) and high-energy (right) peaks of ^{241}Am from the events of one DSSD chip pair. The timing resolution is shorter for the high-energy peak due to time walk in the discriminator output, illustrated in the cartoon at the top where the larger pulse crossing Vth sooner than the smaller pulse. The diagram is modified from Ortec literature.

4.7.1 Count rate capability

Count rate capability is an important characteristic of detectors in small-animal SPECT since a lot of activity can be in the field of view. It becomes even more important when high-sensitivity apertures are used, such as coded apertures.

At higher count rates hot strip artifacts appear in the coincidence images. Some strips produce more triggers than their neighbors, inundating the system output and affecting the timing resolution. An example high-count rate flood image from an ^{125}I source is shown in Fig. 4.46. This detector had not been trimmed so the uniformity was poor in addition to the count rate related artifacts. The time-difference between coincidence pairs histogram (Fig. 4.47) is more complicated with this data. The noisy channel events are spaced in a more consistent way than the real events, which adds nodules and spikes to the time-difference histogram. This is seen in Fig. 4.48, where the chips with more noisy triggers have not only more counts but more structure to the histogram shape. The noisy channels create a worse timing resolution with a FWHM of 2000 ns. The time stamps are generated after the triggers and ADC values have been read out and sent to the CROB. The time between trigger and time stamp likely adds to the width of the timing resolution. The hot strip artifacts could show up in the higher channels because of the readout order of the channels (from high to low). If during a readout cycle only a certain number of triggers are readout, at high count rates that means that some low-channel triggers will not be read.

For SPECT applications, the timing resolution is not of critical importance since the counting rates are typically much lower. Reducing or filtering the noisy channels

at higher counting rates is important for trigger uniformity and correctly assigning coincidence pairs.

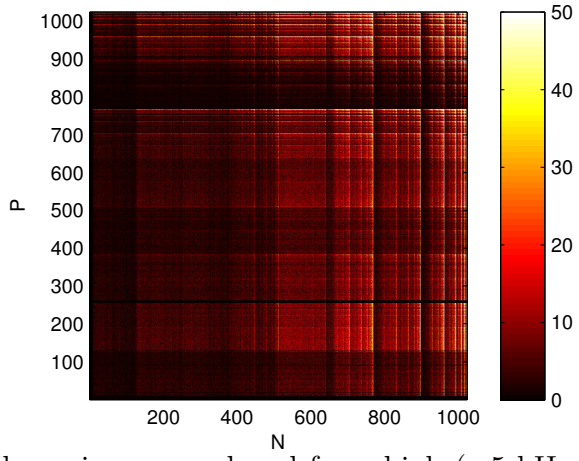

Figure 4.46: Coincidence image produced from high (>5 kHz/side) countrates. Hot strip artifacts show up in the higher channels likely due to a clocking readout order from high to low strip numbers.

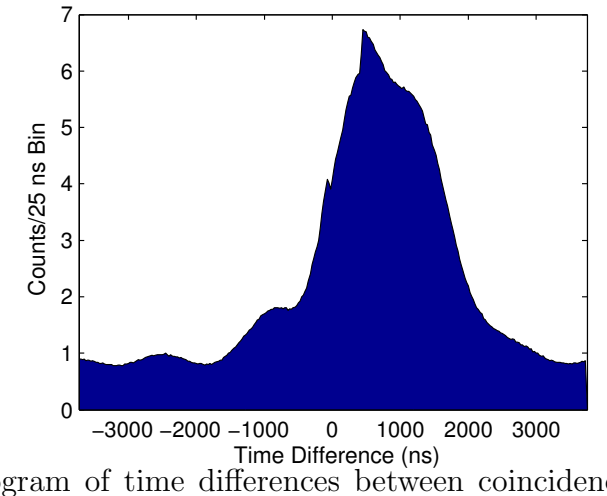

Figure 4.47: Histogram of time differences between coincidence event components from low count rate data. The FWHM of the curve is 2000 ns.

4.7.2 Dead time measurement

In almost all detector systems there is a minimum time that must expire between two events for them to be recorded as two pulses [107]. This 'dead time' can arise from processes in the detector or in the readout electronics. Since radioactive decay

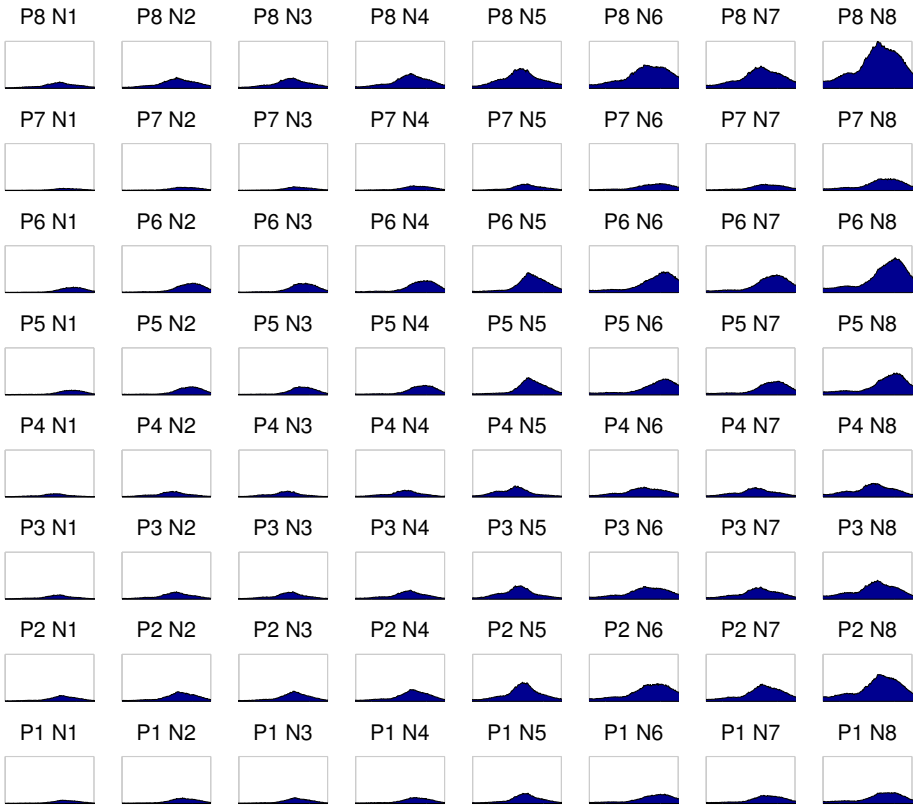

Figure 4.48: Chip-by-chip histograms of high count rate (> 5 kHz) time difference data. The origin is in the lower left (P0,N0). The upper right chips have the most signal and the most hot strip artifacts. The x-axes extend from -3 to 3 μs and the y-axes are normalized to the maximum counts in the ASIC-pair time difference histograms.

is a random process, there is always a chance that some events will be lost to dead time, but dead time losses can become quite high with greater counting rates. In SPECT the counting rates never get too high because the collimator attenuates the vast majority of emitted photons. However, with large amounts of activity in a small FOV with multi-pinhole apertures, there is a possibility that significant losses could occur. Thus, we used a standard technique to measure the system dead time and characterize the system response.

Most detector systems can be described by either a paralyzable or non-paralyzable model for dead time. As the name implies, a paralyzable system's observed counting rate decreases as the actual counting rate increases, effectively choking on the data. In the nonparalyzable system, true events that occur during the dead period are lost, but have no affect on the operation of the detector.

For a nonparalyzable detector, the fraction of all time that the detector is dead is the product mτ, where m is the recorded count rate and τ is the system dead time [107]. The rate at which true events are lost to dead time is nmτ, where n is the true counting rate (with no losses from dead time). The difference (n-m) is another expression for the loss rate of true events, so:

$$n - m = nm\tau. \tag{4.17}$$

Solving for n yields:

$$n = \frac{m}{1 - m\tau}. \tag{4.18}$$

The paralyzable model is given by Knoll as:

$$m = ne^{-n\tau}. \tag{4.19}$$

With a hold delay of 75 clock units (1.875 μs), the minimum time between events (dead time) is 10.3 μs. according to Eq. 4.18, the percentage of events lost because of the dead time is less than 1 % for rates up to 5.5 kHz, which is greater than the maximum rate we expect to encounter in SPECT imaging. If the hold delay is made nearly zero, the system dead time remains at around 8.7 μs, so there are some other timing bottlenecks in the readout system.

Even though the dead time can be directly measured by looking at the minimum sequential-event time difference in the list-mode data, we can determine which dead time model describes our system and see if there are any major count rate related effects (such as retriggering due to clocking on the readout lines). We measured the dead time with the decaying source method [107]. This method is based on the way the observed count rate departs from the known exponential decay of the source. The true count rate, n, is given by:

$$n = n_0 e^{-\lambda t} + n_b, \tag{4.20}$$

where n_0 is the true rate at the beginning of the experiment, λ is the decay constant of the isotope used, and n_b is the background counting rate. We used ^{99m}Tc, as it was readily available, has a $\sim$6 hr half-life ($\lambda = 0.116$ hr^{-1}), and a moderate amount

of 18 keV x-rays. The main gammma-ray emission at 140.5 keV mostly scatters in the detector, but still contributes to the counting rate. If the background rates are less than a few percent of the smallest measured rate, then the n_b term disappears and Eq. 4.20 can be plugged into Eq. 4.18 to become:

$$me^{\lambda t} = -n_0 \tau m + n_0. \tag{4.21}$$

If $me^{\lambda t}$ is the ordinate and m is the abscissa, a line can be fit for different observed counting rates over time to extract the intercept (original true counting rate) and the slope divided by the intercept (the dead time). For the paralyzable model, Eq. 4.20 is inserted into Eq. 4.19, which yields:

$$\lambda t + \ln m = -n_0 \tau e^{-\lambda t} + \ln n_0. \tag{4.22}$$

Like before, the dead time and original true counting rate can be extracted by fitting the data to get the slope and intercept. Both models give similar results for low rates ($n \ll 1/\tau$), so it is important that the initial rate be high enough to have at least a 20 % loss fraction ($m\tau$). With a ~1 mCi ^{99m}Tc source in a small eppendorf tube, the highest count rate was around 16 kHz. The hold delay time was set higher at the time of measurement to 5 μs (possibly in error, since the slow shaper has a peaking time of 3 μs), so the dead time was around 13.4 μs, making the loss fraction 21.5 % for the first measurement. Thus, the first few measurements will have the largest difference between the model fits.

The source was placed 30 cm from the detector, ensuring reasonably accurate flood geometry. Data was acquired for 10 min with 30 min wait periods between acquisitions. A total of 36 acquisitions were made spanning 24 hr, or about four half-lives of the isotope. The number of N-side counts during each acquisition was summed to give the m values. Fig. 4.49 shows the data and a best-fit line for the nonparalyzable model. The data best fit the nonparalyzable model, suggesting that we can collect data at higher count rates without worry of locking up the system.

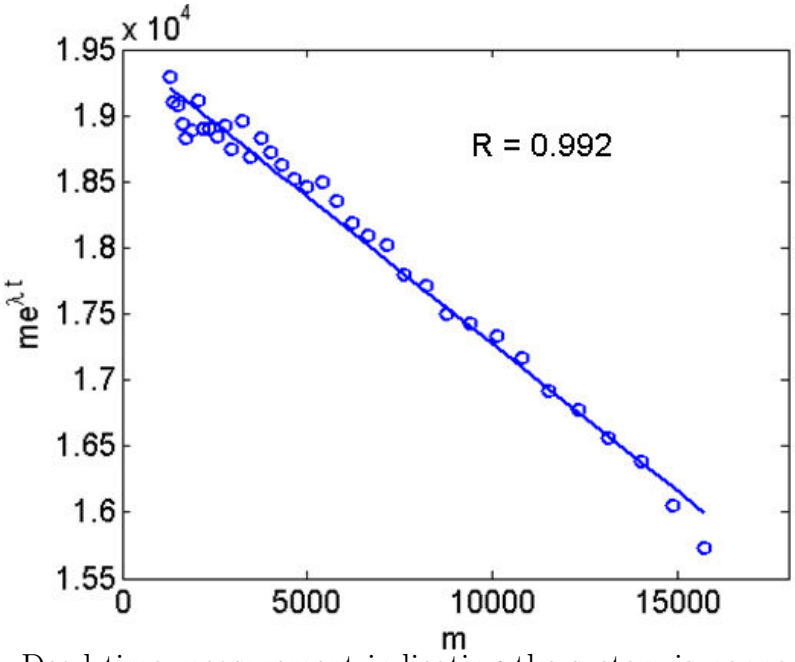

Figure 4.49: Dead time measurement indicating the system is nonparalyzable. The slope divided by the intercept gave a dead time of 14 μs.

4.8 Energy resolution

Energy resolution is a measure of the dispersion in the number of information carriers for a given energy (ΔE/E). Good energy resolution is important for distinguishing between full-energy events and scattered events, where a photon loses part of its energy by scattering off an electron (Compton scattering) or an atom (Rayleigh

scattering). Scattered events generally degrade the image quality, since position information is lost in the scatter, which the reconstruction algorithm then uses incorrectly.

The energy of a Compton-scattered photon is:

$$E_{sc} = E_0/[1 + (E_0/0.511)(1 - \cos\theta)], \tag{4.23}$$

where E_0 is the initial photon energy in MeV and θ is the scattering angle. The minimum energy of scattered photons (most energy given to the electron) occurs when the photon is backscattered ($\theta = 180°$):

$$E_{sc}^{min} = E_0/[1 + (2E_0/0.511)]. \tag{4.24}$$

The maximum energy transfered to the recoil electron, E_{re}^{max}, which is equivalent to the maximum energy deposited in the detector in a single scatter) event, is simply:

$$E_{re}^{max} = E_0 - E_{sc}^{min}. \tag{4.25}$$

Distinguishing between a Compton-scattered and photoelectric events requires a detector with very high energy resolution in low-energy (<50 keV) imaging. Table IV.10 compares the energies of the backscattered scattered photon and electron for ^{125}I and ^{99m}Tc. To distinguish the scattered ^{125}I photons would require a detector with energy resolution less than a few keV, whereas for ^{99m}Tc a detector with resolution greater than 20 % of the peak (28 keV FWHM) would suffice. The energy resolution of the DSSDs is on the order of 5 keV at best (Fig. 4.50). Thus, most

Table IV.10: Backscattered photon and recoil electron energies for ^{125}I and ^{99m}Tc.

Radionucilde	E_0 (keV)	E_{sc}^{min} (keV)	E_{re}^{max} (keV)	E_{re}^{max}/E_0 (%)
^{125}I	27.3	24.7	2.64	10.7
^{99m}Tc	140.5	90.7	49.9	55.0

scattered photons can not be rejected. The resolution offered by a HPGE detector may be the only way to accurately reject ^{125}I scatter events.

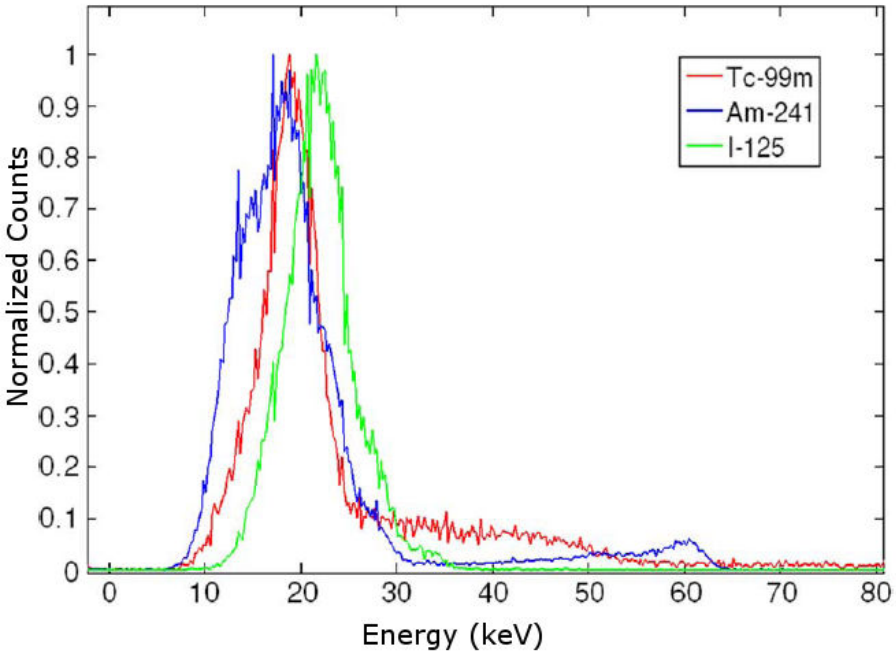

Figure 4.50: Energy spectra from three ^{99m}Tc, ^{125}I, and ^{241}Am in a single P channel. The FWHM of the 18 keV peak from ^{99m}Tc is 5.2 keV. The 60 keV peak from ^{241}Am is visible and was one of the calibration peaks. ^{241}Am has the widest low-energy peak because it is composed of several x-rays at 14 and 18 keV. A Compton edge from scattered ^{99m}Tc is near 45 keV.

To assess the energy resolution across the channels on each detector side, two flood acquisitions were made, one with ^{125}I and another with ^{241}Am. For each channel, the ADC histogram was smoothed and the peak found. The peaks from ^{241}Am were from the 14-18 keV x-rays; most of the 60 keV gamma rays are not detected in the DSSDs. So the peaks from the two isotopes are separated by 10-13 keV. The ADC

peak positions versus the 2048 detector channels are plotted in Fig. 4.51. The peaks are resolved for all of the N-side channels, which show both gain and offset variations. The width of the peak separation indicates the gain of the amplifiers and the relative position on the ADC scale shows the offset. The P-side has more gain and offset variation than the N-side; three of the eight chips appear to have very low gain. The precise causes of the P-side ADC nonuniformity remain a unknown. The P-side collects the holes, which travel slower and thus have longer integration time. This could make the readout more susceptible to noise and increase the time-walk effect.

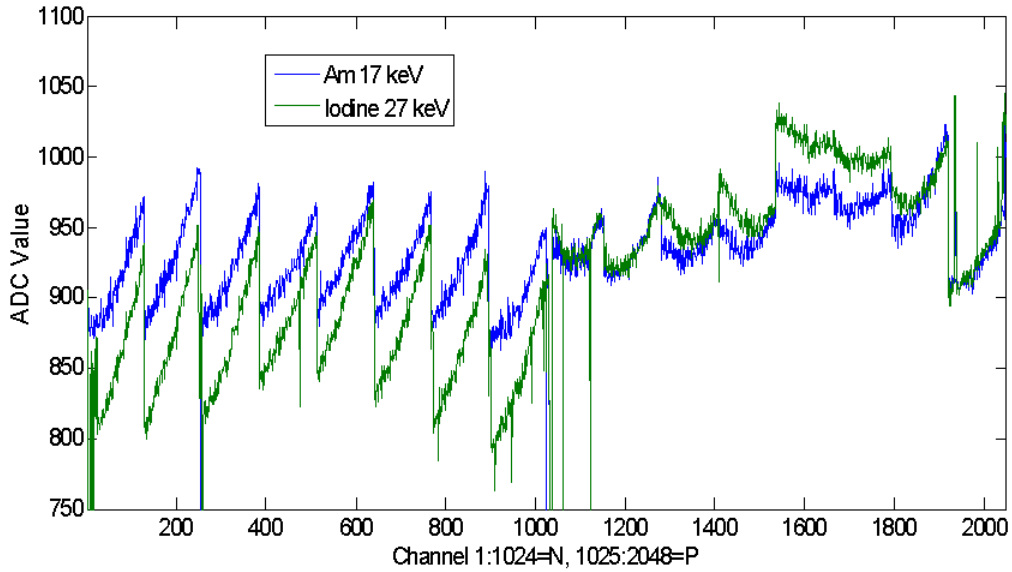

Figure 4.51: ADC peaks from ^{125}I and ^{241}Am for all detector 18 channels. Channels 1-1024 are for the N-side (lower ADC equals higher energy) and channels 1025 to 2048 are the P-side. The peaks were ~27.3 keV for ^{125}I and 60 keV for ^{241}Am. Good peak separation is seen on the N-side, but three P-side chips have low gain, and thus poor energy resolution. The N-side collects electrons and the P-side collects holes, so the polarity of the induced charges are opposite. Thus, the low-ADC values on the N-side correspond to higher energy.

The N-side ADC histograms have the characteristic wave-shape on all the DSSDs. Each DSSD P-side is non-uniform and different from the other DSSDs. For example, the N-side spectra on detector 19 (from ^{241}Am) look quite similar to those of detector

18, and the P-side spectra vary wildly (Fig. 4.52). Only the last chip on P19 has low gain. If we make an energy calibration on just the N-side and use it to make ADC cuts, many of the corresponding P-side triggers would not find a coincidence pair, and so would be effectively discarded. This would only be helpful in removing photon interaction events of a certain energy (high-energy removal, perhaps), and not noise triggers, since they are generated independently on both sides.

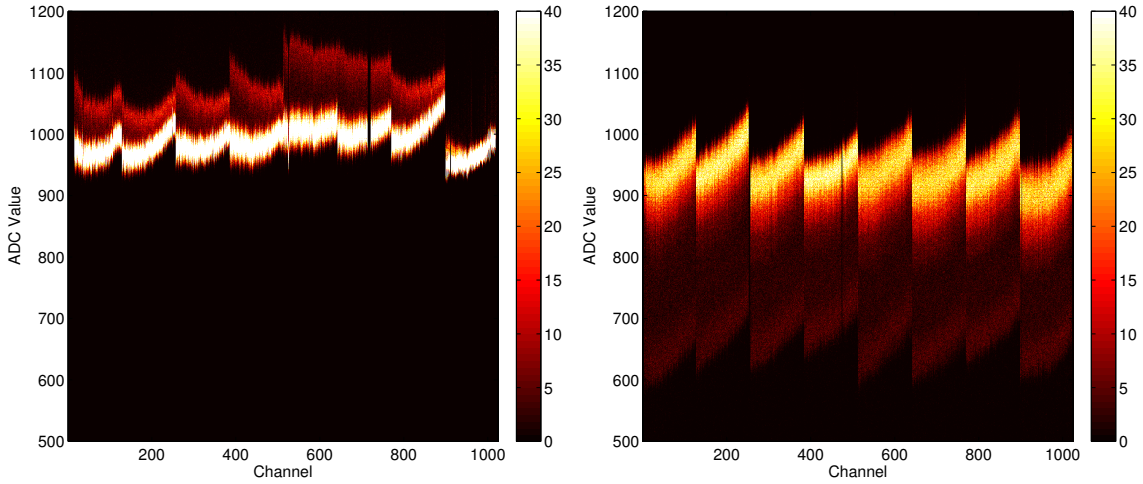

Figure 4.52: Energy spectra from ^{241}Am on all detector 19 P-side (left) and N-side (right) channels. The N-side chips show similar gain and offset variations, whereas the P-side chips have great variability. Overall, the N-side chips have roughly three times the gain of the P-side chips. The last P-side chip has very low gain.

An energy calibration would be useful in rejecting some noise triggers, some of which are well below ^{125}I photopeak. An energy calibration would also allow some other types of noisy data to be removed before they enter the coincidence sorting algorithm. For instance, the count-rate-related noise events have high-energy ADC values that can be removed as described in Sec. 4.3.5. With a good calibration, a more accurate ADC cut could be applied to each channel so fewer real events would be discarded.

4.8.1 Charge sharing

Small pixels are desired for increased spatial resolution, but as the pixels get smaller the likelihood that a signal produced by a photon interaction is shared among several electrodes increases. Charge sharing can degrade energy resolution and decrease detector efficiency, depending on the energy of the photon. These losses can be averted if nearest-neighbor pulse-height information is available, or with the proper setting of triggering thresholds. The DSSDs have an aspect ratio (material thickness divided by pixel width) of ∼16.9. Electrons and holes produced in the detector follow the field lines to the electrodes, but there are several mechanisms that cause the charge clouds to spread over time.

The expected amount of charge-sharing can be estimated by considering the size of the initial electron/hole cloud, the drift time of the cloud, and the diffusion of the cloud over the drift time. Self-repulsion also adds to the lateral spread of the charge-carriers. Trapping of charge carriers also enhances charge-spreading among the detector pixels, however this is more significant in materials such as CZT than in silicon.

The detector bias is 300 V, so the average electric field magnitude in the DSSD is:

$$E = \frac{V}{w} = \frac{300V}{0.1\ cm} = 3 \times 10^3 V/cm, \tag{4.26}$$

where w is the detector thickness. In silicon the electron mobility, μ, is 1350 cm^2/Vs and the hole mobility is 450 cm^2/Vs at 300 K. The drift velocity of the charge carriers, at low-to-moderate electric field intensities, is the product of the mobility and the

magnitude of the electric field:

$$v_d = \mu_E E. \tag{4.27}$$

At higher fields the drift velocity becomes saturated. The electric fields are low enough in the DSSDs so the simple relation still applies. For the DSSDs, the drift velocities are 4.0e$\times 10^6$ cm/s and 1.44$\times 10^6$ cm/s for electrons and holes, respectively at 300° K[107]. The electrons and holes immediately separate upon their creation because of the electric field. Both the electrons and holes take part in random thermal motion which causes them to diffuse apart over time. The width of the distribution can be approximated by a Gaussian function with a standard deviation of:

$$\sigma = \sqrt{2Dt} = \sqrt{\frac{2Dw}{v_d}} = \sqrt{\frac{2Dw}{\mu_E E}}. \tag{4.28}$$

where D is the diffusion coefficient and t is the drift time, which is the drift distance (detector thickness), w, divided by the drift velocity. The diffusion coefficient is given by the Einstein relation:

$$D = \frac{\mu_E kT}{e}, \tag{4.29}$$

where k is Boltzmann's constant, T is the temperature, and e is the electron charge. Combining Eqs. 4.29 & 4.28 yields:

$$\sigma = \sqrt{\frac{2wkT}{eE}}. \tag{4.30}$$

The diffusion width (σ) is independent of the material and is the same for holes and electrons. The value of kT at room temperature is 0.0253 eV. For the detector thickness, (maximum diffusion amount after the drift), and electric field at room temperature, Eq. 4.30 yields a sigma of 9.18 μm. We definitely expect to see some charge-shared events, since the size of the charge-cloud (and distribution of induced signals) will be larger than this since self-repulsion was not considered. Fig. 4.53 shows the charge-sharing between two strips from ^{241}Am events. The low-neighbors generally have signal on them while the high-neighbors do not. This is due to the high-to-low triggered-channel readout order. If an event is shared between two strips so that they both trigger, the highest trigger channel will be read out first. This channel itself does not have any high-neighbor charge-sharing (above threshold), since if it did *that* channel would have been read out first. The low-neighbor of the readout channel also has signal on it, which is recorded. Reading out the lower-channel trigger as a low-neighbor of the higher-channel trigger effectively removes it from the output. Only the higher of the two trigger channels gets read out, and only the low-neighbor will have any charge on it. This is still a valid way to assess the charge sharing among strips as long as the majority of the charge is distributed between two strips.

4.9 Spatial resolution

A qualitative way to demonstrate the detector resolution is with a shadow mask placed over the detector. A steel gear was set on a sheet of plastic over the detector face and illuminated with an Oncoseed source. The fine teeth of the gear are sharply resolved (Fig. 4.54).

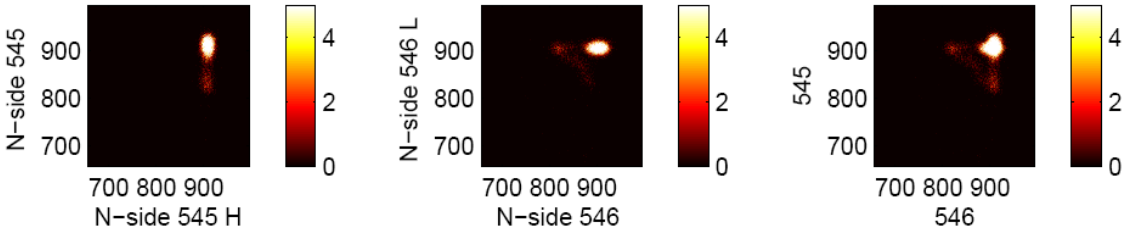

Figure 4.53: Pulse-height correlation for three N-side strips from ^{241}Am events. When channel 545 is the trigger channel, the high-neighbor channel always has very little charge on it (left), but when channel 546 is the trigger channel, the low-neighbor does have charge on it most of the time (middle). The right plot is the sum of the first two plots and shows the total charge sharing between 545 and 546. Charge is only seen on the low-neighbors because of the readout order from high- to low-channels, so the high-channels have already been read out as main triggers before they have a chance to be read out as high-neighbors.

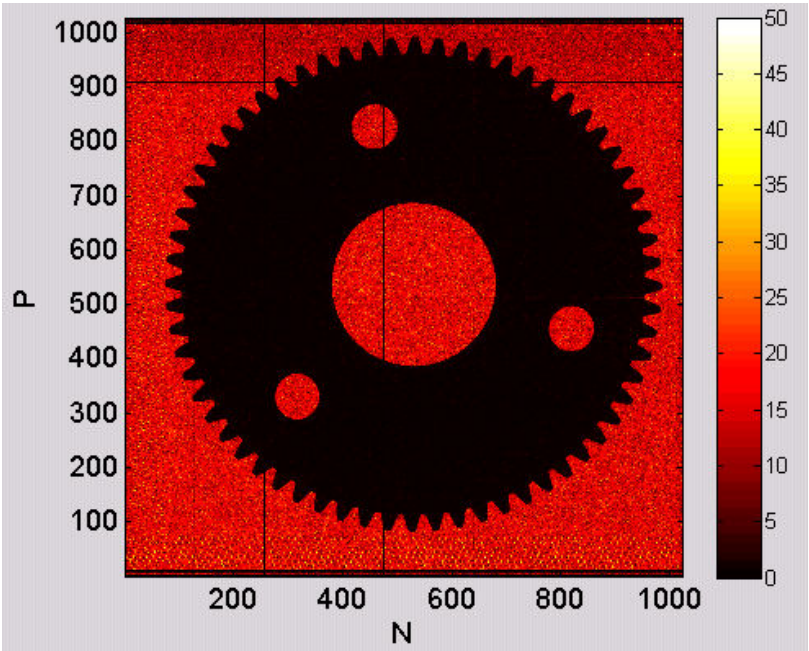

Figure 4.54: Shadow image with a gear and ^{125}I Oncoseed source flood geometry. The DSSD was covered with a 1 mm plastic sheet and the gear was placed directly on the plastic.

The spatial resolution was measured by Dr. Shokouhi with a line-pair phantom used in x-ray radiography. The shadow image of the line pair phantom is shown in Fig. 4.55. The intrinsic detector spatial resolution was demonstrated to be equivalent to the strip pitch, 59 microns [111] The inset shows a line profile through the strips at 9 line-pairs per mm.

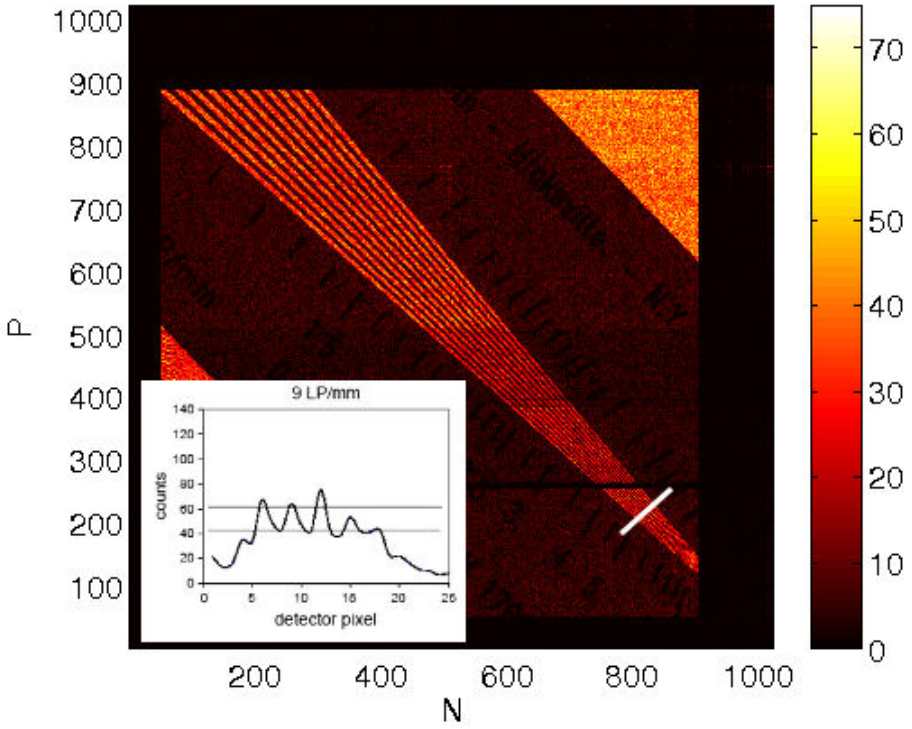

Figure 4.55: Shadow image of a line-pair phantom laid on DSSD and irradiated with ^{125}I Oncoseed source flood geometry.

CHAPTER V

CAMERA HEAD MEASUREMENTS

5.1 Camera head specifications and assembly

The design of the of the camera head boxes revolved around permitting the detectors to move with respect to each other and the aperture plate. We wanted the ability to adjust the magnification without opening the box in order to investigate synthetic collimator imaging under different conditions. This constraint made the boxes larger than they might be otherwise. The detectors are mounted on micrometer-adjustable rails within the camera box. The distance between the detectors and the distances from the detectors to the aperture can be changed without opening the box. A micrometer head on the back of the box presses against a metal frame that is attached to a rail slider, which in turn is screwed to the detector frame. A photograph showing the detector mounted to a holding frame and the slider is shown in Fig. 5.1. A metal rod attached to the front of the box slides through an opening on the metal frame and is held in place by a washer and a spring. The spring constant is large enough to suspend the detector-frame-rail aggregate when opposing the force due to gravity, allowing the camera head to be positioned in a vertical orientation.

The aluminum components on the boxes were anodized, which gave the system a professional aesthetic, but required some filing to electrically ground the plates together to provide electromagnetic shielding. Ground wires from the detectors are secured to the sliders, which are pinned to the bottom plates of the box. From the

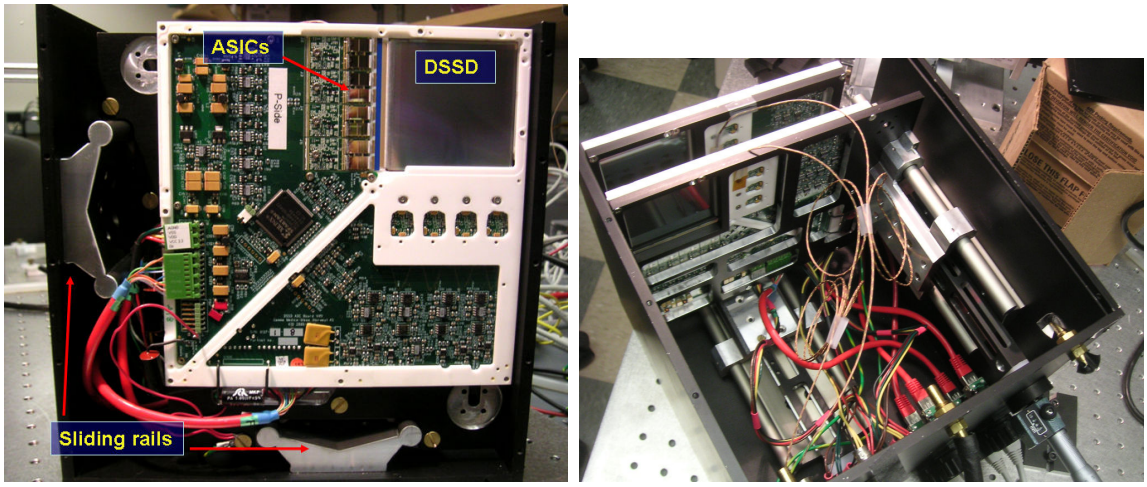

Figure 5.1: Photograph of a silicon DSSD board in an open camera head with labels showing the ASICs, detector, and mounting plate attached to adjustable rails (left). View of the open box from behind and above the apertures, with micrometer head visible in the lower right corner (right).

back of the box a ground wire runs to the power supply.

To run the full system, several changes were needed from the test box setup. A single power supply can power up to four DSSDs, but we found that the detectors operated more stably when two power supplies were used (one for each camera head). This necessitated the use of two digital isolator boards as well. A single CROB was used. The system is depicted as a cartoon in Fig. 5.2 and in reality in Fig. 5.3.

Three line-emitting lasers were arranged to shine across the center of the FOV. The laser lines cross the central pinholes of both aperture plates (two lines on both heads). These lines help position the object to be imaged to within a few millimeters.

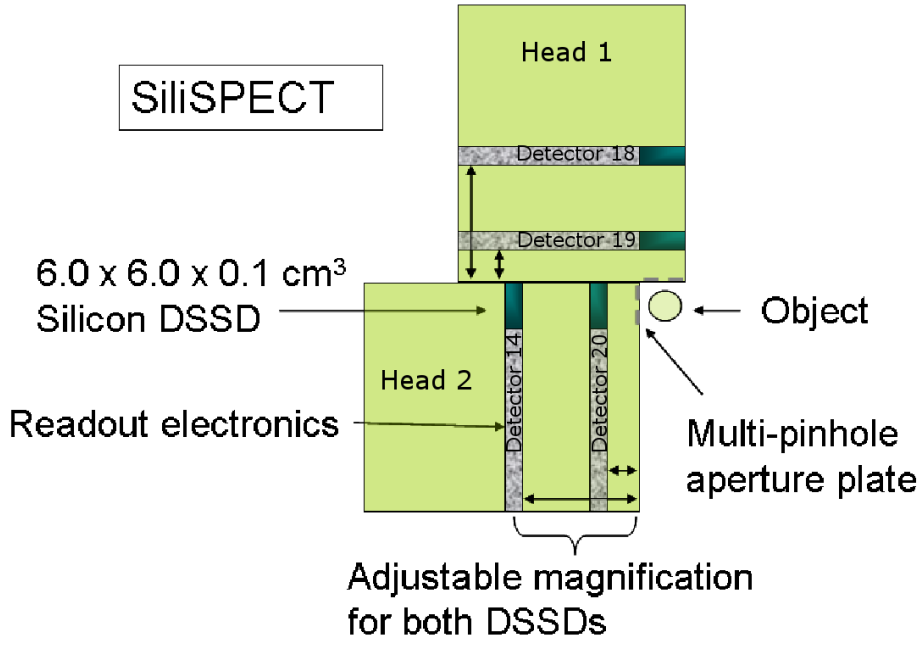

Figure 5.2: Cartoon of SiliSPECT. The system consists of two heads, each containing two variable-magnification DSSDs. The stationary system collects projections with multi-pinhole apertures which see a small FOV.

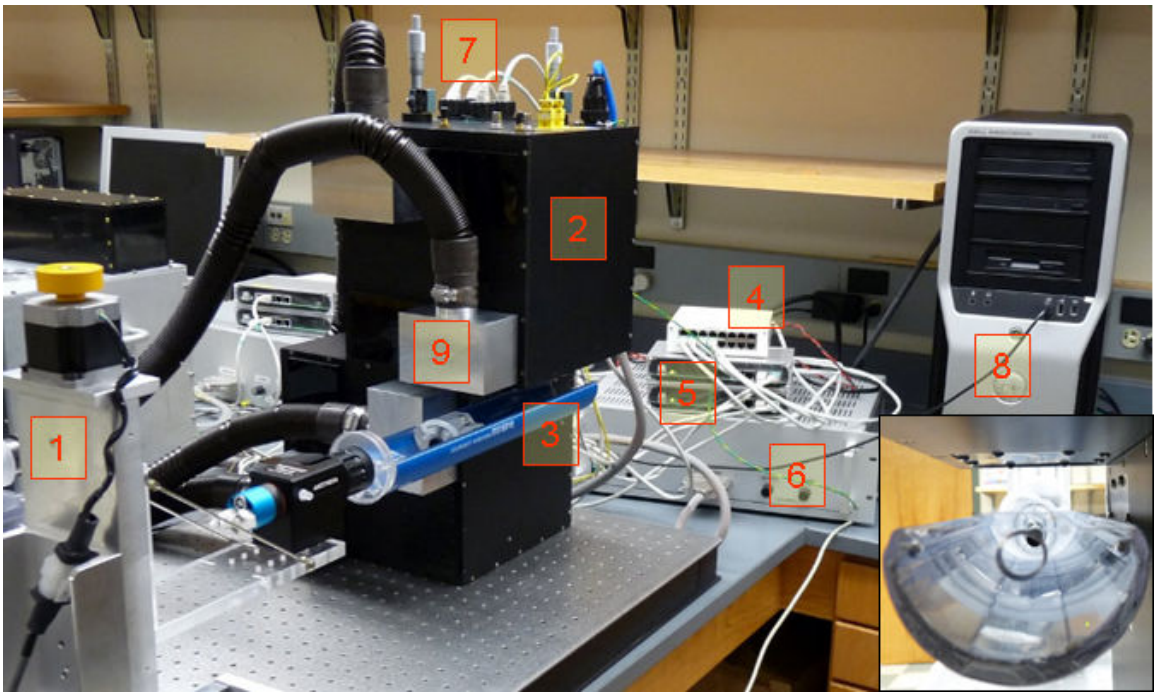

Figure 5.3: Photograph of the SiliSPECT system. 1) XYZ Stages, 2) Camera Head, 3) Bioscan Minerve rat bed, 4) CROB, 5) Digital Isolators, 6) Power supply, 7) Micrometer heads for detector-aperture distance adjustment, 8) NI card and Labview interface, 9) Inlet for forced-air cooling. The inset photograph shows an axial view of the bed with both apertures visible.

5.2 Effects of operating detectors in close proximity

Almost all the detectors had custom-made trim masks when they were being tested. Operating two detectors in one box required changing some of the DACs, which in turn affected the overall trigger uniformity. The largest difference of operating two detectors close to each other is the temperature increase. With twice the amount of heat to dissipate as in the test box (and smaller air volume), the higher temperature affected the gains and offsets of many of the electrical components. The higher temperature likely also led to greater leakage current, and thus more noise triggers and worse trigger uniformity.

Besides heat, the detector readout systems generate a lot of fast digital signals with the clocking. These pulses can cause electromagnetic interference (EMI) in some components. Board-generated sources of noise are coupled to external EMI sources. Though the plates are grounded together, the box is not a true Faraday cage because of the aperture opening and the connectors on the back. It is possible that the detector energy resolution and low-threshold trigger uniformity would be improved if the detector shielding was made better by reducing cross-talk between detectors and pickup from external sources.

The main differences in terms of DACs for the DSSDs in the new boxes were greater Sbif and Vfp values. These both increase the gain, on the fast amp and preamp, respectively. It is not clear why an increased gain would be necessary to obtain better trigger uniformity, but it is consistent across the detector sides in both boxes.

5.3 Multi-pinhole apertures

The parameter space for multi-pinhole aperture design is very large. Optimizing parameters such as pinhole location, size, and orientation is a complex, task-dependent endeavor. Our goal of imaging a small field of view somewhat narrowed the range of possibilities. Pinhole apertures were made that provide high sensitivity, high spatial resolution imaging in a small FOV. Details on the design rationale and pinhole sensitivity characterizations are given by Shokouhi et al. in [112, 113].

127 Cylindrical, 250 μm diameter holes were laser-drilled in 250 μm sheets of tungsten. The pinholes were arrayed in concentric, hexagonal rings with 2.5 mm spacing. The apertures were designed so that the pinholes tilted toward a focus 3 cm from the central pinhole aperture. The central pinhole is untilted, and the outer-most ring of pinholes tilt the most at 26.6°. This was done to increase the sensitivity at the center of the field of view and decrease the sensitivity to out of field of view activity. The pinhole locations were also rotated with respect to the detector to minimize the effect of dead strips on the projection images. Fig. 5.4 depicts the design of the aperture plates and a photograph of the installed apertures.

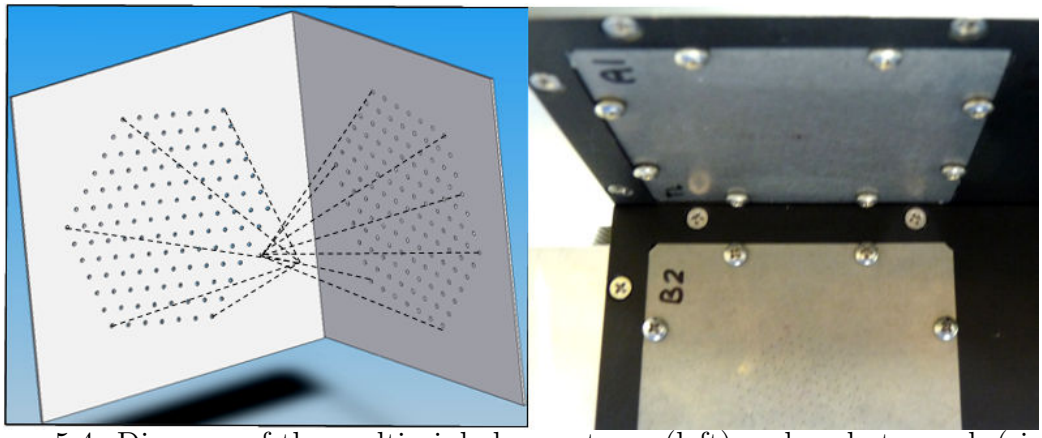

Figure 5.4: Diagram of the multi-pinhole apertures (left) and a photograph (right).

Laser-drilling the holes was significantly less expensive than electron discharge machining (EDM) or tomo-lithographic molding, but was probably less precise than the other techniques. Fig. 5.5 contains two electron micrographs of edge pinholes on the aperture plate. Some debris is seen around the pinhole rims, and some material was left by the laser in the left pinhole micrograph.

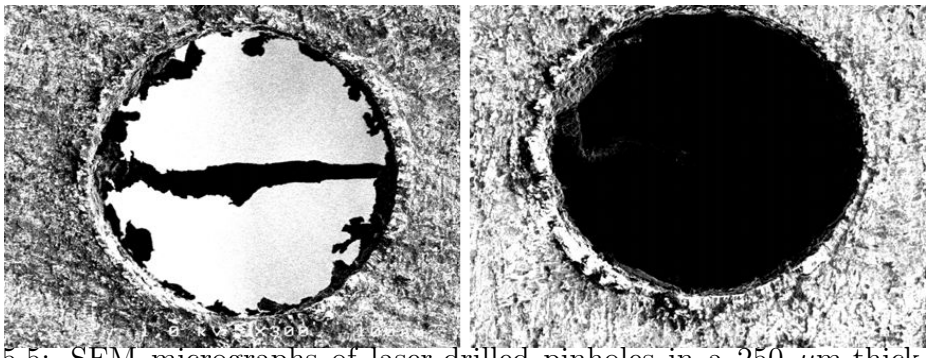

Figure 5.5: SEM micrographs of laser-drilled pinholes in a 250 μm-thick tungsten sheet. Leftover material occludes some pinholes (left), and the edges of the pinholes are fairly rough (both). The pinholes were supposed to be tilted toward a focal spot 3 cm from the central aperture, but no evidence of tilting was seen here.

Multi-pinhole apertures are a key component of the synthetic collimator method since they provide the angular sampling that enables limited-angle tomography. To show the amount of angular sampling provided, the projection images from many rotation angles of the custom seed were summed in a single image (Fig. 5.6). The seed was placed near the axis of the central pinhole and the source rotation radius was $\sim$5 mm. Projections through the outer pinholes traced ellipses with a wider axis in one dimension than those of the pinholes closer to the seed because they viewed the seed at larger angles.

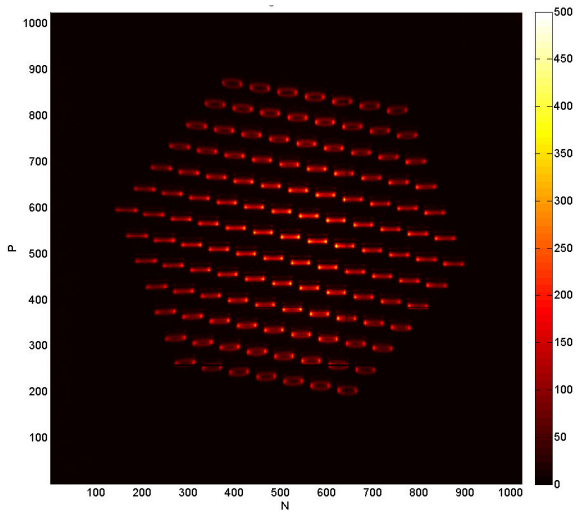

Figure 5.6: Summed projection images of the custom seed for all rotation angles on a front detector (head 2). The outer pinholes trace out ellipses because they view the seed at greater angles, illustrating the angular sampling of the multi-pinhole aperture.

5.3.1 Verifying aperture specifications

To ensure proper modeling of the pinholes in reconstruction, we needed to verify that the apertures were made to specification. It was difficult to visually determine which side of the aperture plate was the focusing side. We examined the apertures with both light and a scanning electron microscopes (SEM), but the tilting of the pinholes was not evident even under high magnification (e.g., Fig. 5.6). Since the holes were laser-drilled, we looked for material debris on the laser-exit side, but this was not consistent across holes. With the failure of visual inspection to determine if the apertures were tilted, we next considered source measurements.

We acquired data with an Oncoseed source positioned over the center pinhole with the aperture on one way, flipped the aperture, and repeated the measurement. We also measured data for both sides when the source was 20 mm off-axis. In both positions the source-aperture distance was 20 mm. The total counts in the projection

Table V.1: Total measured counts for the flipped-aperture configurations shown in Fig. 5.7. The source was either directly in front of the central aperture or 20 mm off-pinhole axis. The source was 20 mm from the aperture plate in all cases.

Source position	A Counts	B Counts	Percent Difference
On-axis	4.30×10^5	4.39×10^5	1.99 %
Off-axis	2.93×10^5	2.86×10^5	2.33 %

image and the individual pinhole projections counts were found. To find the counts in each pinhole projection, the projection centroids were found, then a square region around the centroids was summed. To visually assess the sensitivity maps for the four cases, the projection centroid pixel was replaced with the pinhole projection sensitivity value and downsampled (Fig. 5.7). The numbers for the total counts for the four configurations are given in Table V.1. The total counts for the two aperture sides are only different by a few percent, and these differences most likely come from the different amount of loss in the projections due to dead strips. A smaller source of error is the counting statistics (< 1 %).

To make some sense of the measured sensitivity on both sides, we made a simple simulation based on the ideal pinhole model. The ideal pinhole sensitivity model has known limitations (perfect knife-edge, no keel-length, no penetration, and no finite cone angle), but provides a reasonable first-order estimate for determining whether the apertures are truly tilted [114]:

$$G_{ideal} = \frac{D^2 \cos^3\theta}{16h^2} = \frac{D^2 \cos\theta}{16d^2}, \tag{5.1}$$

where D is the pinhole diameter, d is the source-to-pinhole distance, θ is the incident

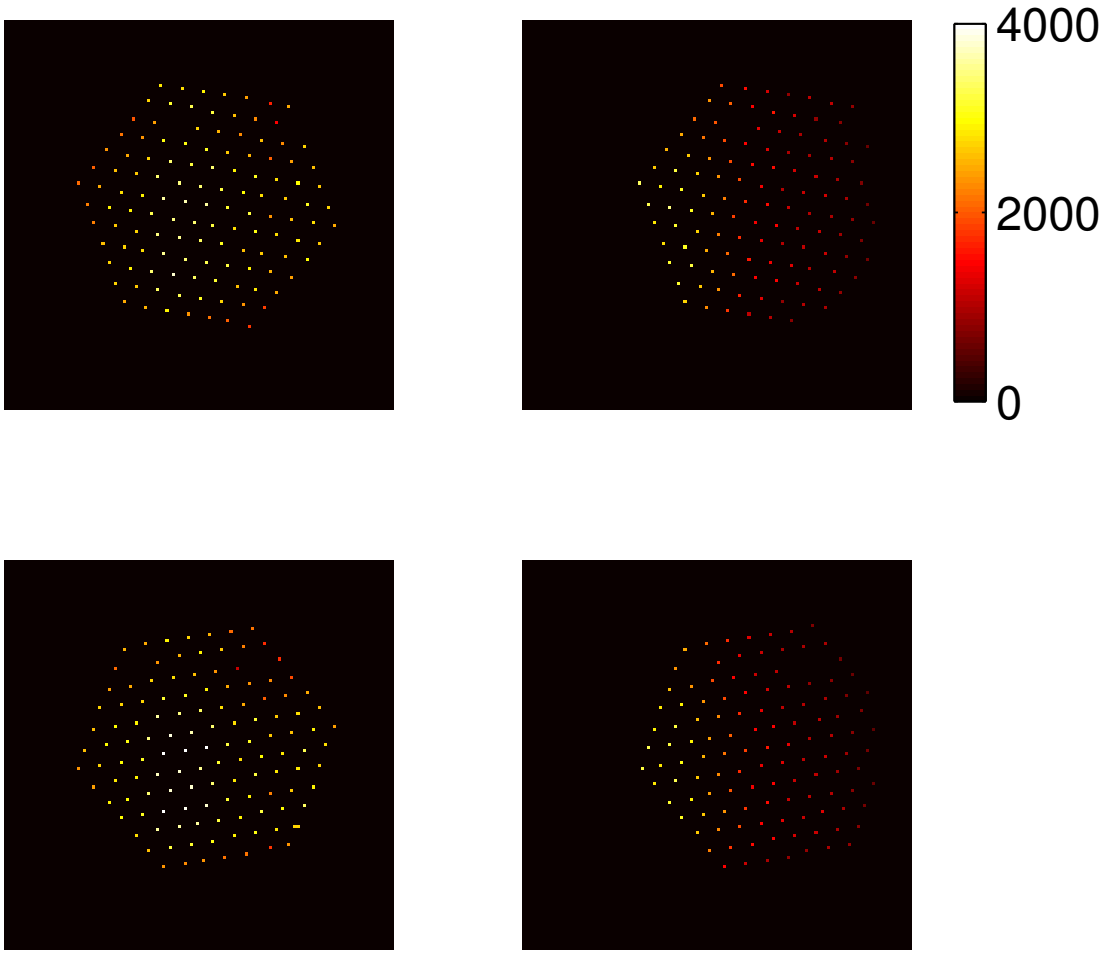

Figure 5.7: Counts in pinhole projections for both aperture sides. The top row is data from aperture side 'A' and the bottom row from the flipped side, 'B'. The left column is for a centered source and the right column is for a source 20 mm off-axis.

angle (depends on the pinhole normal vector), and h is the normal source-to-aperture plate distance (h = d/cos θ). Sensitivity truncation is not a problem since the pinhole opening angles (45° half-cone) means the farthest pinhole still completely views the offset source. The incident angle, θ, is found by treating d as a vector (pointing from the pinhole to the source) and taking the dot product with the pinhole normal vector (which points from the pinhole to the focal spot).

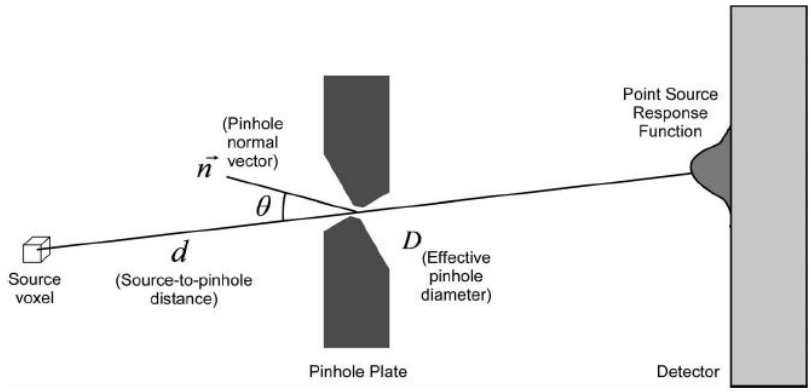

Figure 5.8: Pinhole imaging and sensitivity schematic (from [115]). Activity projects through the aperture onto the detector. Pinhole sensitivity depends upon the four labeled parameters and is the integral of the point response function.

To make the simulated data more accurately resemble the measured data, we boosted the sensitivity by an amount proportional to the counts gained from the parallax effect. Photons going through the outer pinholes impinge on the detector at greater angles of incidence, thus their path lengths through the detector material are larger, increasing the likelihood of interaction. Based on the angle between the source and the pinhole, a relative increase in the sensitivity is calculated based on the higher path length in the DSSD (Fig. 5.9).

The path length, L, through the detector for a non-normal-angle photon is:

$$L = \frac{d}{\cos\theta}, \tag{5.2}$$

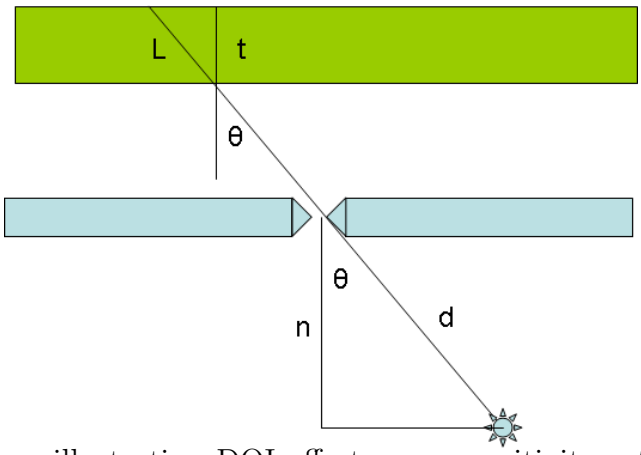

Figure 5.9: Cartoon illustrating DOI effect upon sensitivity estimation for a non-tilted, knife-edge pinhole. Photons that have a non-normal incidence angle upon the detector travel through more detector material (L), and thus have higher detection efficiency.

where d is the detector thickness (0.1 cm) and θ is the same as in Fig. 5.8. The fraction of attenuated photons is:

$$A = 1 - e^{-\mu L}, \tag{5.3}$$

where μ is the total linear attenuation coefficient of 27 keV photons in silicon (4.45 cm^{-1}). Approximately 36 % of normal-incident 27 keV photons are detected in 0.1 cm of silicon, so an increase factor, F, can be calculated to increase the ideal pinhole sensitivity value:

$$\begin{aligned} F &= 1 + \frac{A - .36}{.36} \\ G_{DOI} &= G_{ideal} \cdot F \\ G_{DOI} &= G_{ideal} \cdot \left(1 + \frac{1 - e^{-.445/\cos\theta} - .36}{.36}\right). \end{aligned} \tag{5.4}$$

Table V.2: Simulated sensitivty for the flipped-aperture configurations shown in Fig. 5.7. The source was either directly in front of the central aperture or 20 mm off-pinhole axis. The source was 20 mm from the aperture plate in all cases.

Source position	Focusing side sensitivity	Non-focusing side sensitivity	Percent Difference
On-axis	0.098 %	0.071 %	31.95 %
Off-axis	0.057 %	0.051 %	11.11 %

The modified pinhole sensitivity for DOI, G_{DOI}, was calculated from the four simulations to better mimic the measured data. The pinholes shared a common focal spot 3 cm from the central pinhole axis. The factor F was calculated the same for both sides of the aperture plate since the incident angles of the photons passing through to the detector do not change in either case (just the flux changes).

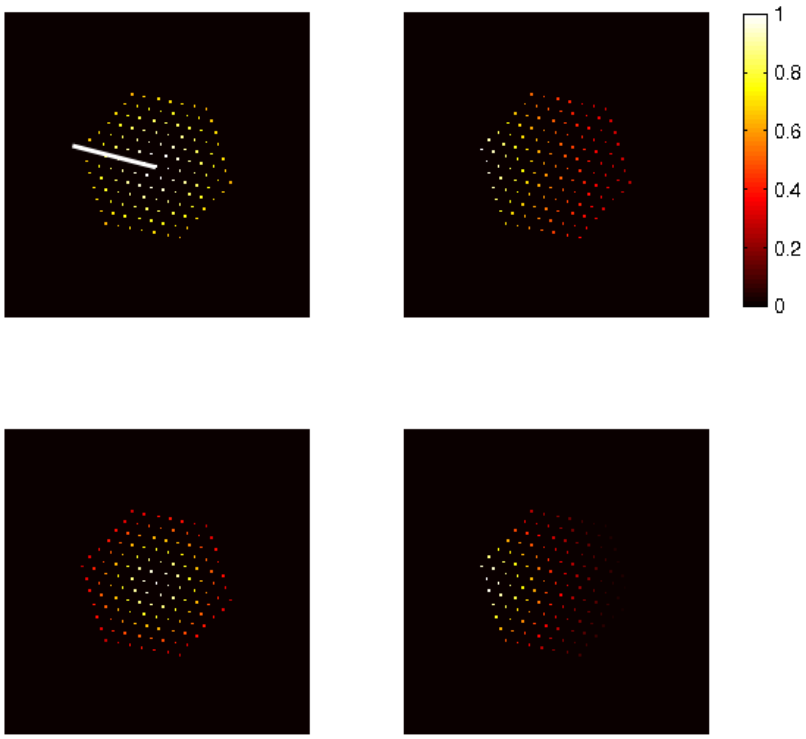

Figure 5.10: Simulated sensitivity maps for a multi-pinhole aperture. The results in this figure correspond to the measured sensitivity in Fig. 5.7. Profiles (Fig. 5.11) were drawn through seven pinholes as indicated by the white line in the top right image

Comparing Tables V.2 and V.1, the expected sensitivity difference between the

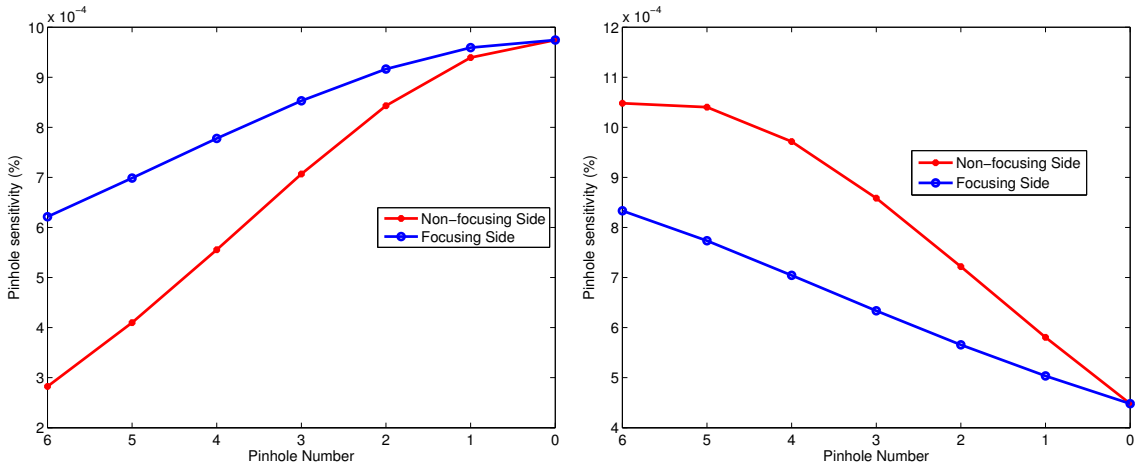

Figure 5.11: Sensitivity profiles for focusing and non-focusing aperture sides for a source directly in front of the central pinhole (a) and 20 mm off-axis (b).

two sides (focusing and anti-focusing) is an order of magnitude larger than the measured differences. Plus, the sensitivity maps are very different in the simulated and measured data when the source is off-axis or on-axis. Thus, we conclude that the apertures were not made to specification regarding the tilt angles, and that they appear to not be tilted at all.

5.4 Simultaneous stacked detector data acquisition

To demonstrate simultaneous stacked detector acquisition, which SiliSPECT depends upon, we made a simple "line-pair" phantom out of two Oncoseeds. The seeds are 0.8 mm in diameter and then were placed in 1.1 mm inner-diameter capillary tubes with wall thickness of 0.2 mm. The tubes were positioned right next to each other so the seed separation distance was 2.6 $\pm$0.2 mm. The seed phantom was placed in the center of the field of view, which is about 4.5 cm from the central pinholes. The four coincidence images are shown in Fig. 5.12.

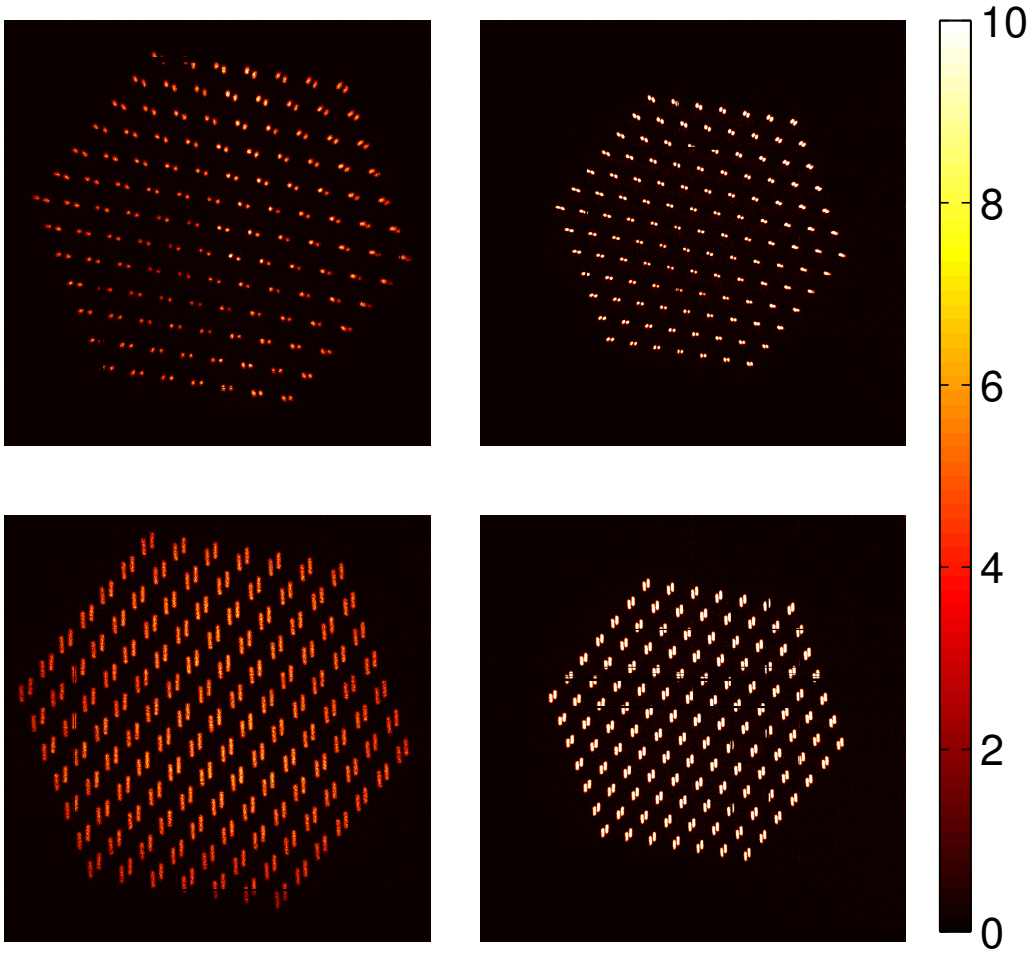

Figure 5.12: Simultaneously-acquired stacked detector projection images from seeds in capillary tubes. The two seeds were parallel with respect to the aperture on head 2, so they were resolved better in the images from head 2 (bottom row). Head 1 detectors view the sources from above, so the sources are not as well-resolved in the front detector projection image. The back detector projections are in the left column and the front are in the right column.

Since the seeds were easy to distinguish, we removed the seeds from the glass tubes and placed them directly next to each other (Figs. 5.13 & 5.14). This time only the seeds in the high-magnification projection image are distinguishable. This example also shows that the presence of the front detector does not degrade the projection on the back detector. The tails of the distribution would be expected to be larger if there was significant scattering in the front detector.

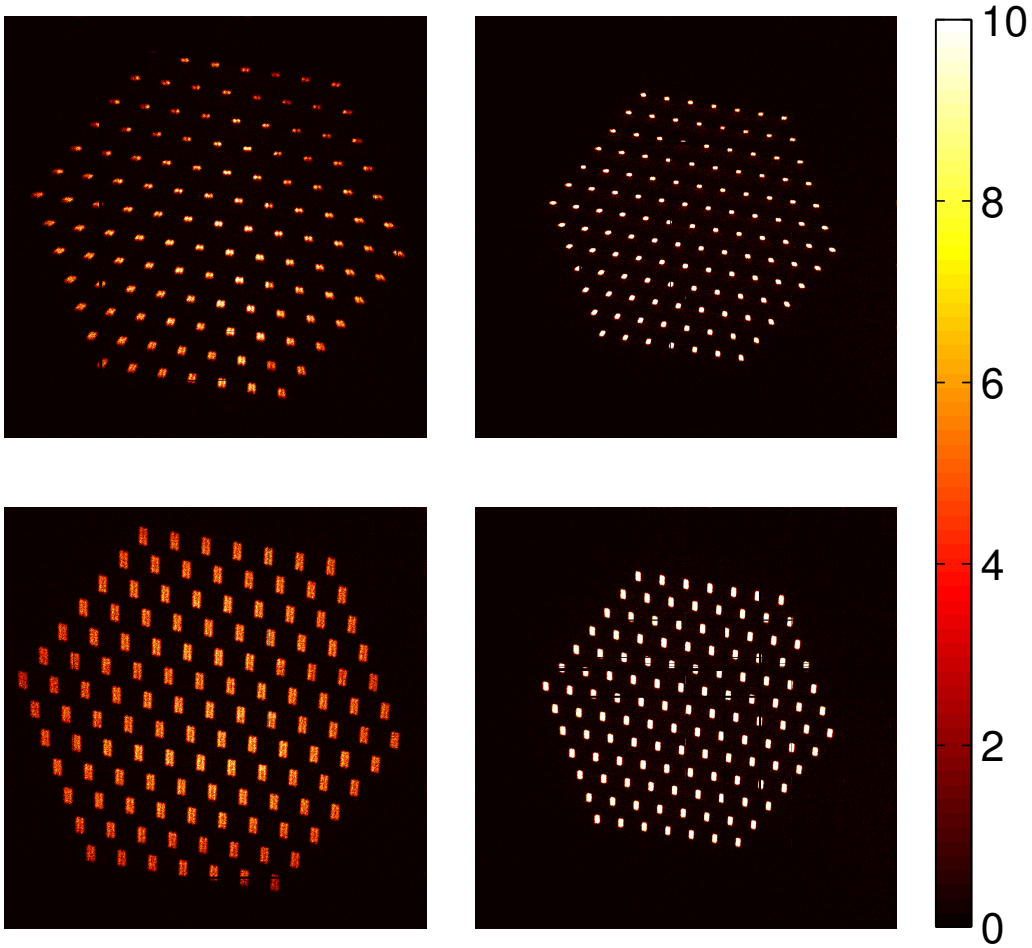

Figure 5.13: Simultaneously-acquired stacked detector projection images from adjacent seeds. Head 1 (top in Fig. 5.2) is the top row, and the back detectors are in the first column while the front detectors are in the right-most column. The two seeds were parallel with respect to the aperture on head 2, so they were resolved on that back detector.

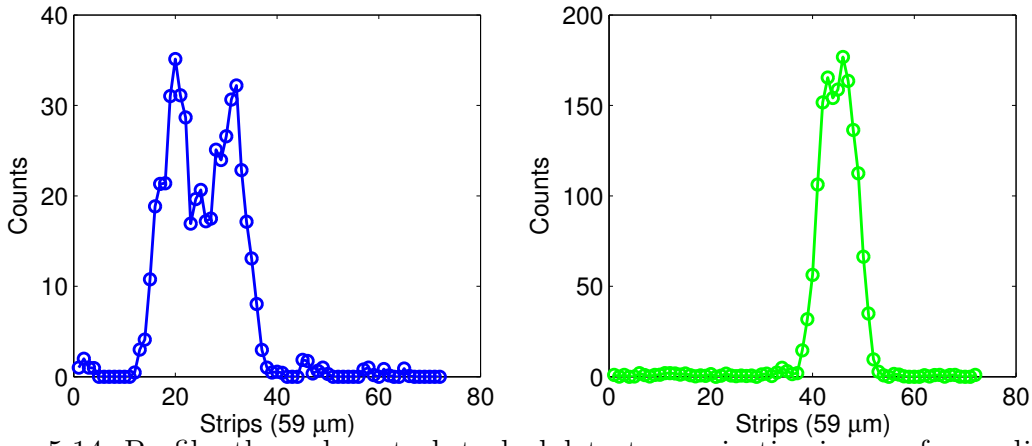

Figure 5.14: Profiles through central stacked detector projection images from adjacent Oncoseeds. The back detector profile is on the left and the front detector profile is on the right.

5.4.1 Estimating magnification parameters

The distance from the aperture to the detectors can not be measured once the camera box is closed, and even when it is open the measurement requires making multiple micrometer measurements. Multiple distances must be known for the micrometer reading to be accurate, such as the recessed aperture plate shelf and the distance from the ceramic frame to the surface of the detector crystal, the latter of which cannot be safely measured. So several methods were employed to estimate the magnification parameters.

First, we utilize the equations governing pinhole imaging (Fig. 5.15):

$$M = \frac{a}{b}, \tag{5.5}$$

$$p_i = \frac{aw}{b_i} \;\Rightarrow\; a = \frac{p_i b_i}{w}, \tag{5.6}$$

and

$$b_i = b_0 - i\Delta b, \tag{5.7}$$

where Δb is the step length, b_0 is the source-aperture distance, and p_i is the projection width, and i is the step number. Substituting Eq. 5.7 into Eq. 5.6 yields:

$$a = p_i(b_0 - i\Delta b)/w. \tag{5.8}$$

This last equation can be rearranged to:

$$i\Delta b = -(w/p_i)a + b_0. \tag{5.9}$$

If we plot $i\Delta b_i$ versus -w/p_i the slope is equal to the focal length (a) and the intercept is the original source-aperture distance, b_0.

A single Oncoseed was positioned ~100 mm (measured with micrometer) from the center of head 2's central pinhole. The seed was stepped toward the aperture 18 times in 5 mm increments. The acquisition time at each step was 10 min. The length of the seed projection was measured and Eq. 5.9 was fit to the data. The method is illustrated in Fig. 5.16 and results are given in Fig. 5.17 and Table V.3. Overall the results from this method were in line with what was measured with a micrometer (when the detectors were accessible within the box). The measurements are sensitive to the number of counts in the projections, how thick of a line profile is used, and what value is used for the length of the object. We have conflicting documentation on the length of the Oncoseed active element (from 2.8 to 3.0 mm). We're also not

sure about the gap between the silver rod and the titanium capsule; some activity could have moved from the rod, making the effective length longer. Changing the length of the seed from 2.8 to 3.1 mm affects the results by a few millimeters.

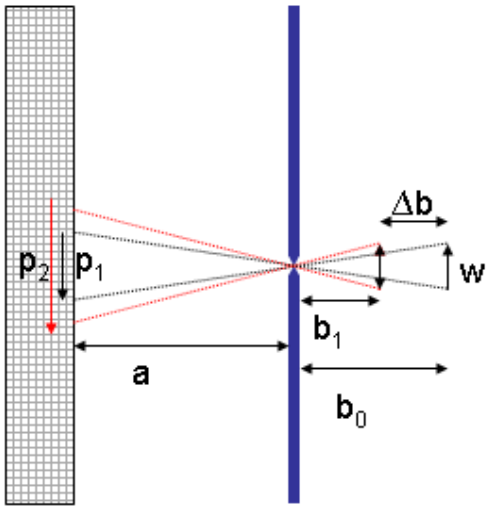

Figure 5.15: Diagram of pinhole magnification of object.

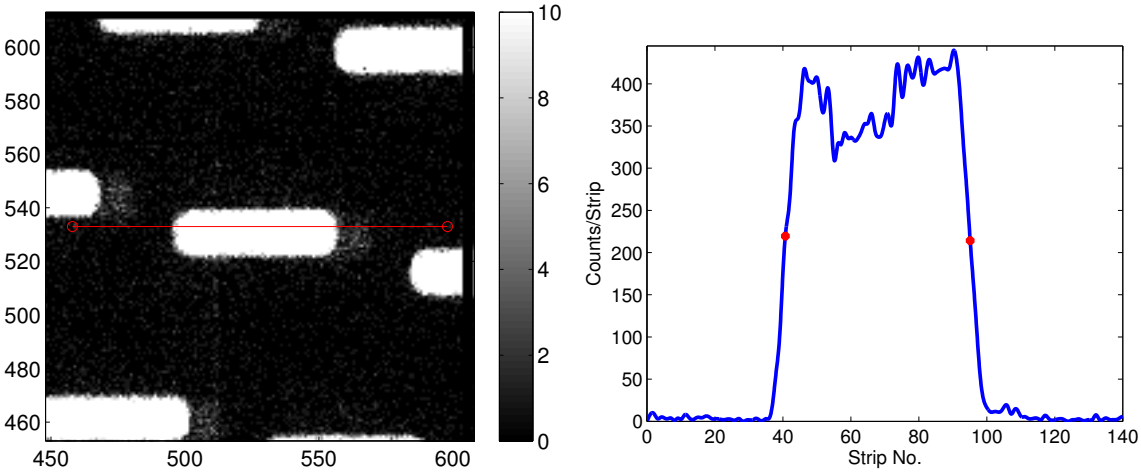

Figure 5.16: Zoomed view of seed projections on front detector of head 2 (left) and profile through central projection (right) . The FWHM of the profile was calculated from interpolated data (factor of 100) to get a more accurate estimate.

The results for the magnification parameters let us calibrate the micrometer head values to the aperture-detector distances. When the box was opened, we noted the minimum and maximum distances the micrometer heads could move the detectors.

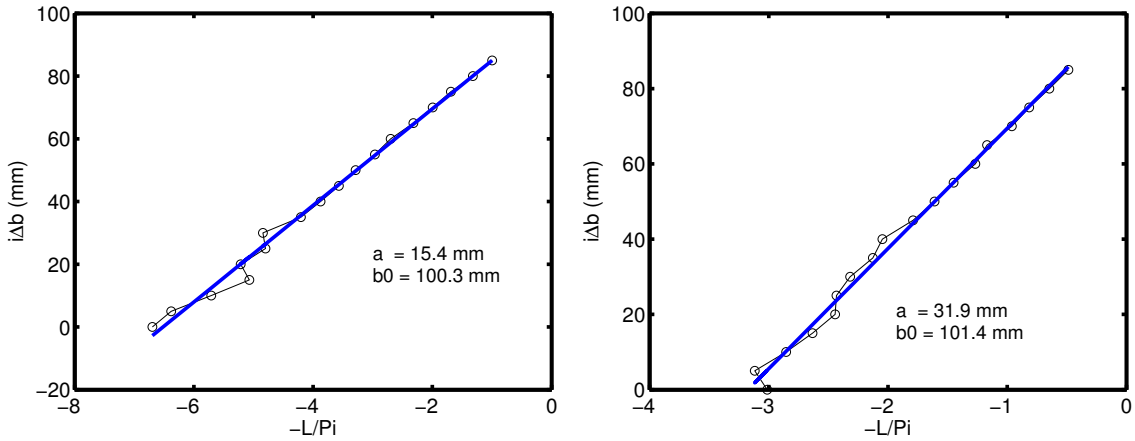

Figure 5.17: Fit results for extracting the magnification factors on the front (a) and back (b) detectors of head 2. At lower magnification (left part of plots), there are fewer counts and fewer pixels with signal so the measurements are noisier. Just as good results could be had by only considering the high-magnification points.

Table V.3: Estimated magnification factors and measured for both detectors in head 2.

	a_{front}	a_{back}	b_{0front}	b_{0back}
Measured (mm)	15.1	33.0	101.0	101.0
Fit (mm)	15.4	31.9	100.3	101.4

The front detector can only be pushed so far until its components are mashed up against the front of the box, and both heads do not move back fully to the back-side of the box. Table V.4 contains the micrometer readings and detector distances for these limits. Fig. 5.18 shows the range of micrometer and detector distances for both heads. The error bars on the front detector plot indicate the distance the back detector must be based on the front detector's position. For instance, when the front detector micrometer reads 2.0, the back detector micrometer must have a value of 10 or greater. This is where the extent of the error bar ($\sim$29) intersects the back detector line. There must always be at least 16 mm between the detectors to ensure that the board components do not touch.

Table V.4: The limits of detector magnification and micrometer travel. The magnifications are calculated with the source-to-aperture distance of 45 mm. All units in the table are in millimeters. M is the magnification (a/b). Mic. is the micrometer reading. The fitted values of a_{front} and a_{back} in Table V.3 were when the micrometers read 3.00 mm and 11.00 mm, respectively. This allows new values to be calculated (e.g., a_{front} = 15.4 - (Mic.$_{front}$ - 3)).

Micrometer	Mic.$_{front}$	Mic.$_{back}$	a_{front}	a_{back}	M_{front}	M_{back}
Max	19.38	25.18	31.78	46.08	0.71	1.02
Min	-2.29	3.43	10.11	24.33	0.22	0.54

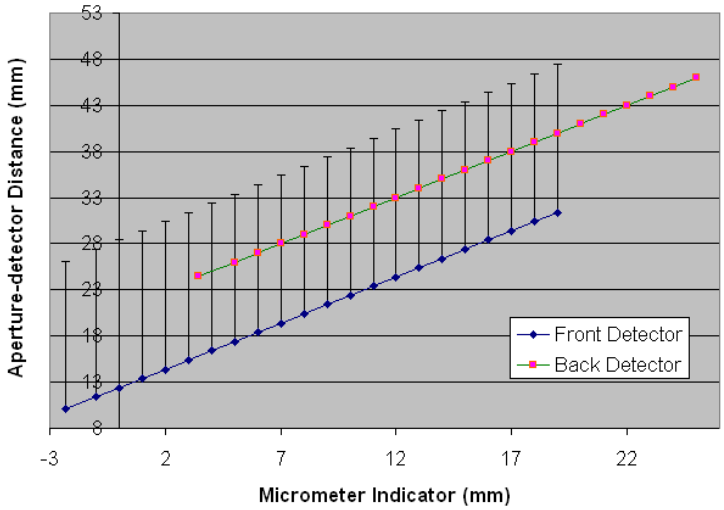

Figure 5.18: Range of micrometer readings versus the stacked detector positions. The detectors must be kept at least 16 mm apart, which is shown by the error bars on the front detector. The front micrometer reading rolls around to large positive numbers as it dips below zero, but negative numbers were plotted for clarity (so 97.7 on the micrometer is actually -2.29 here).

An easier way to obtain the magnification is to use two seeds separated by a known distance. This way only the centroids of the projections need to be found, which is much less sensitive to counting statistics than the full-width at half-maximum measurement used to measure the profiles of the projections. Plus, the exact length of the object need not be known. The magnification can be extracted with a single measurement (but not a & b). We use this method in the next section to measure the magnification and the system spatial resolution.

5.5 Planar resolution

Pinhole planar image resolution is dependent on the pinhole diameter, detector resolution, and magnification, making it a shift-variant property within the object space. We evaluated the planar resolution for the typical geometry envisioned for SiliSPECT. The projections from the two seeds in the capillary tubes (Fig. 5.12) were all well-resolved and could be used to easily estimate the magnification, M. Since we know the distance between the seeds ($\sim$2.6 mm), we only need to measure the distance between the projection centroids (or peak-to-peak distance in a line profile through the projections) to calculate M.

Profiles through the central projections on head 2 (Fig. 5.19), which sees the lengths of the seeds (bottom half of Fig. 5.12), are shown in Fig. 5.20. The width of the profiles in the back detector are increased due to the magnification, but there are no major degradations in the back image from the presence of the front detector. The peak-to-peak distance for the back detector is 19 strips and the front detector is 9 strips. Converted to millimeters, the distances are 1.121 mm and 0.531 mm,

respectively. Magnification is the image size divided by the object size (M_{back} = 1.121/2.6 = 0.43 and M_{front} = 0.531/2.6 = 0.204). The projections on both detectors are minified (magnification less than 1). Next we calculated the planar resolution on both detectors for an infinitely thin source using Eq. 2.1:

$$
\begin{aligned}
R_{sys} &= \sqrt{d^2(1+1/M)^2 + (R_i/M)^2} \\
R_{sys,b} &= \sqrt{0.25^2(1+1/0.431)^2 + (0.059/0.431)^2} \\
R_{sys,b} &= 0.84\ mm \\
R_{sys,f} &= \sqrt{0.25^2(1+1/0.204)^2 + (0.059/0.204)^2} \\
R_{sys,f} &= 1.50\ mm.
\end{aligned}
$$

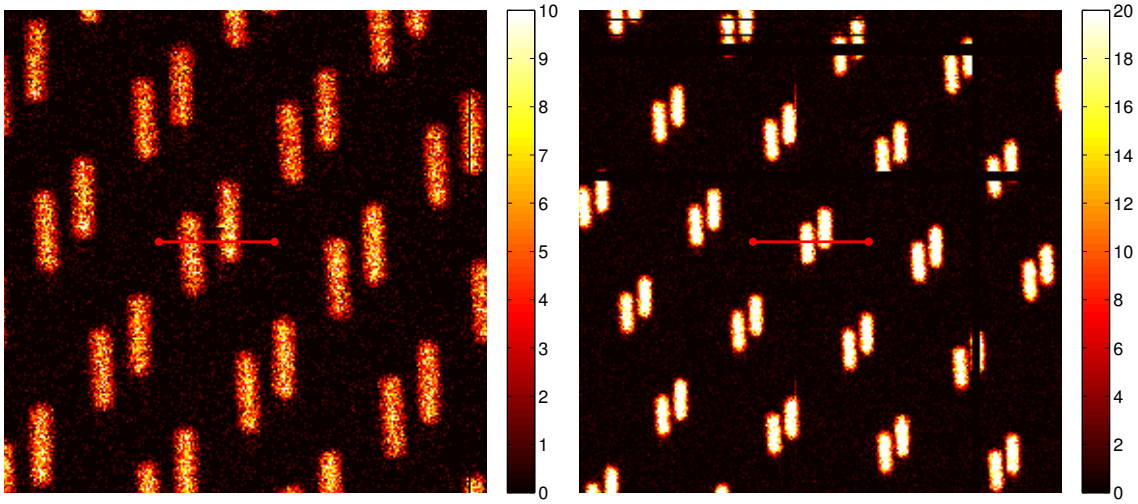

Figure 5.19: Zoomed projection images on the detectors in head 2 from two Oncoseeds placed 2.6 mm apart. Line profiles were drawn across the central projections on the back (a) and the front (b) as indicated by the lines.

Eq. 2.1 estimates the PSF-width for delta-function inputs (infinitesimally small

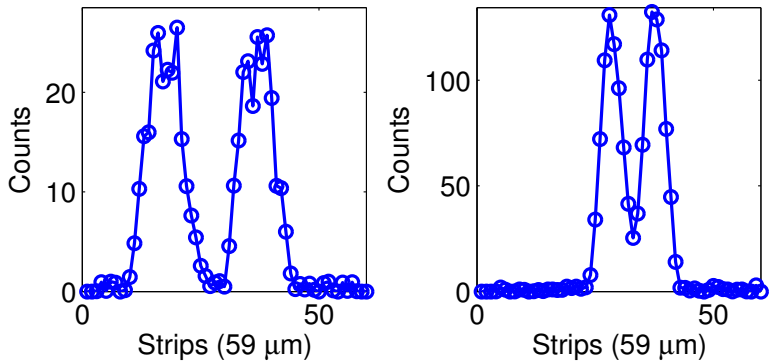

Figure 5.20: Profiles (back on the left, front on the right) through central pinhole projection images from seeds in capillary tubes.

objects). To estimate the spatial resolution for finite objects (like the seeds), a step function of width 0.5 mm (width of seed) was convolved with a Gaussian with FWHM equal to the planar resolution. This is illustrated in Fig. 5.21. The left plot shows a Gaussian function with FWHM equal to the planar resolution. The middle plot shows the step function and the right plot is the result of the convolution, or the planar resolution blurred by the object size. The measured FWHM of the projection profiles can then be compared to the convolved estimate. The FWHM was assessed by interpolating the data in Matlab by a factor of 100, finding the peak index, and then finding the indices of the FWHM (instead of fitting a Gaussian). This approach should reduce discretization effects. Results for the measured projection widths and the estimated resolution are shown in Table V.5. The measured FWHM of the front and back detectors matches well with the expected FWHM from the convolved function. The estimated resolution is less than the measured resolution in both cases. This is expected, as several other processes may add to the blurring that are not included in the estimate (such as charge-sharing and scattering). The measured FWHM on the back detector has a greater difference from the expected resolution compared

Table V.5: Measured and theoretical planar resolution on both detectors with an Oncoseed phantom. $FWHM_{meas.}$ is found by interpolating the count profiles (to get a more accurate estimate), finding the FWHM, then dividing by the magnification. Similarly, once $FWHM_{conv.}$ is calculated, its FWHM is found and converted into object space by dividing by thee magnification.

Detector	Magnification	R_{sys} (mm)	$FWHM_{meas.}$ (mm)	$FWHM_{conv.}$ (mm)
Back	0.43	0.84	1.17	0.91
Front	0.20	1.50	1.56	1.53

to the front detector. This is attributed to the larger amount of scattered photons in the back detector (which scatter in the front detector before interacting in the back detector). Also, the active elements of the seeds are not perfect squares, but cylindrical shells of activity on a silver rod.

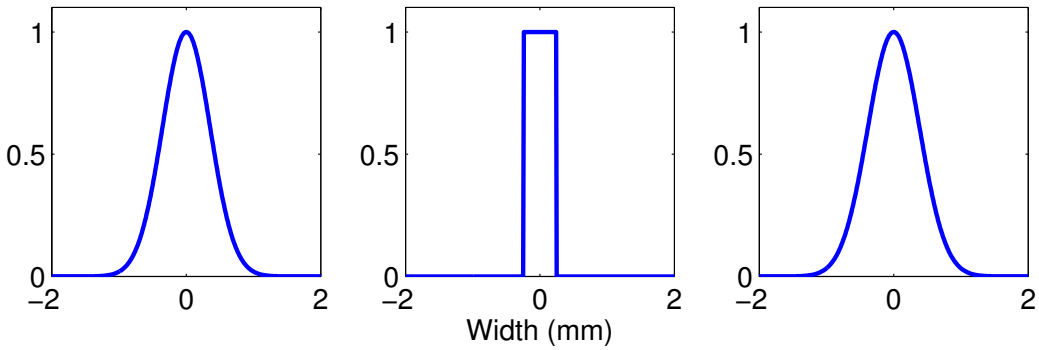

Figure 5.21: The pinhole planar resolution (Eq. 2.1) (left) is convolved with the object size (middle) to produce the expected point spread function (PSF) on the detector. The resolution in object space is found by dividing the the FWHM of the convolved Gaussian by the magnification.

Regardless of the uncertainties in the resolution measurements, these results show that with stacked detectors, multiple images with different resolution are acquired simultaneously. The higher-resolution image provides extra information about the object. Similarly, the lower-resolution image has less projection overlap. When combined into an iterative reconstruction algorithm, these competing effects provide complementary information that aids reconstruction.

5.6 System sensitivity

Sensitivity is a measure of how effective the system is in collecting the emitted photons. The sensitivity, S, is defined as:

$$S = \frac{N}{tAP}, \tag{5.10}$$

where N is the number of detected photons, t is the acquisition time in seconds, A is the activity in Bq, and P is a factor giving the number of emitted photons per decay. For ^{125}I, P is $\sim$1.35 for photons above 5 keV (the lower-energy photons are attenuated in the titanium shell of the Oncoseed and are probably below the DSSD thresholds anyway).

The total system sensitivity was simulated to be 0.08 % for a point source placed 2 cm from both detector heads and with tilted apertures [78]. However, the real apertures are not tilted, and because of the way the boxes were constructed, for a point source to be equidistant from the two central apertures, the aperture-object distance is nearly 4.5 cm. A 186 μCi Oncoseed was used as the source and the acquisition time was 25 min. The system sensitivity was measured to be 0.0133 %. Head 1 counted 0.0069 % and head 2 counted 0.0064 % of emitted photons. Considering the $1/r^2$ falloff of sensitivity, these numbers are quite close to the simulated sensitivity of 0.08 % at 2 cm. Sensitivities for the detectors in camera head 2 for several distances are plotted in Fig. 5.22.

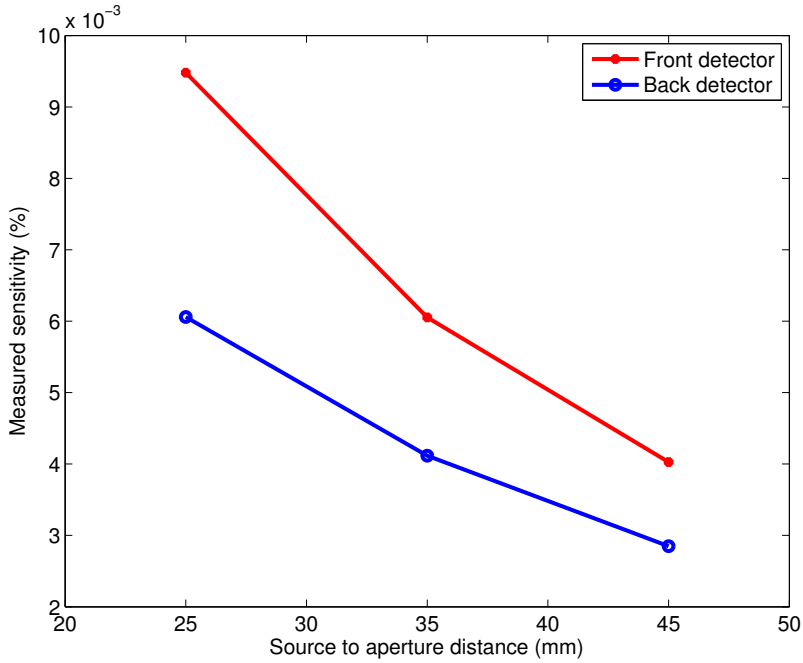

Figure 5.22: Sensitivity (with DOI effect added) vs. source to aperture distance for front and back detectors of head 2.

5.7 Depth-of-interaction effect estimation

The depth-of-interaction (DOI) effect, or parallax, shifts the expected projection centroids depending on the incidence angle of the photons. It is a significant source of spatial blurring in high-resolution pinhole imaging systems. Considerable efforts have been made to accurately model this effect or to estimate the depth of interaction of each photon with specialized instrumentation. To estimate how much the DOI effect may impact SiliSPECT, we turn to equations developed by S. Metzler [116].

Metzler derived the mean shift in the projection centroid parallel to the detector surface, $\overline{\Delta\eta}$, based upon the incident angle, θ, the linear attenuation coefficient, μ, (for the detector material and photon energy), and the detector thickness, T:

$$\overline{\Delta\eta} = \frac{1 - (1 + \mu T \csc\theta)\, e^{-\mu T \csc\theta}}{(1 - e^{-\mu T \csc\theta})\, \mu} \cos\theta. \tag{5.11}$$

The largest incident angle we expect can be calculated by considering the edge of the FOV and the farthest pinhole aperture from that location. We expect the FOV to be no more than 3 cm in diameter, so part of the object could be 1.5 cm away from the central pinhole axis. The outer pinholes are also 1.5 cm away, and the closest the object might be is 3.0 cm with the current camera heads. So the maximum angle is $\arctan 3/3 = 45°$. For $\mu = 0.445$ mm^{-1} and T = 1.0 mm, Eq. 5.11 evaluates to a mean shift of 0.955 mm. This is a shift of nearly 16 strips in one dimension, and is expected based upon the large aspect ratio (material thickness T divided by pixel or strip width w), as displayed in Fig. 5.23. The centroid shift at extreme incidence angles is nearly 1 mm and thus needs to be incorporated in the system model for accurate image reconstruction.

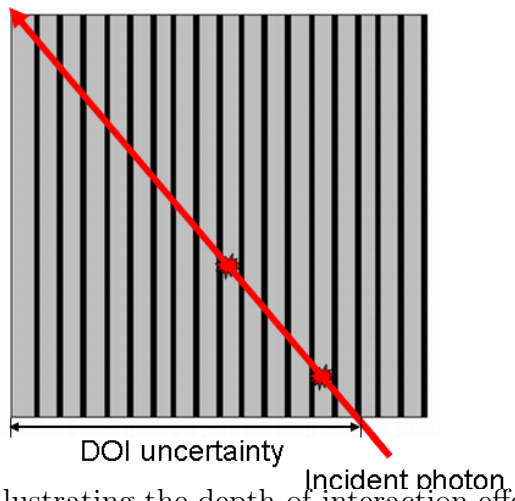

Figure 5.23: Cartoon illustrating the depth-of-interaction effect in the DSSDs with a to-scale aspect ratio. Photons incident at non-perpendicular angles with respect to the detector may interact deeper in the detector, increasing the uncertainty of the photon origin. Because of the long attenuation length, ^{125}I photons in silicon the probability of interaction along the path length is fairly uniform.

5.8 Spatial multiplexing in the field of view

To gauge the amount of multiplexing in the projection images, we filled a spherical phantom 17 mm in diameter, close to the target size of a mouse brain, with 162 μCi of ^{125}I. A NanoSPECT/CT co-registered image of the phantom is shown in Fig. 5.24. Projections of the phantom on head 1 of SiliSPECT are shown in Fig. 5.25. Both detectors exhibit significant amounts of multiplexing. The dark spots in the front detector image are where a single pinhole projection does not have any multiplexing with its neighboring-pinhole's projections.

To better discern the amount of multiplexing, we masked all but the 7 inner pinholes. In the front detector, more than half of the projection area is multiplexed in each pinhole projection. The center pinhole projection is probably around 90 % multiplexed. It is difficult to assess the amount of multiplexing in the back image because of low counts, but we estimate complete 2nd-order multiplexing in each pinhole projection (could have come through 1 of 2 pinholes) and even higher-order amounts of multiplexing. We then masked all but three of the inner pinhole ring so the pinhole-to-pinhole distance was around 5 mm. With this pinhole mask, the front detector's projections were almost distinct. The back detector still had significant multiplexing. This indicates that in order to have non-multiplexed data on the front detector (which may be required for the synthetic collimator method), we need to use a sparser pinhole array. The 3-pinhole mask suggests that an inter-pinhole distance of 5 mm is sufficient to remove almost all the front detector multiplexing for a 17 mm diameter object. This can be accomplished by masking the current pinhole array or

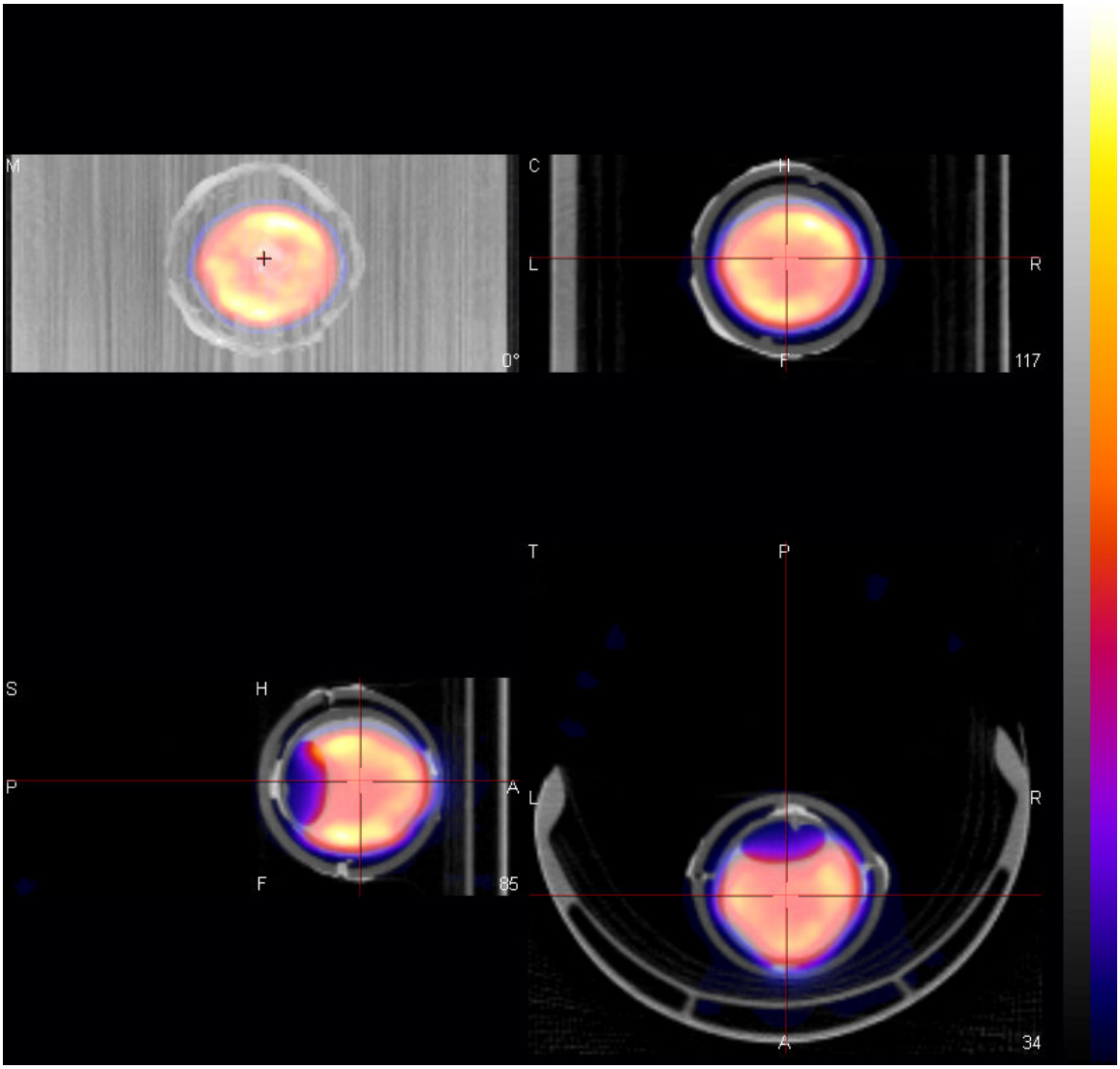

Figure 5.24: Screenshot from InvivoScope program showing NanoSPECT/CT image of spherical phantom. The 17 mm diameter sphere was filled with ^{125}I with the exception of an air bubble. 162 μCi of activity was in the sphere on March 10th, 2010. The fill-hole was plugged with fast-drying epoxy and a 20 mm diameter sphere was halved and then epoxied around the inner sphere to ensure containment of the iodine.

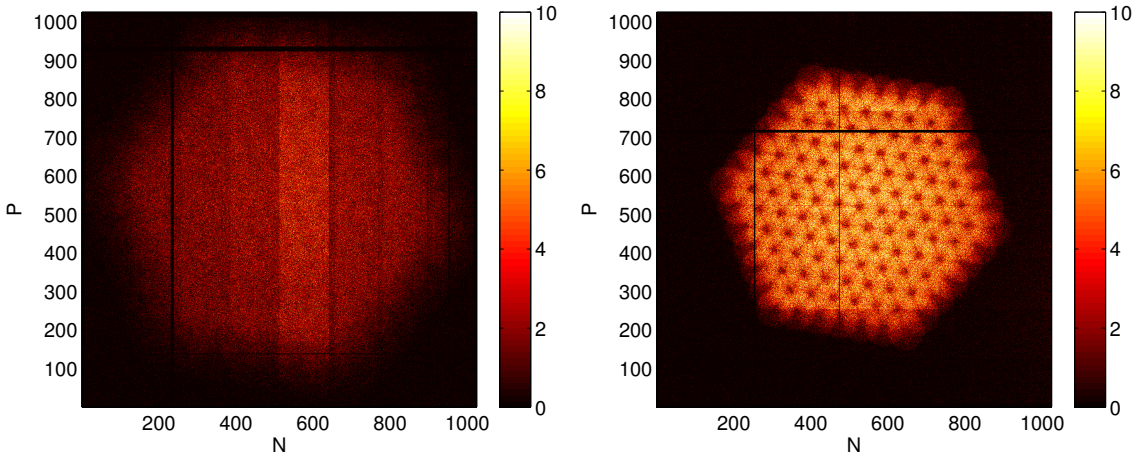

Figure 5.25: Projection image on the back detector of (a) and the front detector (b) of head 1. The sphere was approximately 4.5 cm from the aperture and the detectors were 15.1 cm and 33.0 cm from the aperture plate. The detectors can be moved 5 mm closer, which would reduce the multiplexing. Moving the source farther away also reduces multiplexing but places the object away from the central FOV of the other head.

building new apertures. We have used a jeweler's disc cutter to make small Tungsten discs for making different aperture configurations (Fig. 5.27).

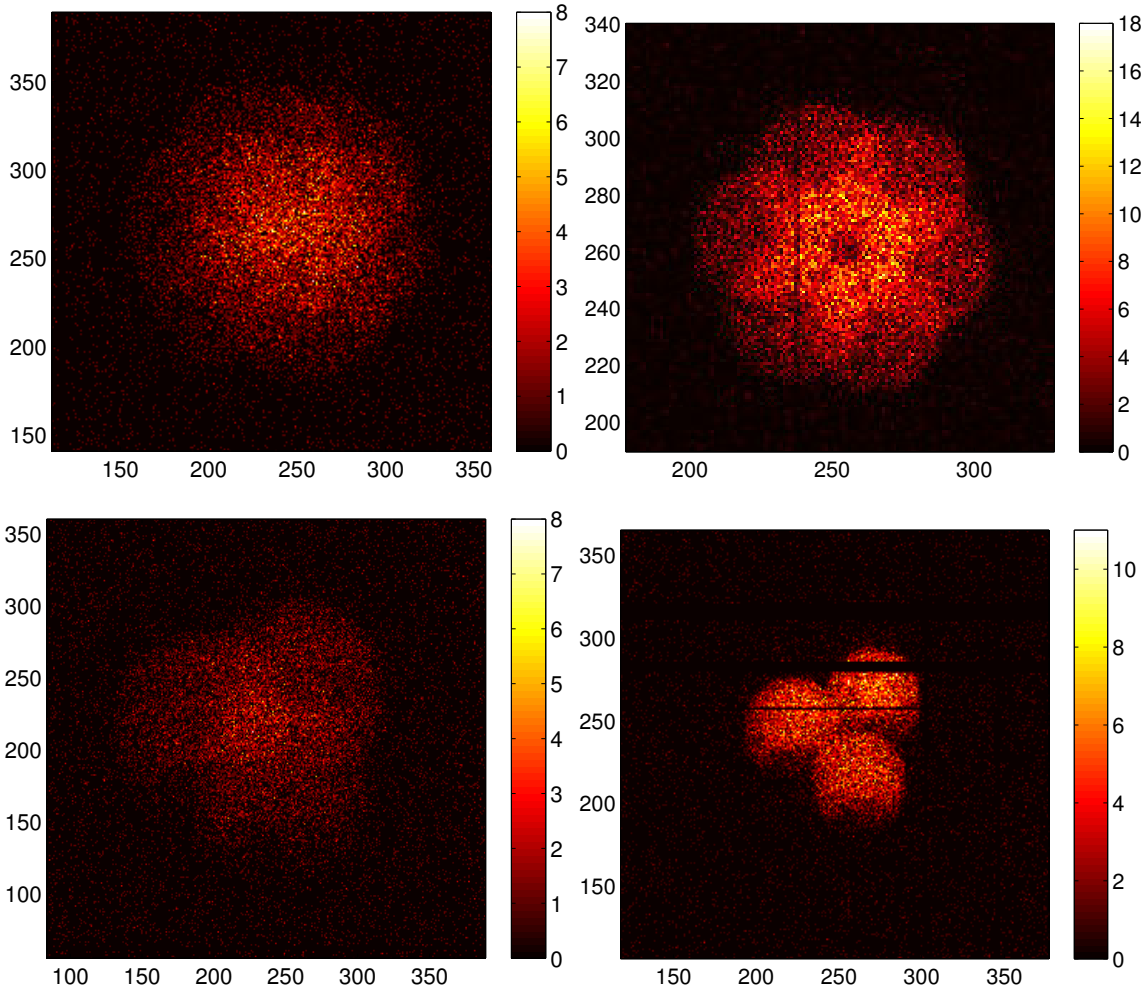

Figure 5.26: Multiplexed projections of the spherical phantom on the back and front detectors of head 1 with 7 pinholes (top left and right, respectively). Acquisition time was 30 min. The dark spots in the pattern on the front detector are where a single pinhole projection is not overlapped by its neighbor-pinhole's projections. The back detector projections are multiplexed beyond recognition. Projection data from head 2 with 3 pinholes unmasked shows less multiplexing on the front (bottom right), but still a large amount on the back detector (bottom left). This acquisition was for 1 hour. The bubble in the phantom is visible in the bottom projections. Images were downsampled to 512x512.

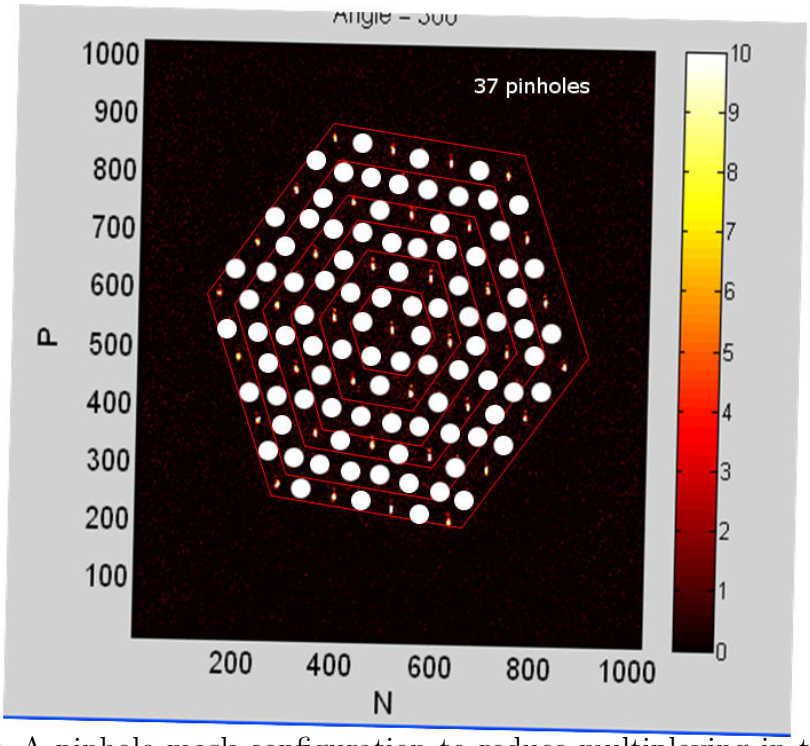

Figure 5.27: A pinhole mask configuration to reduce multiplexing in the projection images. The white circles represent thin metal discs which can be affixed to the plate to block the pinholes. With this mask, only 37 of the initial 127 pinholes remain, but the inter-pinhole distance is doubled to 5 mm.

CHAPTER VI

SILISPECT CALIBRATION

6.1 System matrix generation

The quality of images produced by statistical iterative reconstruction algorithms depends on accurate knowledge of the system matrix, which maps image space into projection space. Perhaps the chief hurdle to making high (<250 μm) spatial resolution nuclear tomographic images is accurate generation of the system matrix. The system matrix describes how an impulse (point source) at each voxel in the field of view maps to the imaging system output (counts in detector pixels). Higher spatial resolution detectors and smaller image voxels make large, unwieldy system matrices. Table VI.1 contains the number of elements and size (in Gb) of system matrices for differing voxel sizes for a 1 cm^3 FOV. The number of pixel elements for four DSSDs is 4,194,304. This number can be reduced by storing only the address and value of pixels with signal for each source position. Since less than 10 % of the pixels have signal for a given point source position, the calculation for the number of system matrix elements is reduced similarly:

$$\#\text{ of system matrix elements} = \left(\frac{\text{cubic FOV length}}{\text{voxel size}}\right)^3 \cdot (\approx 0.1) \cdot (\text{Total pixels}) \quad (6.1)$$

Several approaches have been developed for generating the system matrix. Full measurement of the matrix with a point source is ideal for stationary systems. Other

Table VI.1: System matrix size for different object voxel sizes in a cubic array, as calculated by Eq. 6.1. The imaging volume is 1 cm^3 and the number of total detector pixels is 4x4x1024 = 4194304. The number of elements in the system matrix is at most the number of pixels times the number of object voxels. The matrix can be considerably reduced if only the non-zero pixel values and locations are stored. For a multi-pinhole aperture the system matrix has many non-zero elements, but the number of pixels responding for a given point source location is still around only 10 % of the total pixels, which we used in the estimation (419,430).

Voxel size (μm)	# of voxels in 1D	Total # voxels	# matrix elements	Size (Gb)
60	167	4.7×10^6	2.0×10^{12}	3.6×10^3
120	83	5.7×10^5	2.4×10^{11}	4.6×10^2
240	43	3.3×10^4	3.3×10^{10}	6.2×10^1
480	21	9.3×10^3	3.9×10^9	7.2×10^0

approaches estimate the matrix with a combination of analytical and Monte Carlo methods.

Measuring the system matrix with a point source is the way to include all phenomena (known and unknown) into the system matrix. This technique was developed at the University of Arizona [52] and applied in some other systems [117]. A system matrix based on a minimal number of point source measurements has been used in a PET system as well [118]. Measuring a system matrix presents some major practical challenges. It is difficult to build adequately small and hot point sources, especially with volatile and long-lived ^{125}I. Assuming we sampled the 1 cm^3 volume every 1 mm and counted for 10 minutes at each point, this would amount to nearly seven days of counting. One of the main practical difficulties of this is the detector stability, in which thresholds tend to drift over several days. Even if this sparse 7-day data was measured, some modeling of the projections would be needed to interpolate the measured data into a finer grid to match the desired voxel size of the reconstructed images.

Once a model is derived, the size of the matrix can be greatly reduced since only a few parameters need to be stored for each projection (e.g., parameters describing 2D Gaussian detector response). The system matrix, interpolated and model-fit or not, would likely be so large as to have to be stored on disk, and special computational techniques would be required to access and manipulate it in the reconstruction algorithm. If anything about the system changes, such as the position of the detectors, a new system matrix needs to be measured. The high-resolution detectors make even very small changes discernible. For instance, removing and replacing the aperture plate caused changes in the system response (Fig. 6.1).

One approach to estimating the system matrix is to use geometric projections though the pinhole apertures based on analytical derivations. This approach is based on simple equations which can be quickly solved so the matrix elements can be calculated on the fly. This method can be made more accurate by incorporating the estimated effects of Poisson noise, aperture penetration, scatter, and the depth-of-interaction effect in the detector. Many of these effects can be accurately modeled with Monte Carlo methods. Some efforts have been made to completely generate the system matrix with Monte Carlo simulations [119]. However, simulated system matrices cannot contain all imperfections of the imaging system, such as aperture manufacturing tolerances and detector nonuniformity.

For these reasons, we attempted to use a geometrical model of the pinholes to enable a fast, on the fly calculation of the system matrix during image reconstruction.

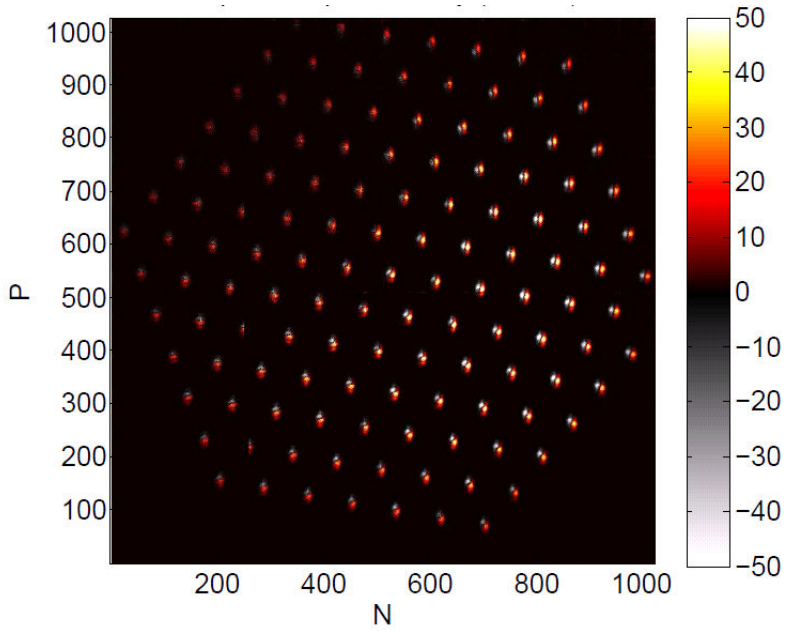

Figure 6.1: Difference image showing the effect of replacing the aperture. One projection image was acquired, the aperture was removed and then reattached, and another image acquired. The second image was subtracted from the first image. The negative pixel values indicate the projection positions of the second acquisition. Tolerances in the mounting screws are probably the largest source of error.

6.2 Geometrical calibration

For any non-measured system matrix, there are a number of geometric calibration parameters that must be accurately known for high-resolution, artifact-free SPECT images. Dr. Shokouhi focused on making an accurate geometric model of the cylindrical pinholes and developed the image reconstruction code [78], while I explored methods of estimating the SPECT calibration parameters. The literature for pinhole SPECT calibration is considerable, dating back to the 1990s. For a single-head, single-pinhole imager, there are seven key parameters that must be known [120]. Fig. 6.2 shows the seven parameters for a single detector (though two are visible in the photograph). Three parameters (often called the intrinsic parameters) do not depend on the position of the detector (f, e_v, and e_u). The focal length, f, is the

perpendicular distance from the detector plane to the aperture plane at the center of an aperture. e_v, and e_u are the electrical shifts, which are a property of the detector and determine photon readout positions. These parameters are exchangeable with the pinhole coordinates (u_i and v_i) [121]. Four parameters (extrinsic) relate the camera to the axis of rotation (AOR) and depend upon the position of the detector. The mechanical shifts (transverse m and axial n) determine the position of the center aperture relative to the AOR. Metzler also calls this "aperture shift" [116]. ROR is defined as the distance from the focal point to the AOR, which runs parallel to the Z-axis. Often ROR is defined as the pinhole-to-AOR distance, but not here. ROR and m describe the distance from the rotation axis to the focal point in the directions parallel (m) and normal (ROR) to the detector plane. Two angles, the twist, Φ, and the tilt, Ψ, describe the orientation of the detector plane and the UV plane (pixel grid) with respect to the AOR.

Most geometrical calibration methods follow the same steps, as outlined by Noo et al. [122]:

1). Place one or more point objects in the field of view and measure the tomographic projection data of the object(s). The relative distances between the objects can be used in the later fitting.

2). Devise a geometrical model that analytically calculates the projections with the set of calibration parameters. Find the experimental centroid locations of these projections for the fitting.

3). Perform a least-squares minimization of the estimated versus the measured cen-

troids values to find the optimal values for the geometrical parameters.

Some of the geometrical parameters are highly correlated, which makes it difficult to find a unique solution with a single point source. Beque et al. showed that three point sources were required with knowledge of their relative distances for single-pinhole SPECT [120]. Wang and Tsui adapted Beque's method to homogenous coordinates, which made it easier to incorporate different acquisition geometries, multiple heads, and more pinholes [121]. They also noted that only two point sources are required if more than one pinhole is being fit. Plus, the distance between the sources is not needed. Recently, Vunckx et al. have examined the uncertainty in the parameter estimates by various metrics [123]. Vunckx noted that supplying the point-source distance or the inter-aperture distances *a priori* greatly helped reduce the noise in the fitting.

Other approaches include the aforementioned Noo et al., where the projection data is fitted with ellipses and geometrical parameters are calculated from the ellipse features [122]. Von Smekal devised a method where the first components of the Fourier series of the projection data are used in the non-linear fitting [124]. These two approaches were designed for x-ray computed tomography; extending them to multi-pinhole SPECT takes some effort. Other approaches are purely analytical, but require complex, well-characterized phantoms (e.g.,[125]). The original approach by Beque uses a simple phantom (2-3 seeds) has a straightforward implementation, and has been proven with other multi-pinhole systems (e.g., [126]).

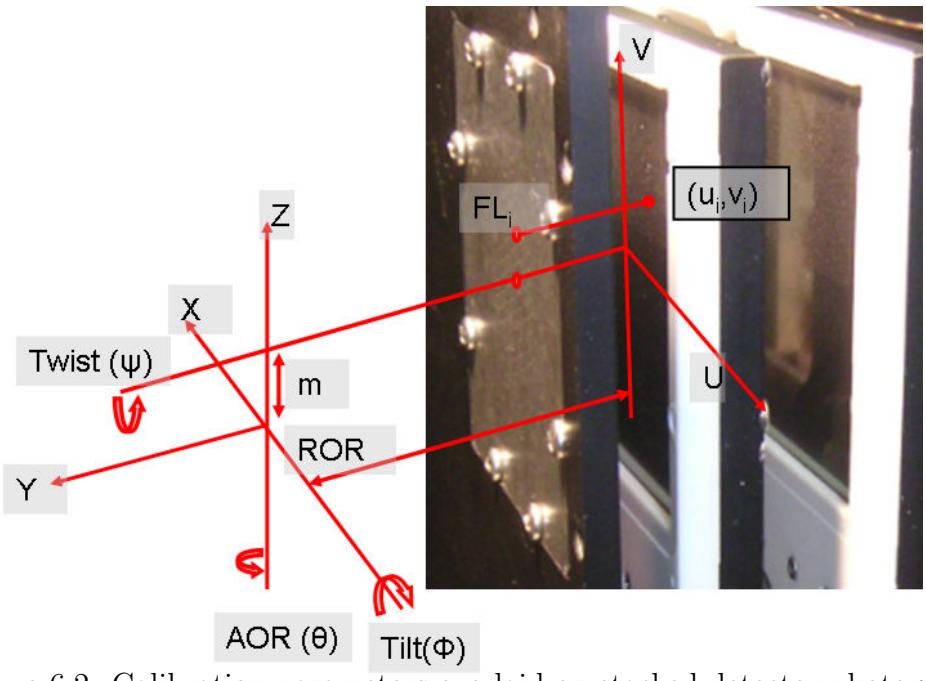

Figure 6.2: Calibration parameters overlaid on stacked detector photograph.

6.3 Calibration data acquisition and processing

We first acquired data with all but the inner seven pinholes masked on each aperture. An acrylic phantom was made to hold Oncoseeds. The phantom was mounted to a motor-controlled rotation stage. Data was acquired in 18 20° steps for two source positions. The source was translated 20 mm axially along the AOR but was kept at the same transverse distance from the AOR. The data was collected separately in two positions with one source instead of using two sources simultaneously because it was more straightforward to match the pinhole projection pairs. Otherwise some of the projections would overlap, which would have made it more difficult to do the next step, which is calculating the projection centroid.

The centroids are estimated using some of the image processing functions (e.g., bwlabel) in Matlab. Then the pinhole-projection pairs are sorted and passed to a

least-squares code that minimizes the differences between the measured centroids and those expected based on the calibration parameters. The fitting code was developed by Beque, Vunckx, and others at Katholieke Universiteit Leuvan in Belgium [42, 120, 123, 127]. It is in the IDL development environment and is based upon the Powell method.

For a single detector the number of parameters that must be estimated is:

$$N = 4 + 3n + 3k, \tag{6.2}$$

where n is the number of pinholes and k is the number of sources. For a single detector, then, there are 31 parameters to fit for seven pinholes (391 parameters for all 127 pinholes). So with 31 unknowns, at least three views of the 2-seed phantom must be acquired (3*14 = 42 equations). The greater the number of projections, the more data the fit has to constrain the problem. We started with 18 views to reduce the acquisition time, but others generally use more in the fitting, such as 60 views. A function *f*, of the N parameters is defined to minimize the difference between measured and calculated centroid positions for each source (i), pinhole, and detector:

$$f = \sum_{n,i,k} \left[\left(x^{n,i}_{meas,k} - x^{n,i}_{cal,k} \right)^2 + \left(y^{n,i}_{meas,k} - y^{n,i}_{cal,k} \right)^2 \right]. \tag{6.3}$$

Example projection images on all four detectors are shown in Fig. 6.3. The centroids for all projections, both seeds, and for all 18 views are plotted for one detector in Fig. 6.4.

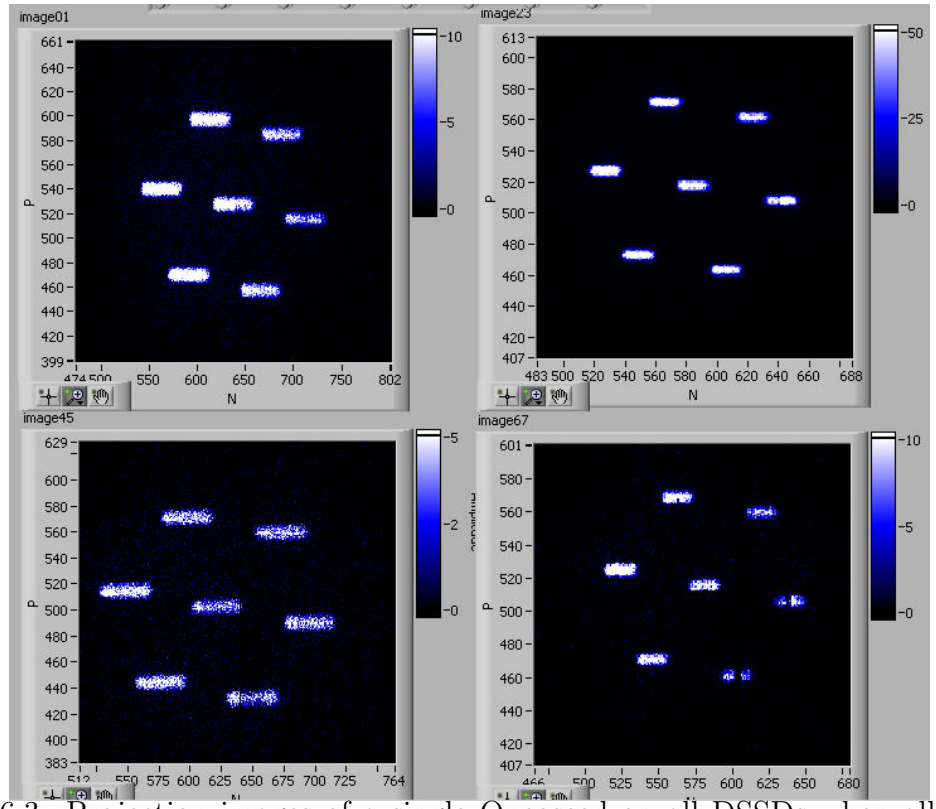

Figure 6.3: Projection images of a single Oncoseed on all DSSDs when all but the inner seven pinholes are masked.

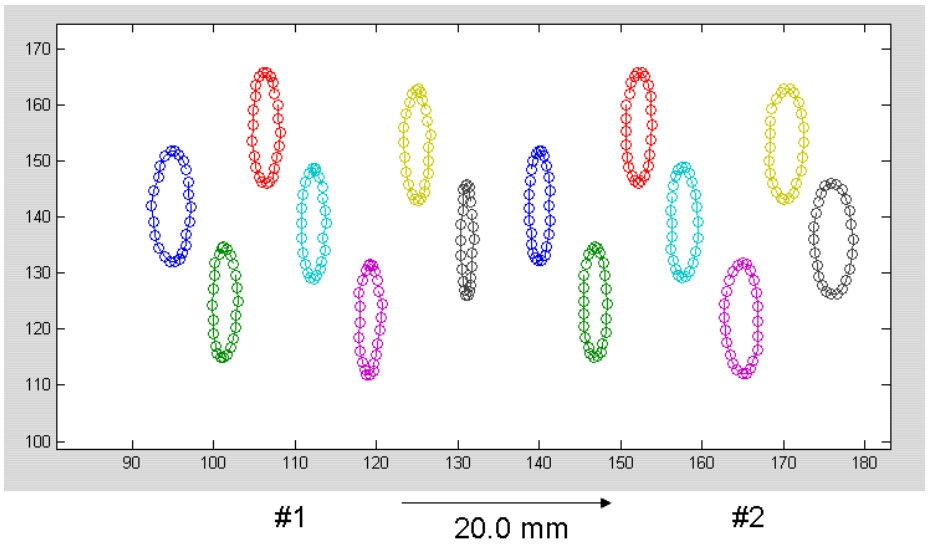

Figure 6.4: Detector 18 projection centroids plotted for each 20° rotation of a seed phantom at two positions. The pinholes projection pairs are matched by color. The detector data was downsampled to 256x256 (0.236 mm pixels). At seed position 1, the projections on on the right. The narrower the ellipse, the closer the source is to being directly over that pinhole.

6.4 First animal images

One of the first set of rat projection images is shown in Fig. 6.5. Rats were directly injected into the interstitial joint of the knee with ∼150 μCi of ^{125}I labeled to an antibody. The open design of SiliSPECT allowed us to position the knee directly in the center of the FOV. We imaged the rats over several time points over four days to follow the biodistribution and clearance of the tracer within the knee. Rats were concurrently imaged with the NanoSPECT/CT system and SiliSPECT. Low-activity Oncoseeds (eventually just one seed) were used as markers for later assistance for sco-registration of the images. Seven pinholes were used initially because we had yet to overcome some of the calibration and reconstruction hurdles, and the problem is much simpler with fewer pinholes. A potential problem is that the angular sampling is lower when only seven pinholes are used, so the reconstructions are expected to have more artifacts associated with limited-angle tomography.

6.5 Current status of calibration and reconstruction

As of this writing, the calibration code has been modified to identify the pinhole-projection pairs (for each separate source measurement). Dead strips have values filled in based on an averaging of the counts in non-dead neighboring strips, so extra regions from bisected projections are not counted. Some minor tweaks to the code are still needed to get it working with 127 pinholes and all detectors. Seven pinholes were initially used since the centroid shift from DOI is not as significant with the lower incidence angles, as illustrated in section 5.7. For 127 pinholes, the measured centroid

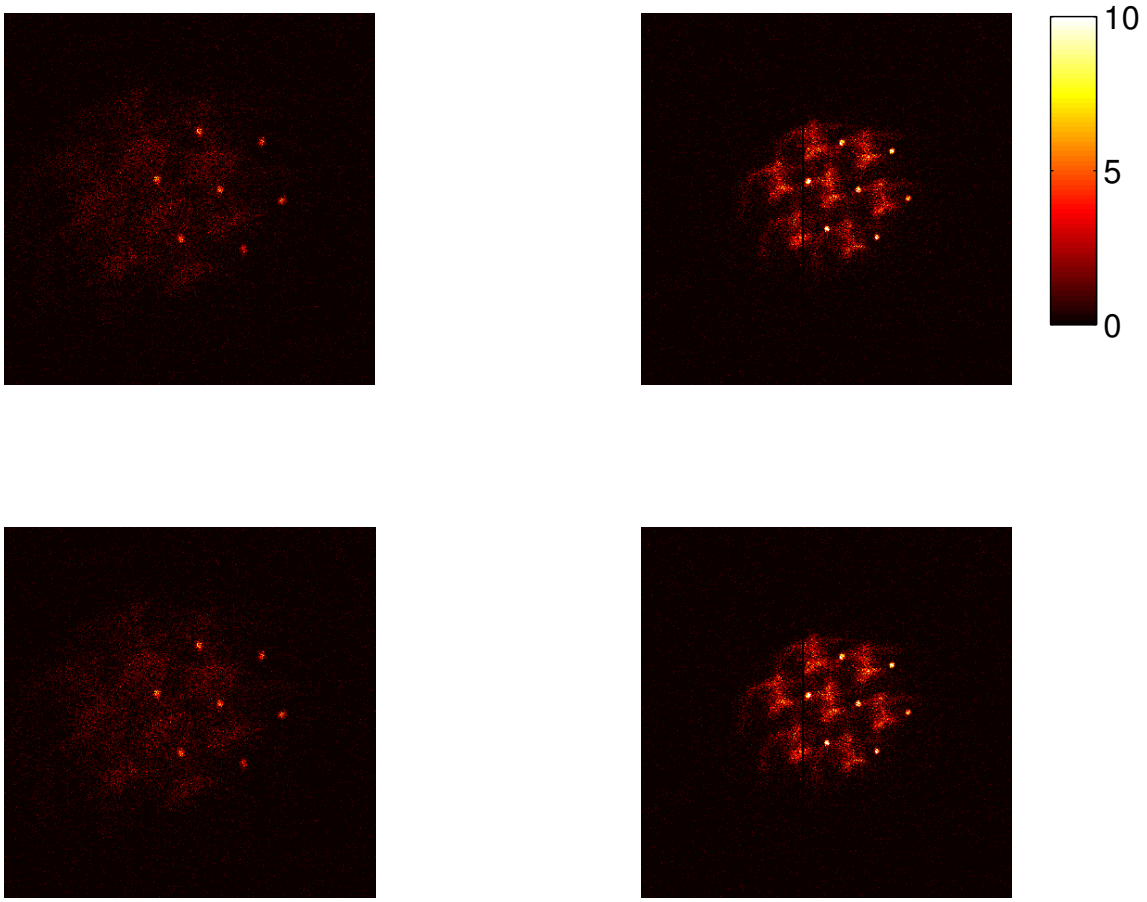

Figure 6.5: Projection images of rat-knee injected with ^{125}I antibody tracer. The hottest spot is a $\sim$20 μCi Oncoseed used for co-registration with the NanoSPECT/CT images. The acquisition time was 30 min and only the inner seven pinholes were used. Head 1 is the top row and the back detectors are in the left column.

data will be shifted to account for the DOI effect to 1st-order using Metzler's formula. This can only be done once the source positions and the central pinhole offsets are known (to compute the incidence angles), so an initial calibration for the central seven pinholes could be used to find this information. Only the central aperture location is needed since the layout of the pinhole array is known fairly accurately. The current reconstruction code assumes perfect geometrical alignment between the heads, so this, and other factors elucidated from the calibration must be implemented in that code. Once these tasks are finished, simple phantoms (Oncoseeds, Oncoseeds on a warm background, etc.) will be measured to test the calibration/reconstruction. If qualitatively-adequate reconstructions are produced with the calibration parameters, then we can try reconstructing the rat knee data that was acquired in December, 2009.

CHAPTER VII

CONCLUSION

SiliSPECT, a novel approach to high-resolution small-animal SPECT, was designed, assembled, and characterized for high-resolution imaging of low-energy emitting isotopes such as ^{125}I. The silicon DSSDs that form the basis of the system were the first mega-pixel detectors used in small-animal nuclear imaging. The DSSD performance characteristics were measured and improved, particularly the low-energy trigger uniformity. This was implemented through an iterative threshold adjustment algorithm, which was required due to the non-uniform and coupled response of the trim DACs. Improving the trigger uniformity boosted the total detection efficiency and overall stability of the detectors, since noisy channels were either found and disabled or their thresholds were trimmed effectively. Forced-air cooling of the detectors kept the detector and electronics cool to provide long-term stable operation.

The count rate limits were explored and found to produce artifacts above 3 kHz, rates that are unlikely to be reached in most animal imaging studies. A method for reducing the artifacts was also investigated. Energy resolution was determined to be only marginally useful. A full energy calibration was prevented due to some chips having very low gain. Some charge-sharing was observed between strips, and more so at higher-energies. The thresholds were low enough to detect most if not all 22 keV charge-shared events from ^{109}Cd, and no excessive double-triggering was observed. The simulated and measured intrinsic detection efficiency matched very

well, showing that any losses from attenuation in the strips, inactive oxide layers, or charge collection inefficiency are minimal.

The dead time was found to vary with the hold delay time. The optimal hold delay was found to be around 1.9 μs, which makes the dead time about 10 μs. At typical count rates of 2 kHz the losses to dead time are less than 1 % of the true count rate.

The 127 pinhole apertures were determined to not be made to specification regarding the tilting angles. This meant that outside FOV activity has a larger contribution to the overall counts. The 2.5 mm spacing between pinholes was determined to permit significant amounts of projection overlap, or multiplexing, on the front detector for a magnification of 1/3 and a 17-mm spherical object (similar in size to a mouse brain, which is the minimally useful FOV). It would probably be best to mask off every other pinhole so the inter-pinhole spacing is 5 mm, or design entirely new apertures.

A graphical user interface was developed to control the detector system, mechanical stages, and list-mode data processing. A real-time coincidence sorter is part of the interface that permits monitoring of detector performance and object positioning within the FOV. These programs should find good use through the life of the detectors.

As the system resolution increases, the challenges associated with generating an accurate system matrix also grow. To avoid some of the practical challenges of measuring and storing a system matrix, an on-the-fly, geometrical system matrix was developed by Dr. Shokouhi. For this method to work, a number of geometrical calibration parameters must be accurately known. We have explored the ways to extract

these parameters and made progress in implementing a robust calibration scheme. The future use of these detectors in SiliSPECT and in other systems may end up requiring a sparsely measured system matrix for accurate reconstructions. We searched for ways to make or buy adequately small (< 0.5 mm) and hot point sources, but currently for ^{125}I, no such sources yet exist.

7.1 Future directions

Thicker aperture plates with cylindrical, or small-opening angle holes would do a better job of shielding for out of FOV activity, which may be a problem with the current apertures. The animal data we have taken with SiliSPECT was for a highly localized source, but in many studies the majority of the activity is in an organ like the bladder that would be outside the FOV. Another parameter to explore is the angle between the camera heads. Decreasing the angle between the boxes reduces the source-aperture distance, which would increase sensitivity and spatial resolution, but also increase the multiplexing on the front detector if the FOV was unchanged. The multiplexing could be addressed by using greater inter-pinhole distance for the apertures.

Heather Durko at the University of Arizona is building a high-resolution, adaptable slit-slat collimator for the DSSDs. She is also exploring the use of a coded aperture imaging configuration. Her basic question is how to best make use of the space-bandwidth product of the detectors. The parameter space she is exploring is quite large. With the coded apertures the count-rate on the detectors would be higher, so dealing with the artifacts would be important. It would be interesting to

see if the stacked detector configuration offers any benefit to a coded aperture imager since the levels of multiplexing would be very high on both detectors. By simply swapping apertures, SiliSPECT could be made into a high-resolution stem-cell imager (coded apertures only work well for concentrated sources with low background), for instance. Most cells are radiolabeled with ^{111}In or ^{99m}Tc, which would require a thicker aperture, possibly limiting the spatial resolution.

The uniformity could possibly be further improved by adapting the iterative trim algorithm to adjust based on the gain as well as the offset. Currently only the threshold floor value (offset) is used. Another method that might be better is based on repeatedly measuring the flood singles histograms with a tungsten plate on the stages acting like a shutter. The flood data would be taken, the singles data histogrammed, and the trims would be adjusted based on the histograms. Then the shutter would block the source and the global threshold would be set to just above where noise triggers become significant. Egregiously noisy channels would be disabled as before. Then new flood data would be acquired, and the proces would repeat. The advantage with this method is that 1) it may actually be faster, and 2) it would account for both gain and offset variations for a given energy.

7.1.1 Extension to high-energy gamma-ray emitters

Early on we investigated the concept of stacking detectors for simultaneously imaging the low- and high-energy components of isotopes such as ^{123}I using a DSSD with a modular gamma-camera (modcam) stacked behind it [47]. One configuration of this concept is illustrated in Fig. 7.1. With this approach the low-energy photons are

absorbed by the front detector, but the higher-energy photons mostly pass through to interact in the denser, higher-Z back detector. As a impetus for future work, a summary of this earlier work is given. Fig. 7.1 shows a configuration for this concept. With the large pinholes, the resolution on the two detectors ends up being quite similar. Some basic simulations evaluating one detector's impact upon the other in terms of scatter and attenuation were performed. We used GATE [128] to simulate the system matrix for each detector and to generate projection images. For example, Fig. 7.2 shows simulated projection images from a ^{123}I point source, where 15.2 % of the incident photons are detected in the front detector and 25.2 % are detected in the back detector. Only a few percent of the incident photons scatter in one detector and then deposit energy in the other detector. The data on the right side of Fig. 7.1 shows some of the results, such as the intrinsic efficiency for different energies and the efficiency for incident ^{123}I photons (bottom right).

We generated 2561-element point spread functions (PSFs) consisting of a 17x17x13 cubic grid within a cylinder with 0.45 mm isotropic voxels for each detector. Computing one PSF element with roughly 5×10^4 counts took 10 min on a dual processor x86 2.0 GHz Xeon machine. Batch jobs of GATE [128], a Geant4 interface code for emission tomography, were run on Vanderbilts computing cluster (ACCRE) to get a linear speedup. Projections from 3.6 mm long, 1.8 mm diameter rod objects placed 3.3 mm apart (e.g., Fig 7.4) were simulated for 30 angles. Each projection contained on average 3×10^4 counts. The Ordered-Subsets Expectation Maximization (OSEM) iterative algorithm was used to reconstruct images using the simulated PSF. An iterative reconstruction algorithm is essential for the synthetic collimator method, so the

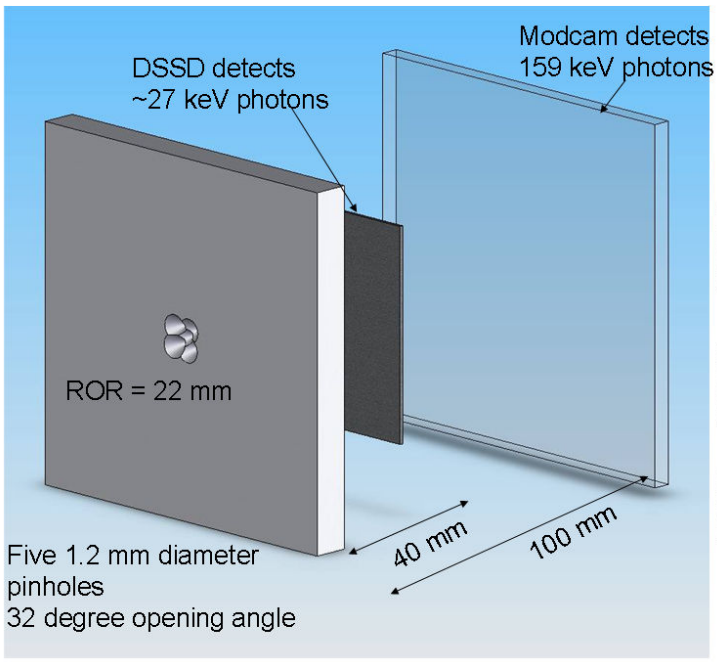

Energy (keV)	DSSD	Modcam
30	30 %	~90 %
159	5 %	60 %
529	~0 %	5 %

DSSD intrinsic resolution (mm)	Modcam intrinsic resolution (mm)
0.06	2.5

DSSD planar resolution (mm)	Modcam intrinsic resolution (mm)
1.9	1.6

DSSD	Modcam
27.5 ± 6 keV	159 ± 24 keV

	DSSD	Modcam
Detected	15.0 %	24.9 %
Scattered	0.2 %	1.6 %

Figure 7.1: Schematic drawing of the dual-energy, single-isotope stacked detector system (left). Simulated data pertinent to the system is shown on the right. The bottom right shows the total incident radiation detected in each detector and the percentage of events that undergo cross-detector scatter before depositing in the other detector's energy window.

non-multiplexed data is used in conjunction with the multiplexed, higher-resolution data. Reconstructed images with the Modcam alone, DSSD alone, and the stacked configuration were generated from the simulated projections. The DSSD reconstruction was used as the starting point for reconstructing the multiplexed Modcam data. A measure of the fidelity of the reconstructed object is found via the normalized mean square error (NMSE):

$$\text{NMSE} = \frac{1}{N} \sum_i \frac{(O_i - E_i)^2}{\overline{O}\ \overline{E}} \tag{7.1}$$

where N is the number of voxels, O is the actual voxel value, and E is the estimated voxel value. $\overline{O}$ and $\overline{E}$ are the mean values.

Using the non-multiplexed DSSD data as an input to the modcam OSEM recon-

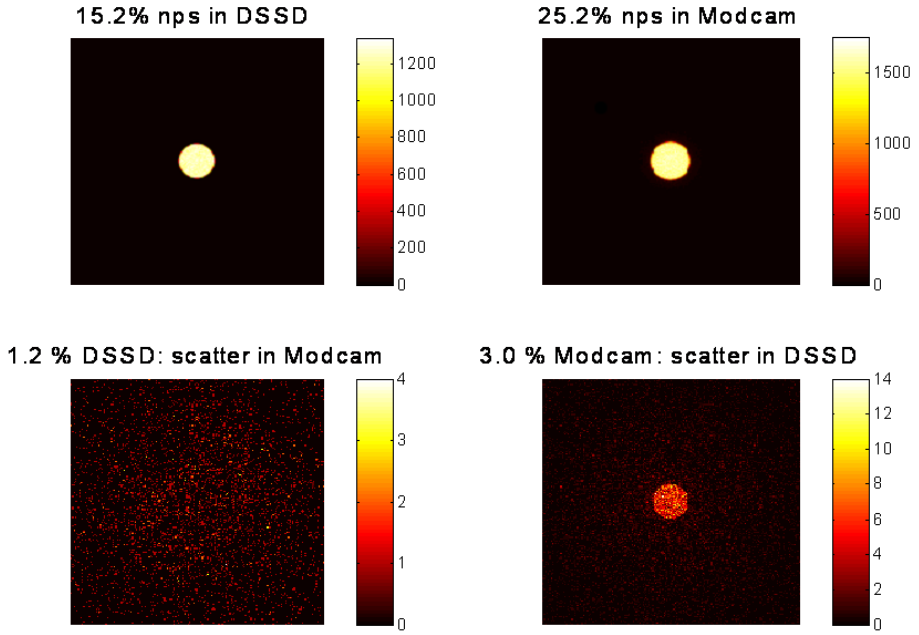

Figure 7.2: Simulated PSFs on the DSSD from photons that pass through the aperture without scatter (top left) and those that scatter in the Modcam and then interact in the DSSD (bottom left), and vice-versa for the right figures. Percentages are given as the total number of particles used in the simulation (nps), which were all incident upon the detector through the pinhole. Modcam window: 15 % at 159 keV, DSSD window: 22 % at 27 keV. Less total cross-detector scattering occurs when DSSD is farther from Modcam.

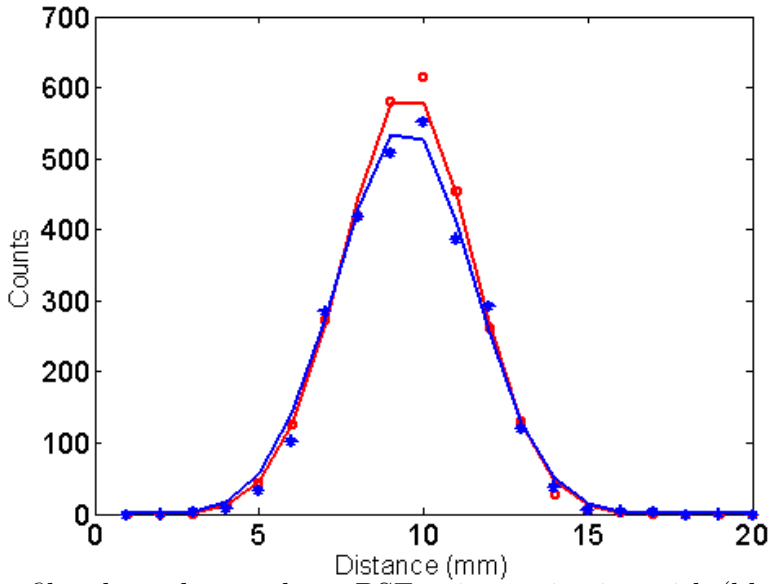

Figure 7.3: Profiles through a modcam PSF point projection with (blue) and without (red) the DSSD. The DSSD attenuates roughly 9 % of the counts normally in the modcam, but doesn't change the width or the tails of the PSF.

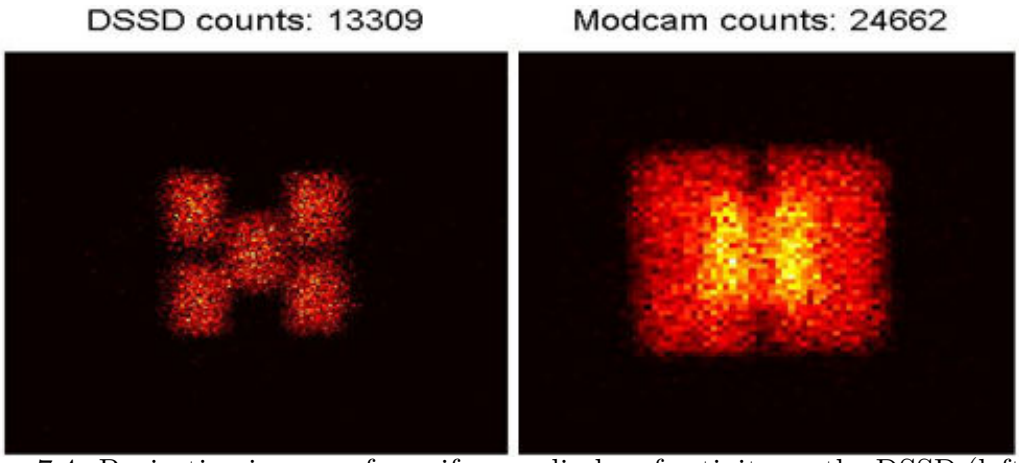

Figure 7.4: Projection images of a uniform cylinder of activity on the DSSD (left) and modcam (right). High levels of multiplexing are evident in the modcam projection, but the DSSD projections are distinct.

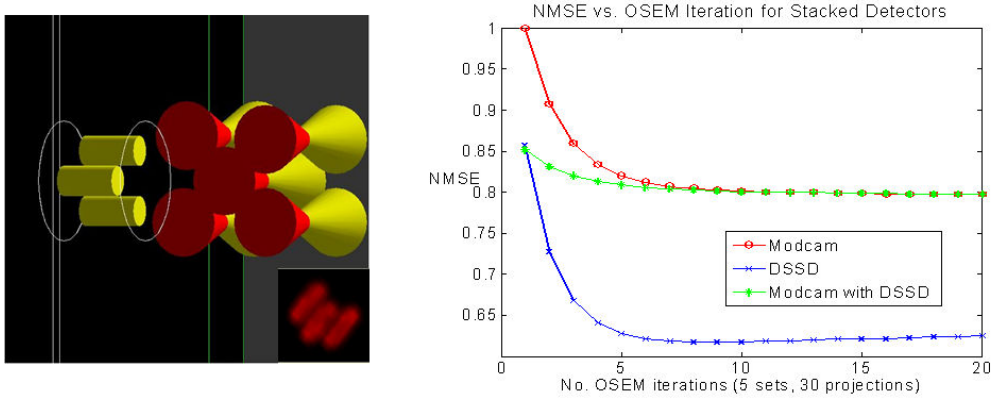

Figure 7.5: Three 1.8mm diameter, 3.6 mm long line objects placed 3.3mm apart in GATE (left, inset shows rendering of reconstructed object), and NMSE vs. OSEM iteration (right).

struction reduced the NMSE for the first nine iterations (Fig. 7.5). The DSSD NMSE is likely much lower than the that of the modcam because the higher multiplexing in the modcam projections skews accurate determination of the activity in the voxels. Concatenating the projections from each detector in a large OSEM reconstruction might reduce the NMSE of the modcam at all iteration values. We learned that the initial guess for MLEM-based algorithms does not matter if the iterations are allowed to reach convergence, although it speeds up the convergence.

We implemented a batch cluster tool with GATE to simulate complex imaging systems. Combined with Gaussian interpolation code, these tools will allow us to simulate larger, realistic systems in reasonable computing time. Stacked detectors with multi-pinhole apertures present a novel way to boost sensitivity and limit reconstructions artifacts from multiplexing. Besides increasing sensitivity through multiplexing of the high-energy data, this approach also increases sensitivity by inclusion of the low-energy data. We anticipate that the DSSD data will be more beneficial for higher amounts of multiplexing on the modcam.

The area and spatial resolution of the modcam limited its use in the stacked detector geometry. A higher-resolution detector would have better performance and permit more imaging options. The detector could be placed at lower magnification so there would be less multiplexing. A high-purity germanium DSSD will take the place of the modcam in a future system. The plan is to use a single Si DSSD with a Ge DSSD stacked behind it with both detectors affixed to the gantry of the microCT machine. This will be a good demonstration of a fully semiconductor detector system.

The unbonded silicon detectors could be connected to a new readout system with

faster triggering circuitry or custom boards. If the timing and energy resolution were good enough with the Si DSSD, the stacked Si & Ge detectors could also work in Compton mode. In an even grander vision, custom-size boards with flexible readout cables could be designed with magnetic-free components to allow operation in an MRI bore. The overall size, resolution, and detection physics make DSSDs a great, untapped candidate for the basis of a SPECT/MRI imager.

APPENDIX A

APPENDIX A: SYSTEM OPERATING INSTRUCTIONS

A.1 Overview of system startup and power down

When the power supply is switched on or off, the HV knobs should be turned completely counter-clockwise, or set at zero volts. The preamplifiers in the ASICs must be turned on before applying the HV. Otherwise, the gate oxide of the input transistors may be damaged. The HV should also be turned down so it is less than 1 V before shutting off the power supply. The HV bias can be measured with a voltmeter at the terminals at the front of the digital isolator boxes. If nothing happens when the power toggle is switched, try pressing the relay button.

In the case of loss of power, we wired in a relay switch into the power supply circuit so the power would stay off after such an event. Turning the system off without lowering the high voltage is not the safest procedure, but applying the high voltage when the chips are not initialized with proper DAC settings can be disastrous, according to the Ideas documentation.

Startup sequence

1. Make sure the high voltage is off. (dials turned fully ccw).
2. Turn on the cooling fans and make sure there are no light leaks.
3. Switch on the power supply.
4. Download the DAC values for both sides.
5. Download ASIC masks for both sides.
6. Turn high voltage on (turn one dial so the voltage reaches 150 V, then turn the other dial until the voltage reaches 300 V). Dials fully turned will give a

potential of -200 V to 200 V (400 V across the detector).

7. Download the FPGA (ADC board) masks for both sides.

Power down sequence

1. Turn high voltage off (dials turned fully CCW).
2. Switch off the power supply after the voltage hovers around 0.4-0.5 V. It takes several minutes to ramp down from 300 V.
3. Turn off cooling fan.

A.2 Labview graphical user interface

The main window for the SiliSPECT control interface is shown in Fig. A.1. From here the user can download ASIC, FGPA, and DAC masks, as well as look at real time burst-mode or coincidence data. The pedestals can be recorded, and data can be acquired in a single- or multi-file mode. Data can also be acquired with simple linear or rotation stage step/shoot movements.

The DAC interface is displayed in Fig. A.2 and the real-time coincidence sorter in Fig. A.3.

A.3 Steps for restoring trigger uniformity and detector function

1. Download the last ASIC mask and DAC values that produced good trigger uniformity.

2. Disable all but one detector side with the front panel buttons and click "update FGPA mask."

3. Place a source roughly 30 cm from the detector with the aperture removed.

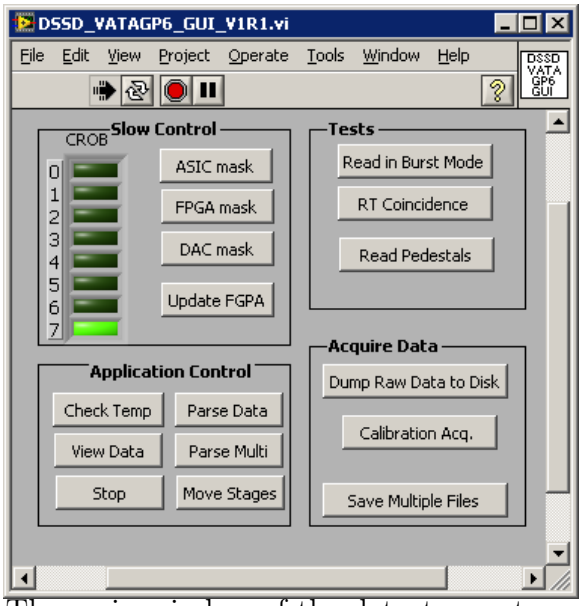

Figure A.1: The main window of the detector system user interface.

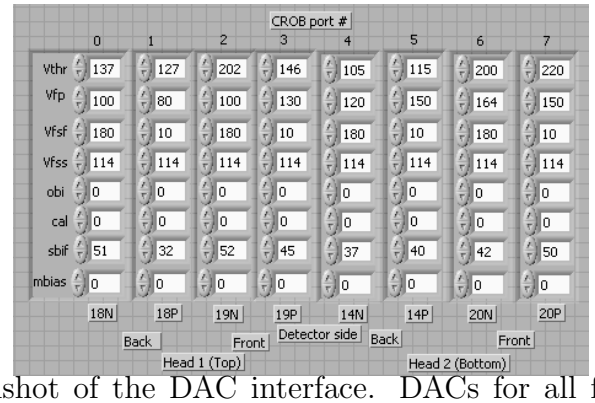

Figure A.2: Screenshot of the DAC interface. DACs for all four detectors can be adjusted, saved, and loaded from this window.

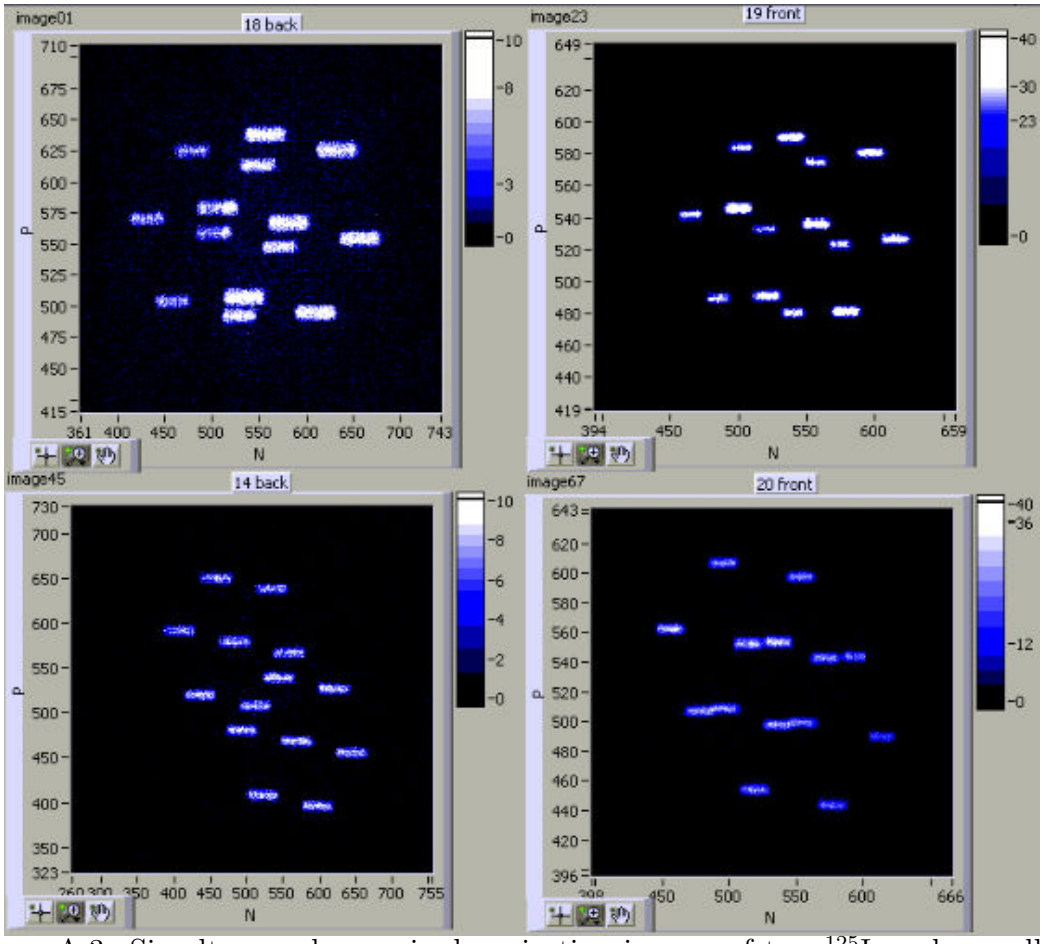

Figure A.3: Simultaneously-acquired projection images of two ^{125}I seeds on all four detectors using 7 pinholes on each camera. Real-time coincidence sorting permits object centering in the ∼2 cm diameter quasi-spherical FOV.

4. Look at the burst-mode data. If the detector is triggering on noise at high rates, first turn off the plotting, as this bogs down the whole program at high counting rates. Then try increasing the Vth DAC (Decrease on the N-side) until the hot strips (usually it is just a few) stop triggering. The background counting rate from all the other channels should be low and uniform (no more than 25 Hz for all the channels).

5. If adjusting Vth has no effect, make sure the noisy channel(s) are disabled in the ASIC mask. In certain cases the channels may also need to have the input drain enabled.

6. If the noisy channels are disabled but the uniformity is still poor (e.g., one chip triggering more than the others), try increasing Sbif and lowering Vfp. Altering Sbif changes the gain on the fast amp, so the threshold will shift and Vth must be adjusted accordingly.

7. Look at the real time pedestal readout. Do certain channels have much wider pedestal widths (as measured by the sdevs)? If so, these channels may need to be disabled, also. The pedestal values are very sensitive to the DAC values, though, so try varying the DACs while the pedestals are being read out.

8. Check that the temperature in the boxes is around 93° Fand that the lab temperature is normal.

A.4 Some things learned by accident

- Forward-biasing the detectors (hooking up positive voltage on P side) does not destroy anything.
- Starting the system with the CROB cables unconnected to the digital isolators does not destroy anything.
- Hot-swapping the CROB cables did not destroy anything, but required restarting the digital isolators and CROB.
- Making wrong connections with the cables in the CROB will give very confusing results. We had the P cables switched for two detectors, and we were able to get decent slit shadow images, but flood acquisitions did not sort right at all.
- Plugging the detector/chip power supply cable by one pin off does cause damage. Several filtering capacitors and possibly other components were destroyed on the N side of detector 14 when this happened due to poor visibility of the connector. We modified the board holders after this so we could see the connections better.
- Measuring the HV bias with a voltmeter affects the operating voltages of the ASICs: removing or replacing the probe leads on the digital isolators will change the triggering rates on the detectors.

REFERENCES

[1] G. Hevesy. The absorption and translocation of lead by plants. *Biochem. J*, 17(4-5):439–445, 1923.

[2] O. Chiewitz and G. Hevesy. Radioactive indicators in the study of phosphorus metabolism in rats. *Nature*, 136:754–755, 1935.

[3] Proceedings of the 26th Annual Meeting. *J Nucl Med*, 20(6):590–698, 1979.

[4] B. Cassen, L. Curtis, C. Reed, and R. Libby. Instrumentation for 131i use in medical studies. *Nucleonics*, 9(2):46, 1951.

[5] H. O. Anger. Use of a gamma-ray camera for in vivo studies (1952): Article in nature. *Nature*, 170:200–201, 1952.

[6] R. J. Jaszczak. The early years of single photon emission computed tomography (SPECT): an anthology of selected reminiscences. *Physics in Medicine and Biology*, 51(13):99, 2006.

[7] E. Williams Lawrence. Anniversary paper: Nuclear medicine: Fifty years and still counting. *Medical Physics*, 35(7):3020–3029, 2008.

[8] S. Carlson. A glance at the history of nuclear medicine. *Acta Oncologica*, 34(8):1095–1102, 1995.

[9] R. J. Jaszczak, R. E. Coleman, and C. B. Lim. SPECT - single photon-emission computed-tomography. *IEEE Transactions on Nuclear Science*, 27(3):1137–1153, 1980.

[10] H. H. Barrett. Detectors for small-animal SPECT. In *Workshop for Small-Animal SPECT*, University of Arizona, Tucson, 2006. Springer Verlag.

[11] T. F. Budinger and G. T. Gullberg. Three-dimensional reconstruction in nuclear medicine emission imaging. *IEEE Transactions on Nuclear Science*, 21(3):2–20, 1974.

[12] L. A. Shepp and Y. Vardi. Maximum likelihood reconstruction for emission tomography. *IEEE Transactions on Medical Imaging*, MI-1(2):113–122, 1982.

[13] H. M. Hudson and R. S. Larkin. Accelerated image reconstruction using ordered subsets of projection data. *IEEE Transactions on Medical Imaging*, 13(4):601–609, 1994.

[14] B. H. Hasegawa, K. Iwata, K. H. Wong, M. C. Wu, A. J. Da Silva, H. R. Tang, W. C. Barber, A. H. Hwang, and A. E. Sakdinawat. Dual-modality imaging of function and physiology. *Academic radiology*, 9(11):1305–1321, 2002.

[15] S. R. Meikle, P. Kench, M. Kassiou, and R. B. Banati. Small animal SPECT and its place in the matrix of molecular imaging technologies. *Physics in Medicine and Biology*, 50(22):R45–61, 2005.

[16] P. D. Acton and H. F. Kung. Small animal imaging with high resolution single photon emission tomography. *Nuclear Medicine and Biology*, 30(8):889–95, 2003.

[17] B. L. Franc, P. D. Acton, C. Mari, and B. H. Hasegawa. Small-animal SPECT and SPECT/CT: Important tools for preclinical investigation. *Journal of Nuclear Medicine*, 49(10):1651, 2008.

[18] Sushil Sharma and Manuchair Ebadi. SPECT neuroimaging in translational research of cns disorders. *Neurochemistry International*, 52(3):352–362, 2008.

[19] S. Shokouhi, D.W. Wilson, W. Pham, and T.E. Peterson. System evaluation for in vivo imaging of amyloid beta plaques in a mouse brain using statistical decision theory. In *Nuclear Science Symposium Conference Record*, volume 6, 2007.

[20] Dinggang Shen, Dengfeng Liu, Zixiong Cao, Paul Acton, and Rong Zhou. Coregistration of magnetic resonance and single photon emission computed tomography images for noninvasive localization of stem cells grafted in the infarcted rat myocardium. *Molecular Imaging and Biology*, 9(1):24–31, 2007.

[21] G. Muehllehner. Effect of resolution improvement on required count density in ect imaging - a computer-simulation. *Physics in Medicine and Biology*, 30(2):163–173, 1985.

[22] Douglas J. Rowland and Simon R. Cherry. Small-animal preclinical nuclear medicine instrumentation and methodology. *Seminars in Nuclear Medicine*, 38(3):209–222, 2008.

[23] F. J. Beekman and F. van der Have. The pinhole: gateway to ultra-high-resolution three-dimensional radionuclide imaging. *European Journal of Nuclear Medicine and Molecular Imaging*, 2006.

[24] S. R. Cherry. In vivo molecular and genomic imaging: new challenges for imaging physics. *Physics in Medicine and Biology*, 49(3):R13–R48, 2004.

[25] H. R. Herschman. Molecular imaging: Looking at problems, seeing solutions. *Science*, 302(5645):605–608, 2003.

[26] A. F. Chatziioannou. Instrumentation for molecular imaging in preclinical research: Micro-PET and micro-SPECT. *Proceedings of the American Thoracic Society*, 2(6):533–6, 510–11, 2005.

[27] M. Rudin and R. Weissleder. Molecular imaging in drug discovery and development. *Nature Reviews Drug Discovery*, 2(2):123–131, 2003.

[28] M. A. Kupinski and H. H. Barrett. *Small-Animal SPECT Imaging*. Springer Science+Business Media, Inc., 2005.

[29] S. P. Hume, R. N. Gunn, and T. Jones. Pharmacological constraints associated with positron emission tomographic scanning of small laboratory animals. *European Journal of Nuclear Medicine*, 25(2):173–176, 1998.

[30] M. V. Green, J. Seidel, J. J. Vaquero, E. Lagoda, I. Lee, and W. C. Eckelman. High resolution PET, SPECT and projection imaging in small animals. *Computerized Medical Imaging and Graphics*, 25(2):79–86, 2001.

[31] Simon R. Cherry. The 2006 henry n. wagner lecture: Of mice and men (and positrons)–advances in PET imaging technology. *Journal of Nuclear Medicine*, 47(11):1735–1745, 2006.

[32] H. N. Wagner Jr. Highlights 2002 lecture: Reinventing clinical nuclear medicine. *Journal of Nuclear Medicine*, 43(8), 2002.

[33] Paul D. Acton. Animal imaging equipment: Recent advances. *Journal of Nuclear Medicine*, 47(12):52N–55, 2006.

[34] Steven R. Meikle, Freek J. Beekman, and Stephen E. Rose. Complementary molecular imaging technologies: High resolution SPECT, PET and mri. *Drug Discovery Today: Technologies*, 3(2):187–194, 2006.

[35] T.E. Peterson, S. Shokouhi, L.R. Furenlid, and D.W. Wilson. Multi-pinhole SPECT imaging with silicon strip detectors. *Nuclear Science, IEEE Transactions on*, 56(3):646–652, June 2009.

[36] M. M. Rogulski, H. B. Barber, H. H. Barrett, R. L. Shoemaker, and J. M. Woolfenden. Ultra-high-resolution brain SPECT imaging - simulation results. *IEEE Transactions on Nuclear Science*, 40(4):1123–1129, 1993.

[37] F. J. Beekman, F. van der Have, B. Vastenhouw, A. J. A. van der Linden, P. P. van Rijk, J. P. H. Burbach, and M. P. Smidt. U-SPECT-I: A novel system for submillimeter-resolution tomography with radiolabeled molecules in mice. *Journal of Nuclear Medicine*, 46(7):1194–1200, 2005.

[38] F. van der Have, B. Vastenhouw, R.M. Ramakers, W. Branderhorst, J.O. Krah, C. Ji, S.G. Staelens, and F.J. Beekman. U-SPECT-II: An ultra-high-resolution device for molecular small-animal imaging. *Journal of Nuclear Medicine*, 50(4):599, 2009.

[39] N. U. Schramm, G. Ebel, U. Engeland, T. Schurrat, M. Behe, and T. M. Behr. High-resolution SPECT using multipinhole collimation. *IEEE Transactions on Nuclear Science*, 50(3):315–320, 2003.

[40] Jacob Y. Hesterman, Matthew A. Kupinski, Lars R. Furenlid, Donald W. Wilson, and Harrison H. Barrett. The multi-module, multi-resolution system (M3R): A novel small-animal SPECT system. *Medical Physics*, 34(3):987–993, 2007.

[41] K. Vunckx, P. Suetens, and J. Nuyts. Effect of overlapping projections on reconstruction image quality in multipinhole SPECT. *IEEE Transactions on Medical Imaging*, 27(7):972–983, 2008.

[42] J. Nuyts, K. Vunckx, M. Defrise, and C. Vanhove. Small animal imaging with multi-pinhole SPECT. *Methods*, 48(2):83–91, 2009.

[43] D. W. Wilson, H. H. Barrett, and E. W. Clarkson. Reconstruction of two- and three-dimensional images from synthetic-collimator data. *IEEE Transactions on Medical Imaging*, 19(5):412–422, 2000.

[44] Jacob Y. Hesterman, Matthew A. Kupinski, Eric Clarkson, and Harrison H. Barrett. Hardware assessment using the multi-module, multi-resolution system (M3R): A signal-detection study. *Medical Physics*, 34(7):3034–3044, 2007.

[45] C. Lackas, N. U. Schramm, J. W. Hoppin, U. Engeland, A. Wirrwar, and H. Halling. T-SPECT: A novel imaging technique for small animal research. *IEEE Transactions on Nuclear Science*, 52(1):181–187, 2005.

[46] T. E. Peterson, S. Shokouhi, L. R. Furenlid, and D. W. Wilson. Multi-pinhole SPECT imaging with silicon strip detectors. *Nuclear Science, IEEE Transactions on*, 56(3):646–652, 2009.

[47] B. S. McDonald, S. Shokouhi, H. H. Barrett, and T. E. Peterson. Multi-energy, single-isotope pinhole imaging using stacked detectors. In *IEEE Nuclear Science Symposium and Medical Imaging Conference*, San Diego, CA, 2006.

[48] T. E. Peterson, D. W. Wilson, and H. H. Barrett. Application of silicon strip detectors to small-animal imaging. *Nuclear Instruments & Methods in Physics Research Section A*, 505(1-2):608–611, 2003.

[49] T. E. Peterson, D. W. Wilson, and H. H. Barrett. A prototype low-energy, multi-pinhole SPECT system for small-animal imaging. In *IEEE Nuclear Science Symposium and Medical Imaging Conference*, volume 5, pages 2999–3002 Vol. 5, 2004.

[50] W. S. Choong, W. W. Moses, C. S. Tindall, and P. N. Luke. Design for a high-resolution small-animal SPECT system using pixellated si(li) detectors for in vivo i-125 imaging. *IEEE Transactions on Nuclear Science*, 52(1):174–180, 2005.

[51] H. Kim, L. R. Furenlid, M. J. Crawford, D. W. Wilson, H. B. Barber, T. E. Peterson, W. C. J. Hunter, Z. L. Liu, J. M. Woolfenden, and H. H. Barrett. SemiSPECT: A small-animal single-photon emission computed tomography (SPECT)

imager based on eight cadmium zinc telluride (czt) detector arrays. *Medical Physics*, 33(2):465–474, 2006.

[52] L. R. Furenlid, D. W. Wilson, Y. C. Chen, H. Kim, P. J. Pietraski, M. J. Crawford, and H. H. Barrett. FastSPECT II: A second-generation high-resolution dynamic SPECT imager. *IEEE Transactions on Nuclear Science*, 51(3):631–635, 2004.

[53] E. L. Bradley, J. Cella, S. Majewski, V. Popov, J. G. Qian, M. S. Saha, M. F. Smith, and A. G. Weisenberger. A compact gamma camera for biological imaging. *IEEE Transactions on Nuclear Science*, 53(1):59–65, 2006.

[54] L. J. Meng. An intensified EMCCD camera for low energy gamma ray imaging applications. *IEEE Transactions on Nuclear Science*, 53(4):2376–2384, 2006.

[55] Brian W. Miller, Harrison H. Barrett, Lars R. Furenlid, H. Bradford Barber, and Robert J. Hunter. Recent advances in BazookaSPECT: Real-time data processing and the development of a gamma-ray microscope. *Nuclear Instruments & Methods in Physics Research Section A*, 591(1):272–275, 2008.

[56] T. C. Soesbe, M. A. Lewis, E. Richer, N. V. Slavine, and P. P. Antich. Development and evaluation of an EMCCD based gamma camera for preclinical SPECT imaging. *IEEE Transactions on Nuclear Science*, 54(5 Part 1):1516–1524, 2007.

[57] G. A. de Vree, A. H. Westra, I. Moody, F. van der Have, K. M. Ligtvoet, and F. J. Beekman. Photon-counting gamma camera based on an electron-multiplying CCD. *IEEE Transactions on Nuclear Science*, 52(3):580–588, 2005.

[58] F. J. Beekman, D. P. McElroy, F. Berger, S. S. Gambhir, E. J. Hoffman, and S. R. Cherry. Towards in vivo nuclear microscopy: iodine-125 imaging in mice using micro-pinholes. *European Journal of Nuclear Medicine and Molecular Imaging*, 29(7):933–938, 2002.

[59] Frans van der Have, Brendan Vastenhouw, and Frederik Beekman. U-SPECT-II: A versatile sub-half-mm resolution small animal SPECT system. *Society of Nuclear Medicine Meeting*, 48(2):47P–b–, 2007.

[60] Tobias Funk, Philippe Despres, William C. Barber, Kanai S. Shah, and Bruce H. Hasegawa. A multipinhole small animal SPECT system with submillimeter spatial resolution. *Medical Physics*, 33(5):1259–1268, 2006.

[61] G. A. Kastis, L. R. Furenlid, D. W. Wilson, T. E. Peterson, H. B. Barber, and H. H. Barrett. Compact CT/SPECT small-animal imaging system. *IEEE Transactions on Nuclear Science*, 51(1):63–67, 2004.

[62] L. R. MacDonald, B. E. Patt, J. S. Iwanczyk, B. M. W. Tsui, Y. C. Wang, E. C. Frey, D. E. Wessell, P. D. Acton, and H. F. Kung. Pinhole SPECT of mice using the lumagem gamma camera. *IEEE Transactions on Nuclear Science*, 48(3):830–836, 2001.

[63] T. Zeniya, H. Watabe, T. Aoi, K. M. Kim, N. Teramoto, T. Takeno, Y. Ohta, T. Hayashi, H. Mashino, and T. Ota. Use of a compact pixellated gamma camera for small animal pinhole SPECT imaging. *Annals of Nuclear Medicine*, 2006:409–16, 2006.

[64] Jacob Y. Hesterman. The multi-module, multi-resolution spect system: a tool for variable-pinhole small-animal imaging, 2006.

[65] GK Kastis, HB Barber, HH Barrett, HC Gifford, IW Pang, DD Patton, JD Sain, G. Stevenson, and DW Wilson. High resolution SPECT imager for three-dimensional imaging of small animals. *J. Nucl. Med (supplement)*, 39(9), 1998.

[66] SR Meikle, P. Kench, R. Wojcik, MF Smith, AG Weisenberger, S. Majewski, M. Lerch, and AB Rosenfeld. Performance evaluation of a multipinhole small animal SPECT system. In *IEEE Nuclear Science Symposium Conference Record*, volume 3, 2003.

[67] SC Moore, RE Zimmerman, A. Mahmood, R. Mellen, and CB Lim. A triple-detector, multiple-pinhole system for SPECT imaging of rodents. *J. Nucl. Med*, 45:97, 2004.

[68] RE Zimmerman, SC Moore, and A. Mahmood. Performance of a triple-detector, multiple-pinhole SPECT system with iodine and indium isotopes. In *Nuclear Science Symposium Conference Record*, volume 4, 2004.

[69] A. G. Weisenberger, S. S. Gleason, J. Goddard, B. Kross, S. Majewski, S. R. Meikle, M. J. Paulus, M. Pomper, V. Popov, M. F. Smith, B. L. Welch, and R. Wojcik. A restraint-free small animal SPECT imaging system with motion tracking. *IEEE Transactions on Nuclear Science*, 52(3):638–644, 2005.

[70] A. L. Goertzen, D. W. Jones, J. Seidel, K. Li, and M. V. Green. First results from the high-resolution mouseSPECT annular scintillation camera. *IEEE Transactions on Medical Imaging*, 24(7):863–867, 2005.

[71] N. Schramm, J. Hoppin, C. Lackas, F. Forrer, R. Valkema, and M. de Jong. The NanoSPECT: A high-sensitivity multi-pinhole SPECT system with submillimeter (nanoliter) spatial resolution for imaging small rodents, 2006. details at www.bioscan.com.

[72] R. Accorsi, M. Autiero, L. Celentano, M. Chmeissani, R. Cozzolino, A.S. Curion, P. Frallicciardi, P. Laccetti, RC Lanza, A. Lauria, et al. MediSPECT: Single photon emission computed tomography system for small field of view small animal imaging based on a CdTe hybrid pixel detector. *Nuclear Inst. and Methods in Physics Research, A*, 571(1-2):44–47, 2007.

[73] A. Del Guerra and N. Belcari. State-of-the-art of PET, SPECT and CT for small animal imaging. *Nuclear Inst. and Methods in Physics Research, A*, 583(1):119–124, 2007. www.gm-ideas.com.

[74] R. Accorsi. 20-m resolution imaging of soft x-ray emitters. *IEEE Transactions on Nuclear Science*, 55(3):889, 2008.

[75] Y. Zingerman, H. Golan, A. Gersten, and A. Moalem. A compact CT/SPECT system for small-object imaging. *Nuclear Instruments & Methods in Physics Research Section A*, 584(1):135–148, 2008.

[76] Jianguo Qian, Eric L. Bradley, Stan Majewski, Vladimir Popov, Margaret S. Saha, Mark F. Smith, Andrew G. Weisenberger, and Robert E. Welsh. A small-animal imaging system capable of multipinhole circular/helical spect and parallel-hole spect. *Nuclear Instruments and Methods in Physics Research Section A: Accelerators, Spectrometers, Detectors and Associated Equipment*, 594(1):102 – 110, 2008.

[77] B. W. Miller, H. B. Barber, H. H. Barrett, D. W. Wilson, and L. Chen. A low-cost approach to high-resolution single-photon imaging using columnar scintillators and image intensifiers, 2006.

[78] S. Shokouhi, SD Metzler, DW Wilson, and TE Peterson. Multi-pinhole collimator design for small-object imaging with SiliSPECT: a high-resolution SPECT. *Physics in Medicine and Biology*, 54(2):207–225, 2009.

[79] S. Shokouhi, M.A. Fritz, B.S. McDonald, H.L. Durko, L.R. Furenlid, D.W. Wilson, and T.E. Peterson. A silicon SPECT system for molecular imaging of the mouse brain. In *Nuclear Science Symposium Conference Record*, volume 4, 2007.

[80] S. Shokouhi, MA Fritz, BS McDonald, DW Wilson, SD Metzler, and TE Peterson. Design of a Multi-Pinhole Collimator in a Dual-Headed, Stationary, Small-Animal SPECT. In *Nuclear Science Symposium Conference Record*, volume 4, 2006.

[81] L.J. Meng, G. Fu, E.J. Roy, B. Suppe, and C.T. Chen. An ultrahigh resolution SPECT system for i-125 mouse brain imaging studies. *Nuclear Instruments and Methods in Physics Research Section A: Accelerators, Spectrometers, Detectors and Associated Equipment*, 600(2):498 – 505, 2009.

[82] L. J. Meng, D. Li, S. Cho, C. Pelizzari, J. Souris, X. Pan, and C. T. Chen. Preliminary imaging performance of an ultra-high resolution pinhole SPECT systems using an intensified EMCCD camera. In *IEEE Nuclear Science Symposium and Medical Imaging Conference*, San Diego, CA, 2006.

[83] L. J. Meng and G. Fu. Investigation of the intrinsic spatial resolution of an intensified EMCCD scintillation camera. *IEEE Transactions on Nuclear Science*, 55(5 Part 1):2508–2517, 2008.

[84] T.T. Shinichiro Takeda, S. Watanabe, H. Tajima, T. Tanaka, K. Nakazawa, Y. Fukazawa, J. Sagamihara, CA Stanford, and J. Higashi-Hiroshima.

Double-sided silicon strip detector for x-ray imaging, March 2010. http://spie.org/x20060.xml?ArticleID=x20060.

[85] GJ Royle, A. Papanestis, RD Speller, G. Hall, G. Iles, M. Raymond, E. Corrin, PF Van der Stelt, N. Manthos, and FA Triantis. Development of a 2D silicon strip detector system for mammographic imaging using particle physics technology. *Nuclear Inst. and Methods in Physics Research, A*, 493(3):176–188, 2002.

[86] J. H. D. Wong, M. Carolan, M. L. F. Lerch, M. Petasecca, S. Khanna, V. L. Perevertaylo, P. Metcalfe, and A. B. Rosenfeld. A silicon strip detector dose magnifying glass for imrt dosimetry. *Medical Physics*, 37(2):427–439, 2010.

[87] N. Cesca, N. Auricchio, G. Di Domenico, G. Zavattini, R. Malaguti, R. Andritschke, G. Kanbach, and F. Schopper. SiliPET: design of an ultra-high resolution small animal PET scanner based on stacks of semi-conductor detectors. *Nuclear Inst. and Methods in Physics Research, A*, 572(1):225–227, 2007.

[88] GS Mitchell, S. Sinha, JR Stickel, SL Bowen, LJ Cirignano, P. Dokhale, H. Kim, KS Shah, and SR Cherry. CdTe Strip Detector Characterization for High Resolution Small Animal PET. *IEEE Transactions on Nuclear Science*, 55(3 Part 1):870–876, 2008.

[89] C. Fiorini, A. Gola, A. Longoni, M. Zanchi, A. Restelli, F. Perotti, P. Lechner, H. Soltau, and L. Str
"uder. A large-area monolithic array of silicon drift detectors for medical imaging. *Nuclear Inst. and Methods in Physics Research, A*, 568(1):96–100, 2006.

[90] HC Boston, J. Gillam, AJ Boston, RJ Cooper, J. Cresswell, AN Grint, AR Mather, PJ Nolan, DP Scraggs, G. Turk, et al. Orthogonal strip HPGe planar SmartPET detectors in Compton configuration. *Nuclear Inst. and Methods in Physics Research, A*, 580(2):929–933, 2007.

[91] E. A. Wulf, B. F. Phlips, J. D. Kurfess, K. D. Hobart, F. J. Kub, and M. Tadjer. Wafter-bonded silicon gamma-ray detectors. In *IEEE Nuclear Science Symposium and Medical Imaging Conference*, San Diego, CA, 2006.

[92] Z. Li, W. Chen, Y.H. Guo, D. Lissauer, D. Lynn, V. Radeka, and G. Pellegrini. Development, simulation and processing of new 3d si detectors. *Nuclear Instruments and Methods in Physics Research Section A: Accelerators, Spectrometers, Detectors and Associated Equipment*, 583(1):139 – 148, 2007. Proceedings of the 6th International Conference on Radiation Effects on Semiconductor Materials, Detectors and Devices - RESMDD 2006.

[93] SINTEF ICT Microsystems and Nanotechnology. www.sintef.no/Home.

[94] D. M. Pettersen, S. Mikkelsen, J. Talebi, D. Meier, I. Asa, and N. Fornebu. A readout asic for SPECT. *IEEE Transactions on Nuclear Science*, 52(3 Part 2):764–771, 2005.

[95] S. Shokouhi, HL Durko, MA Fritz, LR Furenlid, and TE Peterson. Thick Silicon Strip Detectors for Small-Animal SPECT Imaging. In *Nuclear Science Symposium Conference Record*, volume 6, 2006.

[96] S. Mikkelsen, D. Meier, G. MÃ|hlum, B. Sundal, J. Talebi, A. Helland, N. Ostgaard, Y. Skogseide, and K. Ullaland. Low-power and low-noise multi-channel asic for x-ray and gamma-ray spectroscopy. In *Proceedings of AMICSA*, 2008.

[97] E. Barberis, N. Cartiglia, J. Dann, T. Dubbs, K. Noble, K. O'Shaughnessy, J. Rahn, H. F. W. Sadrozinski, R. Wichmann, and T. Ohsugi. Analysis of capacitance measurements on silicon microstripdetectors. *IEEE Transactions on Nuclear Science*, 41(4 Part 1):785–790, 1994.

[98] H. Spieler. *Semiconductor detector systems*. Oxford University Press, USA, New York, 2005.

[99] S. Shokouhi, B. S. McDonald, H. L. Durko, M. A. Fritz, L. R. Furenlid, and T. E. Peterson. Thick silicon double-sided strip detectors for low-energy small-animal SPECT. *IEEE Transactions on Nuclear Science*, 56:557–564, 2009.

[100] LBL Table of the Isotopes: Decay Data Search, February 2010. `http://ie.lbl.gov/toi/nucSearch.asp`.

[101] M.J. Berger, J.H. Hubbell, S.M. Seltzer, J. Chang, J.S. Coursey, R. Sukumar, and D.S Zucker. Nist xcom: Photon cross sections database (version 3.1), 2009. available at: http://physics.nist.gov/PhysRefData/Xcom/Text/XCOM.html.

[102] R. Nath and Z.J. Chen. Silver fluorescent x-ray yield and its influence on the dose rate constant for nine low-energy brachytherapy source models. *Medical Physics*, 34:3785, 2007.

[103] L. Pacciani, O. Uberti, E. Del Monte, A. Argan, M. Feroci, P. Soffitta, A. Trois, E. Costa, I. Donnarumma, and Y. Evangelista. Threshold equalization algorithm for the xaa1. 2 asics and its application to superagile x-ray imager. *Nuclear Instruments & Methods in Physics Research Section A*, 2008.

[104] J.M. Links. Toward a useful measure of flood-field uniformity: can the beauty in the eye of the beholder be quantified? *European Journal of Nuclear Medicine and Molecular Imaging*, 19(9):757–758, 1992.

[105] F.P. DiFilippo, S.H. Abreu, and H. Majmundar. Collimator integrity. *Journal of Nuclear Cardiology*, 13(6):889–891, 2006.

[106] *National Electrical Manufacturers Association: NEMA NU 1-2007: Performance measurements of gamma cameras*, 2007.

[107] G. F. Knoll. *Radiation detection and measurement*. Wiley, New York, 3rd edition, 2003.

[108] Jussi Pahikkala. Planetmath.org solid angle, 2009. available at: http://planetmath.org/encyclopedia/Steradian.html.

[109] TE Booth, FB Brown, JS Bull, LJ Cox, RA Forster, and JT Goorley. MCNP a general Monte Carlo N-particle transport code, Version 5, 2003. Report No. LA-UR-03-1987.

[110] M.H. Freeman and C. Hull. *Optics*. Butterworth-Heinemann Medical, New York, 2003.

[111] S. Shokouhi, B.S. McDonald, H.L. Durko, M.A. Fritz, L.R. Furenlid, and T.E. Peterson. Thick Silicon Double-Sided Strip Detectors for Low-Energy Small-Animal SPECT. *IEEE Transactions on Nuclear Science*, 56:557–564, 2009.

[112] S. Shokouhi, M. A. Fritz, B. S. McDonald, M. D. W. Wilson, S. D. Metzler, and T. E. Peterson. Design of a multi-pinhole collimator in a dual-headed, stationary, small-animal SPECT. In *Nuclear Science Symposium Conference Record, 2006. IEEE*, volume 4, pages 2399–2402, 2006.

[113] S. Shokouhi, S. D. Metzler, D. W. Wilson, and T. E. Peterson. Multi-pinhole collimator design for small-object imaging with silispect: a high-resolutionSPECTt. *Physics in Medicine and Biology*, 54(2):207–225, 2009.

[114] J R Mallard and M J Myers. The performance of a gamma camera for the visualization of radioactive isotopes in vivo. *Physics in Medicine and Biology*, 8(2):165, 1963.

[115] FP DiFilippo. A sensitivity model for multi-pinhole SPECT. In *IEEE Nuclear Science Symposium Conference Record, 2006*, volume 3, 2006.

[116] SD Metzler, KL Greer, and RJ Jaszczak. Determination of mechanical and electronic shifts for pinhole SPECT using a single point source. *IEEE Transactions on Medical Imaging*, 24(3):361–370, 2005.

[117] F. van der Have, B. Vastenhouw, M. Rentmeester, and F. J. Beekman. System calibration and statistical image reconstruction for ultra-high resolution stationary pinhole SPECT. *IEEE Transactions on Medical Imaging*, 27(7):960–971, 2008.

[118] V.Y. Panin, F. Kehren, C. Michel, and M. Casey. Fully 3-d pet reconstruction with system matrix derived from point source measurements. *Medical Imaging, IEEE Transactions on*, 25(7):907 –921, july 2006.

[119] D. Lazaro, Z. El Bitar, V. Breton, D. Hill, and I. Buvat. Fully 3D Monte Carlo reconstruction in SPECT. *Physics in Medicine and Biology*, 50:3739–3754, 2005.

[120] D. Beque, J. Nuyts, G. Bormans, P. Suetens, and P. Dupont. Characterization of pinhole SPECT acquisition geometry. *IEEE Transactions on Medical Imaging*, 22(5):599–612, 2003.

[121] Y. Wang and B.M.W. Tsui. Pinhole SPECT with different data acquisition geometries: Usefulness of unified projection operators in homogeneous coordinates. *IEEE Transactions on Medical Imaging*, 26(3):298, 2007.

[122] F. Noo, R. Clackdoyle, C. Mennessier, T.A. White, and T.J. Roney. Analytic method based on identification of ellipse parameters for scanner calibration in cone-beam tomography. *Physics in Medicine and Biology*, 45(11):3489–3508, 2000.

[123] K. Vunckx, M. Defrise, D. Bequé, C. Vanhove, A. Andreyev, and J. Nuyts. Geometrical calibration and aperture configuration design in multi-pinhole SPECT. In *IEEE Internat. Symp. on Biomed. Imag*, pages 1403–1406, 2008.

[124] L. von Smekal, M. Kachelriess, E. Stepina, and W.A. Kalender. Geometric misalignment and calibration in cone-beam tomography. *Medical Physics*, 31:3242, 2004.

[125] C. Mennessier, R. Clackdoyle, and F. Noo. Geometric calibration in cone-beam tomography. *Physics in Medicine and Biology*, 54:1633–1660, 2009.

[126] F.P. DiFilippo. Geometric characterization of multi-axis multi-pinhole SPECT. *Medical Physics*, 35:181, 2008.

[127] D. Beque, J. Nuyts, P. Suetens, and G. Bormans. Optimization of geometrical calibration in pinhole SPECT. *IEEE transactions on medical imaging*, 24(2):180–190, 2005.

[128] S. Jan, G. Santin, D. Strul, S. Staelens, K. Assie, D. Autret, S. Avner, R. Barbier, M. Bardies, P. M. Bloomfield, D. Brasse, V. Breton, P. Bruyndonckx, I. Buvat, A. F. Chatziioannou, Y. Choi, Y. H. Chung, C. Comtat, D. Donnarieix, L. Ferrer, S. J. Glick, C. J. Groiselle, D. Guez, P. F. Honore, S. Kerhoas-Cavata, A. S. Kirov, V. Kohli, M. Koole, M. Krieguer, D. J. van der Laan, F. Lamare, G. Largeron, C. Lartizien, D. Lazaro, M. C. Maas, L. Maigne, F. Mayet, F. Melot, C. Merheb, E. Pennacchio, J. Perez, U. Pietrzyk, F. R. Rannou, M. Rey, D. R. Schaart, C. R. Schmidtlein, L. Simon, T. Y. Song, J. M. Vieira, D. Visvikis, R. V. de Walle, E. Wieers, and C. Morel. Gate: a simulation toolkit for PET and SPECT. *Physics in Medicine and Biology*, 49(19):4543–4561, 2004.